SPECTROSCOPIC AND KINETIC INVESTIGATION OF THE CATALYTIC MECHANISM OF TYROSINE HYDROXYLASE

A Dissertation

by

BEKIR ENGIN ESER

Submitted to the Office of Graduate Studies of
Texas A&M University
in partial fulfillment of the requirements for the degree of

DOCTOR OF PHILOSOPHY

December 2009

Major Subject: Chemistry

SPECTROSCOPIC AND KINETIC INVESTIGATION OF THE CATALYTIC MECHANISM OF TYROSINE HYDROXYLASE

A Dissertation

by

BEKIR ENGIN ESER

Submitted to the Office of Graduate Studies of
Texas A&M University
in partial fulfillment of the requirements for the degree of

DOCTOR OF PHILOSOPHY

Approved by:

Co-Chairs of Committee,	Paul F. Fitzpatrick
	Frank M. Raushel
Committee Members,	Paul A. Lindahl
	Gregory D. Reinhart
Head of Department,	David H. Russell

December 2009

Major Subject: Chemistry

ABSTRACT

Spectroscopic and Kinetic Investigation of the Catalytic Mechanism of Tyrosine Hydroxylase. (December 2009)

Bekir Engin Eser, B.S., Bilkent University, Ankara, Turkey

Co-Chairs of Advisory Committee: Dr. Paul F. Fitzpatrick
Dr. Frank M. Raushel

Tyrosine Hydroxylase (TyrH) is a pterin-dependent mononuclear non-heme iron oxygenase. TyrH catalyzes the hydroxylation reaction of tyrosine to dihydroxyphenylalanine (DOPA). This reaction is the first and the rate-limiting step in the biosynthesis of the catecholamine neurotransmitters. The active site iron in TyrH is coordinated by the common facial triad motif, 2-His-1-Glu. A combination of kinetic and spectroscopic techniques was applied in order to obtain insight into the catalytic mechanism of this physiologically important enzyme.

Analysis of the TyrH reaction by rapid freeze-quench Mössbauer spectroscopy allowed the first direct characterization of an Fe(IV) intermediate in a mononuclear non-heme enzyme catalyzing aromatic hydroxylation. Further rapid kinetic studies established the kinetic competency of this intermediate to be the long-postulated hydroxylating species, Fe(IV)O.

Spectroscopic investigations of wild-type (WT) and mutant TyrH complexes using magnetic circular dichroism (MCD) and X-ray absorption spectroscopy (XAS) showed that the active site iron is 6-coordinate in the resting form of the enzyme and that binding of either tyrosine or $6MPH_4$ alone does not change the coordination. However, when both tyrosine and $6MPH_4$ are bound, the active site becomes 5-coordinate, creating an open site for reaction with O_2. Investigation of the kinetics of oxygen reactivity of TyrH complexes in the absence and presence of tyrosine and/or $6MPH_4$ indicated that there is a significant enhancement in reactivity in the 5-coordinate complex in comparison to the 6-coordinate form. Similar investigations with E332A TyrH showed that Glu332 residue plays a role in directing the protonation of the bridged complex that forms prior to the formation of Fe(IV)O.

Rapid chemical quench analyses of DOPA formation showed a burst of product formation, suggesting a slow product release step. Steady-state viscosity experiments established a diffusional step as being significantly rate-limiting. Further studies with stopped-flow spectroscopy indicated that the rate of TyrH reaction is determined by a combination of a number of physical and chemical steps.

Investigation of the NO complexes of TyrH by means of optical absorption, electron paramagnetic resonance (EPR) and electron spin echo envelope modulation (ESEEM) techniques revealed the relative positions of the substrate and cofactor with respect to NO, an O_2 mimic, and provided further insight into how the active site is tuned for catalytic reactivity upon substrate and cofactor binding.

DEDICATION

This dissertation is dedicated to my parents and my sister.

ACKNOWLEDGEMENTS

I would like to thank my advisor, Dr. Paul F. Fitzpatrick, for his guidance and support throughout my Ph.D. work and for giving me the opportunity to work on projects that provided me with a diverse range of skills. I give thanks to all the past and present members of Fitzpatrick Lab. It was a very enjoyable experience for me to be a member of this lab. I would also like to thank my committee members; co-chair, Dr. Frank M. Raushel, Dr. Paul A. Lindahl and Dr. Gregory D. Reinhart.

I would like to thank all our collaborators for the collaborative projects that constitute parts of this dissertation; Dr. Edward I. Solomon, Dr. Marina Chow, Dr. Keith O. Hodgson, Dr. Britt Hedman and Samuel A. Wilson (Stanford University); Dr. J. Martin Bollinger, Dr. Carsten Krebs and Eric Barr (PSU); and Dr. John McCracken and Matthew Krzyaniak (MSU).

I would like to thank Dr. Vijay Gawandi for the synthesis of deuterated tatrahydropterin and I would also like to thank Dr. Paul Lindahl's lab for their assistance in EPR measurements.

Last but not least, I give thanks to all of my friends in College Station.

ABBREVIATIONS

4a-HO-$6MPH_3$	4a-hydroxypterin
5C	Five-Coordinate Complex
6C	Six-Coordinate Complex
$6MPH_2$	6-Methyldihydropterin
$6MPH_4$	6-Methyltetrahydropterin
α-KG	α-Ketoglutarate
AAH	Aromatic Amino Acid Hydroxylase
BH_4	Tetrahydrobiopterin
DOPA	Dihydroxyphenylalanine
EDTA	Ethylene Diamine Tetraacetic Acid
EPR	Electron Paramagnetic Resonance
ESEEM	Electron Spin Echo Envelope Modulation
EXAFS	Extended X-ray Absorption Fine Structure
Hepes	4-(2-Hydroxyethyl)-1-Piperazineethanesulfonic Acid
LF	Ligand Field
MCD	Magnetic Circular Dichroism
Mops	3-(N-Morpholino) Propanesulfonic Acid
q-$6MPH_2$	Quinonoid 6-Methyldihydropterin
Phe	Phenylalanine
PheH	Phenylalanine Hydroxylase
RFQ	Rapid Freeze Quench

TrpH	Tryptophan Hydroxylase
Tyr	Tyrosine
TyrH	Tyrosine Hydroxylase
TauD	Taurine Dioxygenase
VTVH	Variable Temperature Variable Field
XAS	X-ray Absorption Spectroscopy

TABLE OF CONTENTS

Page

LIST OF FIGURES

FIGURE Page

FIGURE Page

FIGURE Page

LIST OF TABLES

CHAPTER I

INTRODUCTION

The utilization of molecular oxygen by biological systems is crucial for aerobic life. Molecular oxygen is the terminal electron acceptor in the synthesis of energy rich molecules, which are used by aerobic organisms for their metabolic energy needs. The other important function of molecular oxygen is its role in the biosynthesis of significant biomolecules through reactions with organic substrates (*1*). Although these reactions are thermodynamically favorable, they face high kinetic barriers due to the spin mismatch between molecular oxygen and organic substrates. Molecular oxygen has a triplet spin due to the presence of two unpaired electrons in its ground state molecular orbital configuration; however, the organic substrates that are targets for O_2 reactivity are in the singlet spin state (*2*).

In order to eliminate the kinetic barrier due to this spin mismatch, aerobic organisms utilize transition metals for most of their metabolic oxidation and oxygenation reactions. Due to their strong ability to change valance, transition metals can activate O_2 by acting as electron donors. Thus, a remarkable number of metalloenzymes, with mononuclear or multinuclear iron and copper active sites, are functional in a wide variety of oxidative transformations that require activation of molecular oxygen for reaction with

---

This dissertation follows the style of *Biochemistry*.

organic substrates (*1-7*). In addition to their role in oxygen activation, these enzymes also tightly control the reactivity of their activated oxygen species so that they only react with specific substrates at specific positions without side reactions that can harm the organism (*1*).

The metalloenzymes that use iron for oxidative transformations of biomolecules can be classified into two main groups; heme enzymes, which contain a porphyrin ring coordinated to the active site iron, and non-heme enzymes, which include dinuclear and mononuclear members with varying number of protein derived ligands (*2, 5*). The mechanisms of heme enzymes are well established from extensive studies on heme peroxidases and cytochrome P450s (*8, 9*). Studies on dinuclear non-heme enzymes, especially on ribonucleotide reductase R2 protein and soluble methane monooxygenase in 1990s, have led to a significant understanding of the mechanism of these enzymes and of the iron based intermediates involved in the activation processes (*2, 7, 10*).

Although studies on mononuclear non-heme enzymes lagged behind those of their heme and dinuclear non-heme counterparts, crystallographic and spectroscopic investigations in the last decade contributed significantly to our understanding of how these enzymes work (*1, 2, 4-6*). These studies also revealed that the mononuclear non-heme family is even more versatile then the heme and dinuclear non-heme families. The reactions catalyzed by various members of this family include hydroxylation of aliphatic and aromatic substrates, epoxidation, aromatic ring cleavage, desaturation, cyclization, halogenation, and dihydroxylation. In most of the mononuclear non-heme enzymes, the iron is coordinated by a 2-His-1-Glu/Asp motif, termed a facial triad (*11, 12*), although variations from this motif have been observed (*13*). Heme containing enzymes have a porphyrin ring that occupies four coordination sites and a protein derived axial ligand to fill the fifth ligation site, leaving only one open coordination to be the oxygen binding site. In contrast, in mononuclear non-heme enzymes, three coordination sites (other than those occupied by the facial triad) are available for binding O_2 or other possible exogenous ligands such as substrates and/or cofactors, giving these enzymes great flexibility for catalysis (*11*). Thus, although most of the mononuclear non-heme family members are similar in their core catalytic active site structure, the way that different subfamilies of these enzymes handle their substrates can be very different, resulting in a versatile set of catalyzed reactions (*2, 5*).

Mononuclear non-heme enzymes can be divided into two categories; oxygen-activating and substrate-activating. Enzymes that activate oxygen with their ferrous iron sites constitute a very large and diverse group, whereas the substrate-activating category consists of a small group of enzymes, including lipoxygenases and intradiol dioxygenases, which activate their substrates with ferric iron sites for reaction with oxygen (*2*). The oxygen-activating group of enzymes catalyzes a very broad array of transformations and can be classified into four main groups, as shown in Figure 1 (*5, 11*). In addition to those four main classes, there is also a “catch-all” category, which mostly includes enzymes with oxidase functionality (*1*). Although all of these classes have a similar active site structure; a mononuclear non-heme ferrous iron coordinated by the 2-His-1-Asp/Glu facial triad, they exhibit significant diversity in the reactions they catalyze and in the strategies they use to catalyze these reactions. Some of these classes use a cofactor to supply electrons for the reductive activation of O_2, whereas others obtain reducing equivalents from their substrates. The use of cofactors and substrates by these enzymes and the structures of the iron intermediates that carry out the reactions also exhibit differences among classes. In some cases, cofactors and/or substrates bind directly to the iron for catalysis, but for some groups they do not. Some of the common iron species that appear as reactive intermediates in the reaction cycles of mononuclear non-heme enzymes are shown in Scheme 1.

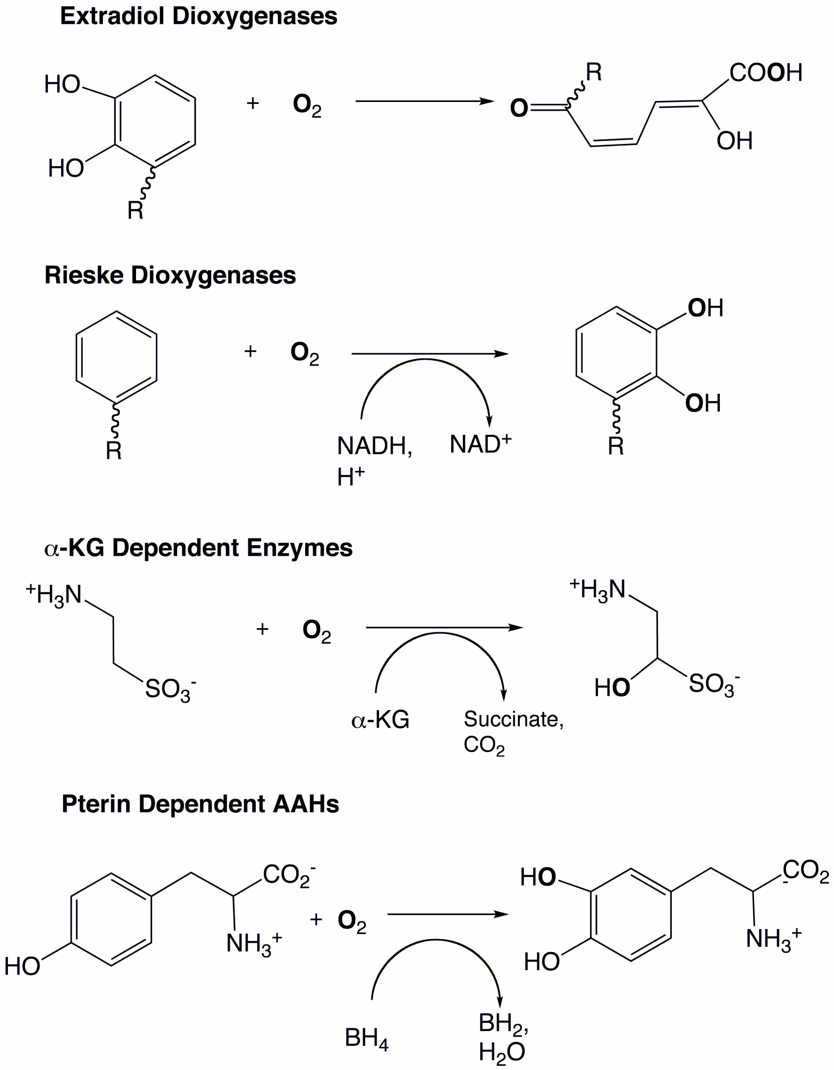

FIGURE 1. Classes of oxygen-activating mononuclear non-heme enzymes and their representative reactions.

Scheme 1

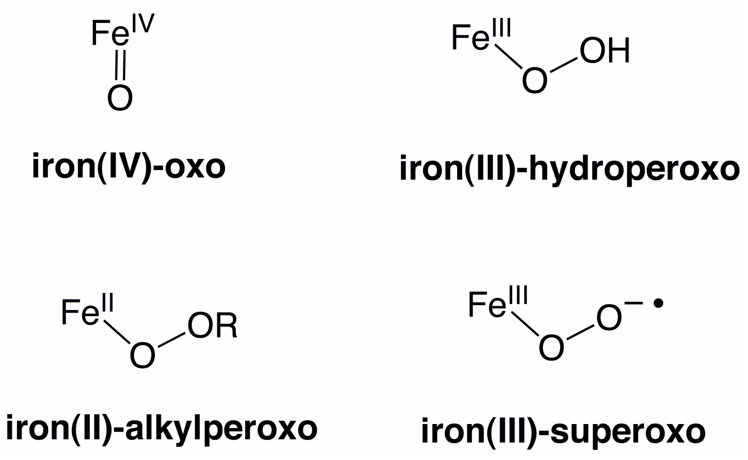

Extradiol dioxygenases and Rieske dioxygenases incorporate both atoms of molecular oxygen into their aromatic substrates (*1, 5*). The substrates of extradiol dioxygenases are catechols, which can make bidentate coordination to the iron. This family of enzymes carries out a 4-electron oxidation process in which all the electrons are supplied by the substrate; thus, they do not need an external electron source. Iron(III)-superoxo and iron(II)-alkylperoxo species have been identified as reactive intermediates in the extradiol dioxygenases (Scheme 1). In the case of Rieske dioxygenases, in contrast, the substrate provides two-electrons and the two additional electrons required for the reduction of oxygen are supplied by NADH. The substrate binds close to the iron, and either a iron(III)-(hydro)peroxide or a HO-Fe(IV)O intermediate carries out the cis-dihydroxylation of the aromatic substrate. The most versatile class in the mononuclear non-heme family is the α-ketoglutarate (α-KG) dependent enzymes (*5, 14*). The enzymes in this class use α-KG as a cofactor; this goes through oxidative decarboxylation during turnover, providing the additional two electrons required for reductive activation of O_2.

The α-KG cofactor coordinates to the iron in a bidentate fashion, next to the oxygen-binding site, similar to the substrate binding in extradiol dioxygenases. Substrates of α-KG dependent enzymes bind close to the active site, but do not ligate to the iron. Attack of an iron(III)-superoxo intermediate onto α-KG incorporates one of the atoms of O_2 into the cofactor and forms a high valent Fe(IV)O intermediate that is capable of carrying out various oxidative transformations such as aliphatic hydroxylation, ring formation, and desaturation.

The other oxygen activating mononuclear non-heme family is a small but physiologically important group of pterin-dependent enzymes, the aromatic amino acid hydroxylases (AAH) (*1, 5, 15, 16*). The members of this family use tetrahydropterin as a cofactor to activate dioxygen for hydroxylation of their amino acid substrates (Scheme 2). Contrary to the other classes of mononuclear non-heme enzymes, both the aromatic amino acid substrate and the tetrahydropterin cofactor incorporate one atom of O_2, but neither of them is directly bound to the iron during catalysis. Tyrosine hydroxylase (TyrH) catalyzes conversion of tyrosine to dihydroxyphenylalanine (DOPA), the first and the rate limiting step in the biosynthesis of catecholamine neurotransmitters (dopamine, adrenaline and noradrenaline). TyrH is found in the brain and adrenal gland. A deficiency of this enzyme leads to various neurological disorders such as DOPA-responsive Parkinson's disease, progressive encephalopathy, DOPA-non-responsive dystonia and DOPA-responsive dystonia (Segawa's disease) (*17, 18*). Phenylalanine hydroxylase (PheH), another member of the family, is a liver enzyme and catalyzes hydroxylation of phenylalanine in the diet to tyrosine. Mutations in this enzyme cause a genetically inherited disorder, phenylketonuria (PKU), which can lead to irreversible mental retardation without early treatment (*15*). Tyrptophan hydroxylase (TrpH) catalyzes the conversion of tyrptophan to 5-hydroxytryptophan, the rate-limiting step in the biosynthesis of the neurotransmitter serotonin. A deficiency in serotonin, which is involved in various brain functions such as sleep and mood regulation, leads to disorders such as depression, schizophrenia and obsessive-compulsive disorder (*15, 19, 20*). TrpH is found in the brain and in the pineal gland (*15, 20*).

Scheme 2

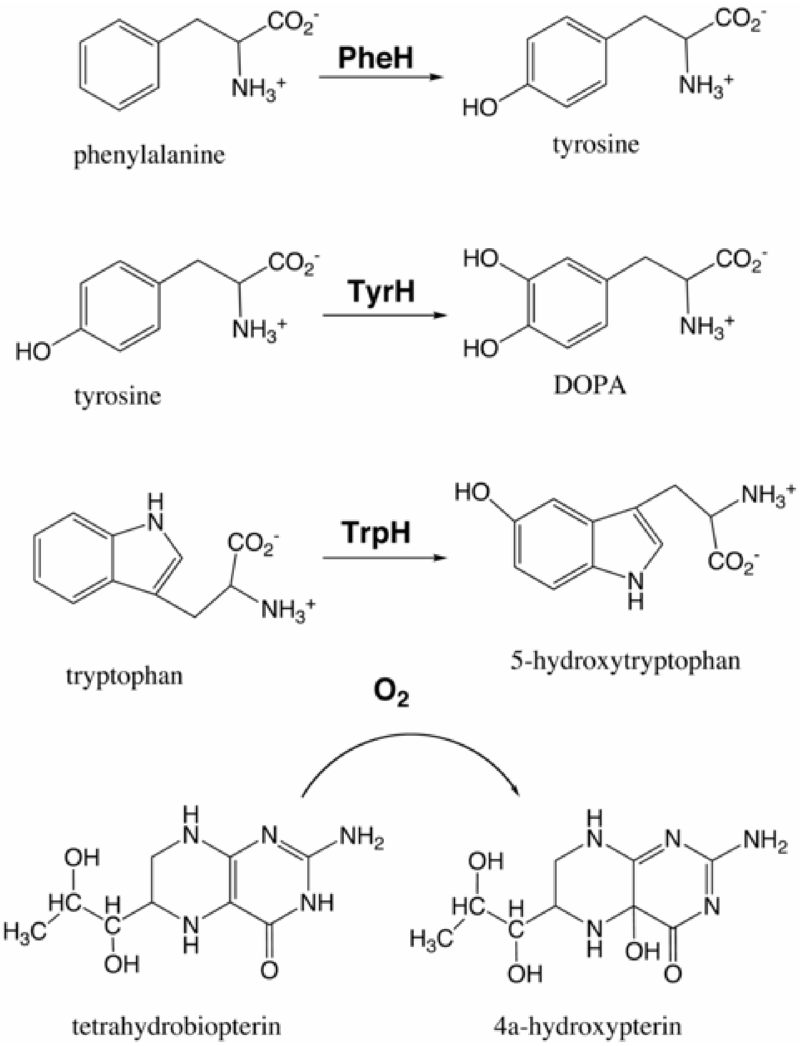

All eukaryotic enzymes of the family are homotetramers (*15, 21*). There is also a bacterial form of PheH that is a monomer. The structures of all three enzymes are made up of three domains: A regulatory domain of 100 to 160 amino acids at the N-terminus, a catalytic domain of about 280 residues close to the C-terminus and a small (40-50 residues) tetramerization domain at the C-terminus. The regulatory domains of the family members exhibit <14% sequence identity, consistent with their different mechanisms of regulation. TyrH is regulated by the phosphorylation of a number of serine residues in the regulatory domain, which decreases the inhibition by catecholamines giving the active ferrous form of the enzyme. PheH and TrpH are also regulated to some extent by phosphorylation of serine residues in their regulatory domains (*15, 21*) . In contrast to the regulatory domains, the catalytic domains of all three enzymes are very similar and show 52% identity for the rat enzymes. This is in agreement with their similar catalytic properties.

The only crystal structure having both the regulatory domain and the catalytic domain has been determined for PheH (*22*). Three-dimensional structures for the catalytic domain have been obtained for all three enzymes (*23-26*), and the structure of the tetramerization domain is also available for TyrH (*23, 27*). This structure shows the coiled-coil that is responsible for tetramer formation (*23, 27*). All three enzymes have one iron per monomer located in an active site cleft that is ~10 Å deep (Figure 2). The common mononuclear non-heme motif, a facial triad of 2-His and 1-Glu (His-$(X)_4$-His-$(X)_{39}$-Glu) coordinates the active site iron in the AAHs (*12, 21*). For TyrH, the facial triad is made up of His 331, His 336 and Glu 376. Structures of the catalytic domains with a tetrahydropterin or a pterin analogue have been determined for all the members of

AAH family (*26-28*). These structures show that the backbone of a flexible loop consisting of the residues 247-251 in PheH interact with the N(1)-N(8) side of the pterin ring. The only electrostatic interaction between the protein and pterin is from the carboxylate of Glu286 for PheH (Glu332 for TyrH). Mutation of this residue in TyrH has been shown to lead significant uncoupling and a 10-fold increase in K_m for pterin (*29*).

The structures that are most relevant to catalysis have been determined only for PheH (*25, 30*). In this case, structures have been obtained with both tetrahydrobiopterin and a substrate analogue, thienylalanine or norleucine bound. These structures show significant differences compared to the resting and binary forms. The monodentate Glu ligand now becomes bidentate and pterin moves ~1.5 Å towards the iron such that the distance of the C-4a of the pterin from the iron decreases from 6 Å to 4.5 Å, a distance close enough for a reaction involving oxygen, pterin and iron. Contrary to the structures of the binary complexes, the active site is now 5-coordinate, with only one water molecule bound. MCD and XAS spectroscopies also supported the observations that the iron active site becoming five coordinate and the glutamate becoming bidentate (*31, 32*). In addition to the active site changes, a movement of a mobile loop consisting of the residues 131-150 occurs in the ternary complex. The side chain of Tyr138, the residue in the middle of the loop, moves almost 20 Å from a surface position towards the active site and pack against the residues that make the amino acid binding site. Mutation of this residue results in a significant decrease in activity (*33*). Although the movement of this loop is only observed in the ternary structure, fluorescence anisotropy studies suggested pterin binding as being the initiator of this conformational change in TyrH (*34*). Overall, the combination of structural and spectroscopic data on the ternary complex of PheH indicate that binding of the substrate and the cofactor makes the active site ready for reaction with oxygen and for the catalysis to proceed.

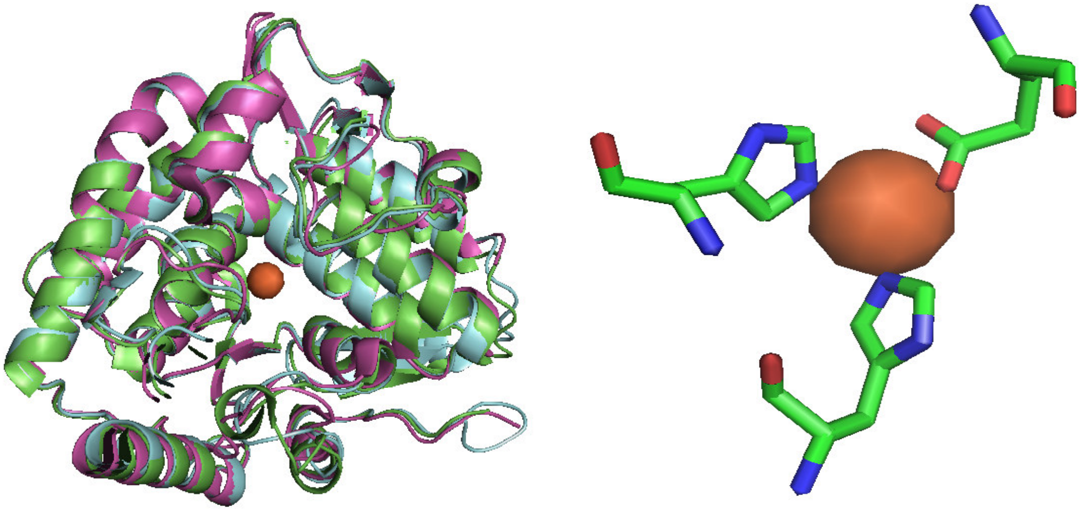

FIGURE 2. (Left) Overlay of the catalytic domains of human PheH (1J8U), rat TyrH (2TOH) and human TrpH (1MLW). The active site iron is in orange. (Right) The active site iron of TyrH (1TOH) coordinated by the 2-His-1Glu facial triad.

The ternary complex structure also reveals the residues making up the amino acid binding site. A hydrophobic cage made up of the side chains of aromatic amino acid residues surrounds the aromatic ring of the substrate side chain (*21, 25*). Site-directed mutagenesis studies showed that amino acids that pack against the residues forming the aromatic cage determine the substrate specificity of the enzymes (*35*).

Steady-state studies established the binding order for TyrH, with tetrahydropterin being the first substrate to bind, followed by oxygen in rapid equilibrium and then tyrosine as the last (*36*). Although studies on PheH and TrpH have not established a consensus binding order, studies with all three enzymes show that all three substrates must be bound before any catalytic reaction takes place (*21*).

One important aspect of the reaction of TyrH and other members of AAHs is that for each product molecule formed, a pterin molecule is oxidized. This gives 100% coupling between DOPA formation and pterin oxidation. Mutations of the residues close to the active site or use of unnatural substrates leads to uncoupling, more pterin being oxidized than the amino acid being hydroxylated (*21, 29, 37*).

All members of the AAH family share a similar mechanism (*38-41*). The proposed mechanism for TyrH is shown in Scheme 3 (*21*). Both the amino acid substrate and tetrahydropterin cofactor are required to bind to the active site before any catalytic reaction takes place. The reaction can be considered as the combination of two major steps. The first step, similar to the other oxygen activating non-heme enzymes (*11*), is formation of the hydroxylating intermediate. This part of the catalysis involves a reaction between iron, tetrahydropterin and molecular oxygen to give an iron μ-peroxypterin. Heterolytic cleavage of this intermediate leads to the formation of the hydroxylating intermediate, a high valence Fe(IV)O species, and the product 4a-hydroxypterin, which is released from the active site and dehydrates in solution to give quinonoid dihydropterin (*42*). NADH-dependent dihydropteridine reductase recycles quinonoid dihydropterin back to tetrahydropterin (*43*).

Scheme 3

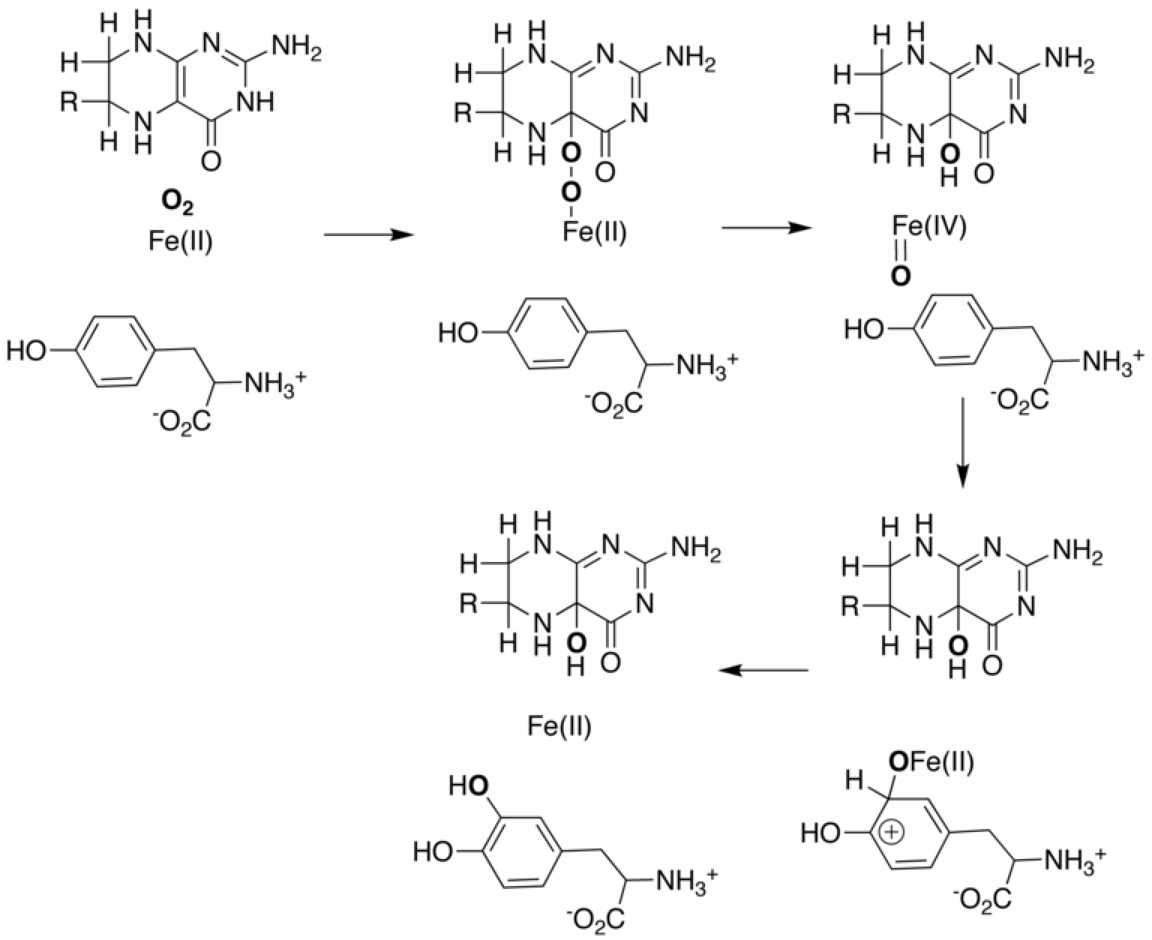

The second part of the mechanism is the reaction of the Fe(IV)O species with the amino acid to give the hydroxylated product. In order to probe the mechanism of this hydroxylation step, the amount of the hydroxylated product was determined using various 4-substituted phenylalanines as substrates for TyrH. The results yielded a good correlation with the σ values of the substituents, with a ρ value of ~ -5, which indicates a cationic transition state for the hydroxylation step, consistent with electrophilic aromatic substitution mechanism (*44*). The inverse isotope effects obtained for of all three enzymes further support this mechanism (*38, 40*).

A combination of many experimental and computational observations supports Fe(IV)O as being the hydroxylating species for the AAH family (*21*). Fe(IV)O species have been characterized as hydroxylating intermediates in some heme containing enzymes (e.g., heme peroxidases and cytochrome P450s) and in a number of dinuclear and mononuclear non-heme enzymes (e.g., soluble methane monooxygenase, α-KG enzymes) (*8-10, 45*). Isotope effect studies showed that all three members of the AAH family can catalyze benzylic hydroxylation with a reactivity similar to heme based cytochrome P450s, which also use Fe(IV)O for hydroxylation of aliphatic substrates (*39, 46*). Computational studies on AAHs are also consistent with the formation of Fe(IV)O through heterolytic cleavage of iron μ-peroxypterin intermediate and the ability of this intermediate to carry out aromatic and benzylic hydroxylation (*47, 48*).

Steady-state kinetic studies with TyrH indicated that k_{cat} of the reaction is not dependent on the identity of the amino acid (*36, 49*). This suggested that the slow step in the mechanism is oxygen activation. ^{18}O isotope effects on *V/K* are in agreement with the effect being due to combination of equilibrium binding of oxygen to the iron and then an inner sphere electron transfer mechanism during formation of iron μ-peroxypterin intermediate (*50*).

This dissertation will report experimental results from a combination of spectroscopic and kinetic studies on the catalytic mechanism of TyrH. Kinetic dissection of individual steps, characterization of reaction intermediates and the correlation of the active site structural changes to reactivity in TyrH reaction will be described.

CHAPTER II

KINETIC AND CHEMICAL CHARACTERIZATION OF THE FERRYL-OXO INTERMEDIATE IN TYROSINE HYDROXYLASE REACTION BY RAPID REACTION TECHNIQUES*

INTRODUCTION

The aromatic amino acid hydroxylases (AAH) form a small family of mononuclear non-heme enzymes. The members of this family use tetrahydropterin as a cofactor for the hydroxylation of their amino acid substrates (*15, 16*). Tyrosine hydroxylase (TyrH) catalyzes the conversion of tyrosine to dihydroxyphenylalanine (DOPA) as the first and the rate-limiting step in the biosynthesis of catecholamine neurotransmitters (dopamine, adrenaline and noradrenaline) (Scheme 4). TyrH is found in the brain and adrenal gland. Deficiency of this enzyme leads to various neurological disorders such as DOPA-responsive Parkinson's disease, progressive encephalopathy, DOPA-non-responsive dystonia and DOPA-responsive dystonia (Segawa's disease) (*17, 18*).

---

*Reproduced in part with permission from Eser, B. E., Barr, E. W., Frantom, P. A., Saleh, L., Bollinger, J. M., Jr., Krebs, C., and Fitzpatrick, P. F. *J.Am.Chem.Soc.* **2007**, *129*, 11334–11335. Copyright 2007 American Chemical Society.

The other members of the family are phenylalanine hydroxylase (PheH) and tyrptophan hydroxylase (TrpH). PheH is a liver enzyme and catalyzes hydroxylation of phenylalanine in the diet to tyrosine. A deficiency of PheH is responsible for phenylketonuria, one of the most common genetically inherited diseases of amino acid metabolism (*15*). TrpH, the rate-limiting enzyme in the biosynthesis of serotonin, converts tyrptophan to 5-hydroxytryptophan and is found in the central nervous system and in the pineal gland (*15, 20*).

Scheme 4

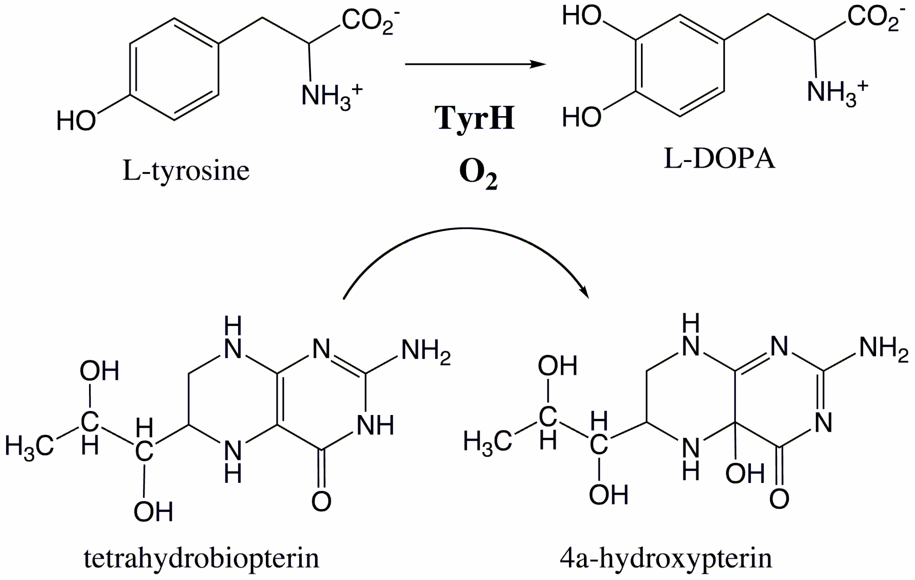

All three enzymes of the AAH family, consistent with their analogous catalytic domain, share a similar mechanism (*38-41*). They have similar active sites where the mononuclear non-heme iron is coordinated by a 2-His-1-Glu facial triad (*23, 51*), a common catalytic motif responsible for the various reactivities of non-heme systems (*12*). The proposed mechanism for TyrH is shown in Scheme 3 (*21*). The mechanism can be divided into two partial reactions. The first part involves formation of an iron μ-peroxypterin bridge after a reaction between iron, oxygen and tetrahydropterin. In order for this reaction to occur, the amino acid substrate must be bound (*21*). The heterolytic cleavage of the O-O bond gives the hydroxylating intermediate, the proposed Fe(IV)O, and the side product 4a-hydroxypterin. In the second part of catalysis, the reaction of the hydroxylating intermediate with the aromatic ring gives the product, DOPA, through electrophilic aromatic substitution (*44*). Although the proposed mechanism for AAHs has been supported by many experimental and computational observations, no intermediate has been characterized directly to date. A Fe(IV)O has for long been postulated to be the hydroxylating species for amino acid hydroxylases (*21*). Fe(IV)O species have been characterized as hydroxylating intermediates in some heme protein systems (e.g., heme peroxidases) (*8, 9*) as well as in a number of non-heme systems (e.g., ribonucleotide reductase protein R2 and soluble methane monooxygenase) (*7, 10*), and the ability of this species to oxygenate unactivated molecules has also been shown with inorganic non-heme model complexes (*52*). Previous studies demonstrated that all three members of AAH family are capable of carrying out benzylic hydroxylation, in addition to their unique aromatic hydroxylation reactions (*16*). PheH can also catalyze difficult aliphatic hydroxylation and epoxidation reactions (*16*). Investigation of the mechanism of benzylic hydroxylation by all three enzymes demonstrated their similar reactivity to heme based cytochrome P450s, which use Fe(IV)O for hydroxylation of aliphatic substrates (*39, 46*). In addition, some of the mononuclear non-heme families are also capable of aliphatic hydroxylation reactions and Fe(IV)O species have been proposed to be the hydroxylating intermediates in these enzymes (e.g., α-KG dependent enzymes and IPNS) (*2, 21*).

Further evidence comes from computational studies carried out for the AAH family by Bassan and coworkers. Reaction models investigated using hybrid density functional theory are in agreement with the formation of Fe(IV)O through heterolytic cleavage of iron μ-peroxypterin intermediate and the ability of this intermediate to carry out aromatic and benzylic hydroxylation (*47, 48*).

Mössbauer spectroscopy is a powerful technique for the characterization of the electronic and magnetic properties of iron species (*10, 53*). ^{57}Fe exhibits transitions between the nuclear ground state, I=1/2, and the first excited-state, I=3/2, that can be perturbed by the electronic structure of the chemical environment around the iron via hyperfine interactions, thus revealing information about the oxidation state of iron as well as the spin state (Figure 3). RFQ method coupled with Mössbauer spectroscopy enables us to trap intermediates by freezing reaction samples in a cryosolvent after allowing the reaction to proceed for a defined period of time (*53*). These frozen samples then can be analyzed by Mössbauer spectroscopy, allowing characterization of the iron species present in the sample. In addition, the absorption intensity of the Mössbauer signal can be correlated to the quantity of the iron species; thus, the kinetics of an intermediate can be studied by collecting samples at various time points. RFQ EPR is a complementary technique to RFQ Mössbauer spectroscopy and often used in conjunction with cryoreduction in order to obtain EPR active Fe(III) species from EPR inactive Fe(IV) intermediates (*53*). Combination of these two techniques provides detailed information about the kinetics and chemical nature of iron intermediates.

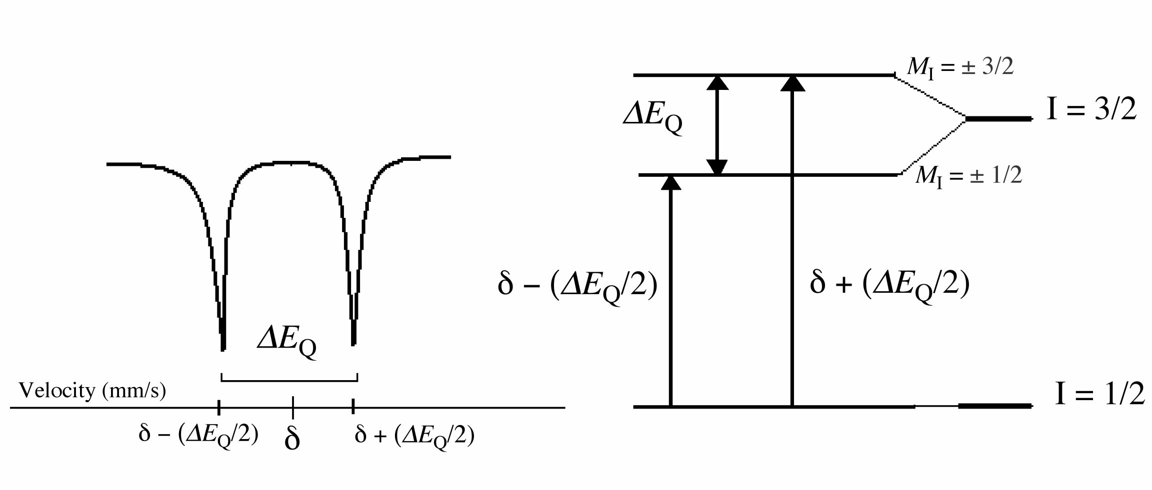

FIGURE 3. The theoretical basis for Mössbauer spectroscopy. Left is a typical quadrupole doublet Mössbauer spectrum in the absence of magnetic field. δ is the isomer shift and ΔE_Q is the quadrupole splitting parameter. Right are the nuclear energy levels of ^{57}Fe and the transitions that give rise to the Mössbauer quadrupole doublet spectrum.

RFQ ^{57}Fe Mössbauer technique has been successfully utilized for direct detection of the high-valent ferryl-oxo species proposed for a number of heme-containing and dinuclear non-heme systems and has brought significant insight into the catalytic mechanisms of these enzymes (*53-56*). Recently, a high-spin Fe(IV) intermediate was directly characterized for the first time for a mononuclear non-heme enzyme, taurine/alpha-ketoglutarate dioxygenase (TauD) (*57*). Further investigation of this intermediate using continous flow resonance Raman and X-ray absorption spectroscopies confirmed the presence of a Fe(IV)=O bond (*58, 59*). Stopped-flow absorption spectroscopy and deuterium kinetic isotope effect studies brought further evidence for the catalytic competency of this intermediate as the hydroxylating species in the TauD reaction (*60*). The studies on TauD were followed by the characterization of Fe(IV)O intermediates in some other mononuclear non-heme enzymes, including prolyl-4-hydroxylase and halogenase cytc3, both of which are also α-KG-dependent (*45*).

For the AAH family, as stated above, computational studies and the ability of the family members to catalyze difficult benzylic and aliphatic hydroxylation reactions similar to heme and non-heme enzyme systems strongly support the presence of a high-valent Fe(IV)O species as the hydroxylating intermediate (*21*). In order to address the involvement of such an intermediate directly, the reaction of TyrH with oxygen was studied by RFQ Mössbauer and RFQ EPR spectroscopies in collaboration with the laboratories of J. Martin Bollinger, Jr., and Carsten Krebs at Pennsylvania State University. Further studies were carried out using rapid chemical quench and stopped-flow spectroscopy in order to demonstrate the kinetic competency of this intermediate in TyrH reaction.

EXPERIMENTAL PROCEDURES

Materials. 6-Methyltetrahydropterin (6MPH$_4$) was from Schircks Laboratories (Jona, Switzerland). Ferrous ammonium sulfate, hepes, potassium chloride and ammonium sulfate were purchased from Fisher (Pittsburgh, PA). Glycerol and tyrosine were from Sigma-Aldrich (Milwaukee, WI). Ampicillin was from USB Corporation (Cleveland, OH). Isopropyl β-thiogalactopyranoside (IPTG) was purchased from Inalco (Milano, Italy). All other reagents were of the highest purity commercially available.

Enzyme Expression and Purification. Wild-type TyrH was expressed in *E. coli* and purified as previously described (*61*). In order to make the enzyme apo, the ammonium sulfate pellet at the end of purification was resuspended in 5 mM EDTA, 200 mM Hepes (pH 7.5), 10% glycerol and 0.1 M KCl, and incubated on ice for one hour. The enzyme solution was then dialyzed against the same buffer without EDTA. The iron content of the apo-enzyme was measured using a Perkin-Elmer AAnalyst600 atomic absorption instrument. The typical iron content of an apoenzyme preparation was 0.1-0.15 equivalents.

Preparation of Mössbauer and EPR Samples. The concentration of TyrH was determined using an extinction coefficient of 58.24 $mM^{-1}cm^{-1}$ at 280 nm (*62*). Highly concentrated stock solution of tyrosine (~50 mM) was prepared in a solution with a final pH of ~10. The exact concentration of the tyrosine stock solution was determined using an extinction coefficient of 1.34 $mM^{-1}cm^{-1}$ at 275 nm in 0.1 M HCl. Stock solution of 6-methyltetrahydropterin was prepared in 2 mM HCl and an extinction coefficient of 17.8 $mM^{-1}cm^{-1}$ in 2 M perchloric acid was used to determine the concentration. Anaerobic solutions of the TyrH:^{57}Fe(II) :tyr:6MPH$_4$ complex (2.15 mM TyrH, 1.95 mM Fe(II), 3.7 mM 6MPH$_4$ and 3.7 mM Tyr in 200 mM Hepes, 10% glycerol, 0.1 M KCl at pH 7.5) were prepared in a MBraun anoxic chamber with a nitrogen atmosphere (Peabody, MA). ^{57}Fe(II) was prepared by dissolving ^{57}Fe(0) in oxygen-free H_2SO_4 (2 N). In order to avoid denaturation of the protein solution, the acidic ^{57}Fe(II) stock (50 mM) was mixed with an anaerobic solution of 1 M Tris•HCl, pH 7.6, prior to its addition. The 0 ms time sample was prepared by taking an aliquot of the TyrH:^{57}Fe(II):Tyr:6MPH$_4$ complex and transferring it directly to a Mössbauer cell. The cell was sealed in a vial and frozen in liquid nitrogen after being removed from the glove box. The procedure for the preparation of freeze-quenched Mössbauer and EPR samples using the rapid-quench instrument has previously been described (*63*). The TyrH:^{57}Fe(II) :Tyr:6MPH$_4$ complex was loaded into a rapid quench syringe in the glovebox. The syringe was then removed from the glovebox and attached to the instrument. A second syringe of O_2-saturated (1.9 mM) buffer (200 mM Hepes, pH 7.5, 10% glycerol, 0.1 M KCl) was also connected to the instrument. These solutions were mixed at 5 °C in a volume ratio of 1:2 (TyrH:^{57}Fe(II):Tyr:6MPH_4 vs. O_2-saturated buffer). The resulting reaction mixture was allowed to flow through an aging line with the appropriate length to give the desired reaction time before it was quenched by direct injection into 2-methylbutane at -150 °C. The total reaction time was determined by adding a quench time of about 10 ms to the calculated reaction time for the delay through the aging line (*64*).

Mössbauer Spectroscopy. Mössbauer spectra were recorded on spectrometers (WEB Research; Edina, MN) operating in the constant acceleration mode in a transmission geometry (*57*). The temperature of the samples was kept at 4.2 K during spectrum collection. A magnetic field of 40 mT was applied parallel to the γ-beam for collection of low-field spectra of the samples inside a SVT-400 dewar from Janis (Wilmington, MA). For high-field spectra, the samples were inside a 12SVT dewar (Janis) with a superconducting magnet that allows application of variable magnetic fields between 0 and 8 T parallel to the γ-beam. Data analysis was carried out using the program WMOSS from WEB Research (Edina, MN). The 8 T Mössbauer spectrum was analyzed with the spin Hamiltonian given in equation 1. The first term of the equation describes the electron Zeeman effect, the second and third terms describe the axial and rhombic zero field splitting of the electronic ground state, the fourth term represents the interaction between the electric field gradient and the nuclear quadrupole moment of the Fe sites, the fifth term describes the magnetic hyperfine interaction of the electronic spin with the ^{57}Fe nucleus, and the last term represents the nuclear Zeeman interaction. Simulations were carried out with respect to the spin of the ground state, S = 2. All tensors were assumed to be collinear.

$$\begin{aligned}\mathbf{H} = \beta\mathbf{S}\bullet\mathbf{g}\bullet\mathbf{B} + D\left(\mathbf{S}_{\mathbf{z}}^{2} - \frac{S(S+1)}{3}\right) + E\left(\mathbf{S}_{\mathbf{x}}^{2} - \mathbf{S}_{\mathbf{y}}^{2}\right) \\ + \frac{\mathbf{eQV_{zz}}}{4}\left[\mathbf{I}_{\mathbf{z}}^{2} - \frac{I(I+1)}{3} + \frac{\eta}{3}\left(\mathbf{I}_{\mathbf{x}}^{2} - \mathbf{I}_{\mathbf{y}}^{2}\right)\right] + \mathbf{S}\bullet\mathbf{A}\bullet\mathbf{I} - g_{n}\beta_{\mathbf{n}}\mathbf{B}\bullet\mathbf{I}\end{aligned} \qquad (1)$$

Cryoreduction by Low-Temperature γ-Radiolysis. The freeze-quenched 20-ms sample was irradiated by γ-irradiation using a ^{60}Co-source (total radiation dose: 3.5 MRad). The temperature of the samples was maintained at 77 K during the γ-irradiation process.

EPR Spectroscopy. EPR spectra were recorded on an ESP300 spectrometer (Bruker; Billerica, MA) equipped with an ER 041 MR Microwave Bridge and a 4102ST X-band Resonator. Spectrometer conditions were as following; temperature, 13 K; microwave frequency, 9.45 GHz; microwave power, 20 mW; modulation amplitude, 10 G; modulation frequency, 100 kHz.

Rapid Chemical Quench. Rapid chemical quench experiments of TyrH were performed using an SFM-400/Q rapid-mixing instrument from Bio-Logic (Claix, France) in quenched-flow mode. The instrument was made anaerobic through incubation with excess sodium dithionite solution for at least two hours. A solution of 500 μM apo-TyrH and 1 mM tyrosine in 200 mM Hepes (pH 7.5), 10% glycerol and 0.1 M KCl was made anaerobic in a tonometer on ice, through at least 20 argon-vacuum cycles. Ferrous ammonium sulfate (480 µM) was then added to the tonometer under argon. $6MPH_4$ stock solution was prepared in 2 mM HCl and a volume corresponding to a final concentration of 2 mM (in tonometer) was placed in the side arm of the tonometer under argon. Additional argon-vacuum cycles were performed prior to mixing the $6MPH_4$ solution with the tonometer contents, which was then loaded to one of the syringes of the rapid-mixing instrument. A buffer solution of 200 mM Hepes (pH 7.5), 10% glycerol and 0.1 M KCl was bubbled with pure oxygen gas for at least 20 min on ice (to obtain a concentration of 1.9 mM O_2) and was loaded to a second syringe of the instrument. The quenching solution, 5 M HCl, was loaded into a third syringe. The tonometer contents were mixed with the oxygenated buffer at 5 °C and quenched with acid after being aged through a 190 µl (N° 5) delay line. Collected samples were analyzed for their DOPA content using a colorimetric assay as described previously (*36*).

Stopped-Flow Spectrophotometry. Single turnover kinetics of TyrH were monitored using an Applied Photophysics (Leatherhead, UK) SX20 stopped-flow spectrophotometer in absorbance mode. The instrument was made anaerobic through incubation with excess sodium dithionite solution for at least two hours. The solutions were prepared in the same way as described above for the rapid chemical quench experiments. TyrH:Fe(II):Tyr:6-$MePH_4$ in 200 mM Hepes, 10% glycerol and 0.1 M KCl, pH 7.5 was mixed with an equal volume of the same buffer containing oxygen (950 µM final) at 5 °C. The concentrations after mixing were 35 µM TyrH:Fe(II), 80 µM Tyr and 80 µM 6-$MePH_4$ for the 248 nm trace, and 100 µM TyrH:Fe(II), 235 µM Tyr and 235 µM 6-$MePH_4$ for the 318 nm trace.

Data analysis. Time-dependent product formation traces obtained from rapid chemical quench experiments and single wavelength absorbance traces from stopped-flow spectroscopy consisted of one or more exponential kinetic phases. These data were analyzed by first fitting to single or multiple exponentials using the program KaleidaGraph (Synergy Software). Results from these fits were than taken as initial estimates for global fits and simulations. Initial estimates for unknown extinction coefficients were determined by global fitting of multiple traces using the program DynaFit (*65*). Initial concentrations were allowed to float within 10% of the experimental values. Global fitting process was performed in an iterative fashion, in which one or two parameters were varied at a time and the rest of the parameters were kept constant. Best fit parameters obtained this way were than employed for the kinetic simulation (DynaFit) of the experimental data to appropriate mechanisms.

RESULTS

RFQ Mössbauer Spectroscopy. The anaerobic TyrH:Fe(II):Tyr:6-MPH$_4$ complex (2.15 mM TyrH, 1.95 mM Fe(II), 3.7 mM, 6-MPH$_4$ and 3.7 mM tyrosine) was mixed with oxygenated buffer (1.9 mM) in a volume ratio of 1:2 at 5 °C. The reaction mixture was allowed to age from 20 ms to 390 ms before being quenched with cryosolvent (*53*). The collected samples were analyzed by Mössbauer spectroscopy (Figure 4). The control sample has two asymmetric broad lines having parameters associated with a typical high spin Fe(II) complex. The asymmetry suggests the presence of at least two distinct Fe(II) complexes.

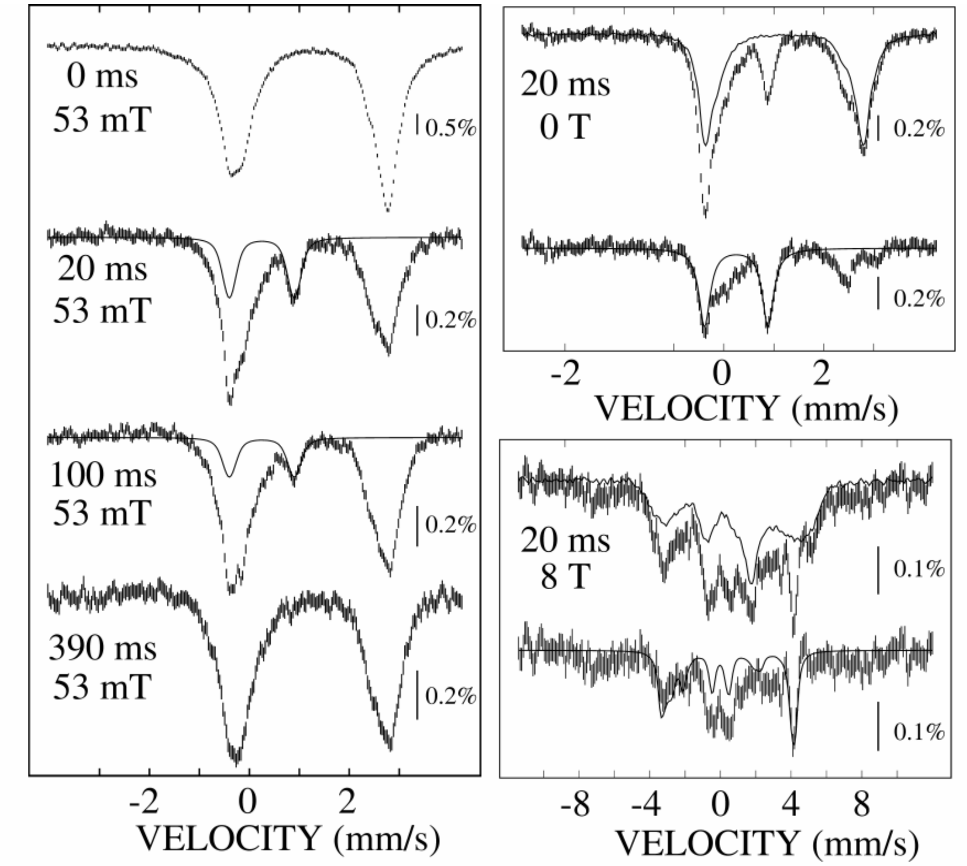

FIGURE 4. Mössbauer spectra at 4.2-K of the reaction at 5 °C of the TyrH:Fe(II):6MPH$_4$:Tyr complex with oxygen-containing buffer. Reaction times and magnetic field strengths are as indicated. Left panel: spectra (hashed marks) at various reaction times. The solid lines are quadrupole doublet simulations of the spectra of the Fe(IV) intermediate (δ = 0.25mm/s and ΔE_Q =1.27 mm/s). Right panel: deconvolution of the spectrum of the 20-ms sample in zero-field (top panel) and an 8-T field (bottom panel). The spectrum of the anaerobic control scaled to 60% of the total intensity is shown as a solid line overlaid with the raw data at the top spectrum within each panel. The hashed lines in the below spectra within each panel are the difference spectra that were obtained by subtracting the solid line from the hashed line at the top spectra. The solid line in the below spectrum is the simulation of the difference spectra for the Fe(IV) intermediate (24% intensity) with the following spin Hamiltonian parameters: S = 2, D = 12.5 cm^{-1}, E/D = 0.05, δ = 0.25 mm/s, ΔE_Q = -1.27 mm/s, η = -0.5, $\mathbf{A}/g_N\beta_N$ = (-18.0, -18.0,-31.0) T.

In the samples collected at times from 20 ms to 150 ms, a new line at ~0.9 mm/s is present. This peak exhibits a quadrupole doublet in a weak external magnetic field, and the second line of the doublet overlaps with the low-energy line of the Fe(II) doublet at -0.5 mm/s, which is apparent from the higher intensity of this line than the high-energy band of the Fe (II) complex at +2.8mm/s. These parameters are similar to those observed in other mononuclear non-heme enzymes for Fe(IV) intermediates (*45*).

To characterize this intermediate further, spectra of the 20-ms sample (this sample contains a maximum amount of the intermediate, 24% of total Fe) were recorded without an applied field (Figure 4, top right panel) and with an 8-T applied field (bottom right panel). The spectrum of the 20-ms sample is shown as the top spectrum in each panel (vertical bars). Removal of the spectral contribution of the starting material (55% of the total intensity, shown as a solid line in the top spectra) results in the spectra depicted as vertical bars (lower spectrum in each panel). The zero-field spectrum reveals the position of the low-energy line and allows the isomer shift (δ) and quadrupole splitting (ΔE_Q) of the intermediate to be determined: δ = 0.25 mm/s and ΔE_Q = 1.27 mm/s. These parameters are similar to those experimentally observed (*45, 53*) and theoretically predicted (*66, 67*) for non-heme Fe(IV) intermediates, suggesting the presence of such a complex in TyrH. In addition, the spectrum reveals two broad lines at 0 and 2.4 mm/s. These features are associated with a new high-spin Fe(II) complex formed during the reaction.

The 8-T spectrum provides further insight into the electronic structure of the Fe(IV) intermediate. In particular, the sharp line at 4 mm/s is associated with the intermediate and not the reactant complex. The spectrum resulting after removal of the

55%-contribution of the reactant complex reflects the Fe(IV) intermediate (24%) and a new high-spin Fe(II) complex (20%). The contribution of the Fe(IV) complex was simulated according to the spin Hamiltonian formalism with parameters typical of high-spin Fe(IV) complexes (*45, 53, 66, 68*).

RFQ EPR. The RFQ-EPR sample that was quenched after 20 ms in the same way and conditions as the Mössbauer sample was reduced by gamma radiation at 77 K and the EPR spectrum was taken. The resulting spectrum shows features at $g = 4.3$ region that are specific to Fe(III) (Figure 5). This suggests that Fe(IV) was present in the freeze-quenched sample and Fe(III) formed upon cryoreduction. Similar results have been obtained for other non-heme Fe(IV)O intermediates (*57*).

Rapid Chemical Quench. The anaerobic complex of TyrH:Fe(II):Tyr:6-MPH_4 (500 μM TyrH, 480 μM Fe(II), 1 mM Tyr, and 2 mM 6-MPH_4) was reacted with an equal volume of oxygen containing buffer (1.9 mM) in the same way as for the Mössbauer study, except the reaction mixture was quenched by concentrated acid (5 M HCl) instead of cryosolvent. The samples collected at various time points were analyzed by a colorimetric DOPA assay (*36*). The time-dependent data obtained from this analysis could be fit reasonably well as a single exponential increase with a rate constant of 15 ± 2 s^{-1}. This is significantly faster than the k_{cat} value at this temperature. The kinetics of formation of both DOPA and the Fe(IV) species were then analyzed according to the mechanism of Scheme 5, with the single rate constant for DOPA formation as an initial estimate. In this kinetic mechanism, the first step is the concomitant formation of Fe(IV)O and 4a-hydroxypterin. Fe(IV)O and tyrosine then react to form the product DOPA. Both time courses were well fit with values for the rate constants k_1 and k_2 of 24 and 35 s^{-1}, respectively, consistent with the Fe(IV) intermediate being the hydroxylating species (Figure 6).

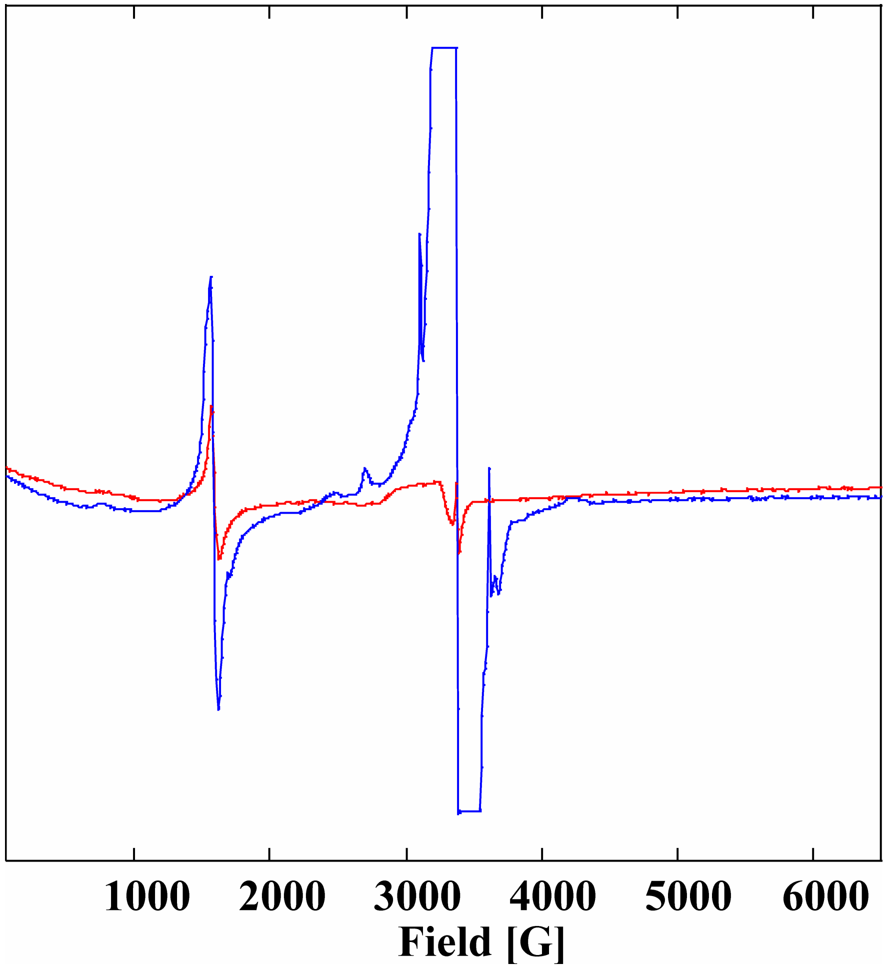

Figure 5. X-band EPR spectra of a sample in which the TyrH:Fe(II):6MPH$_4$:Tyr complex was reacted with an O_2-saturated buffer solution for 20 ms (the experimental conditions are identical to those reported for the Mössbauer sample). The spectra were recorded before (red) and after (blue) γ-irradiation of the sample at 77 K with a ^{60}Co source (total radiation dose: 3.5 MRad). Spectrometer conditions are given in Experimental Procedures.

Scheme 5

$$\text{TyrH:Fe(II):Tyr:6MPH}_4\text{:O}_2 \xrightarrow{k_1 = 24\ \text{s}^{-1}} \text{TyrH:Fe(IV)O:Tyr} + \text{4a-HO6MPH}_3$$

$$\text{TyrH:Fe(IV)O:Tyr} \xrightarrow{k_2 = 35\ \text{s}^{-1}} \text{TyrH:Fe(II)} + \text{DOPA}$$

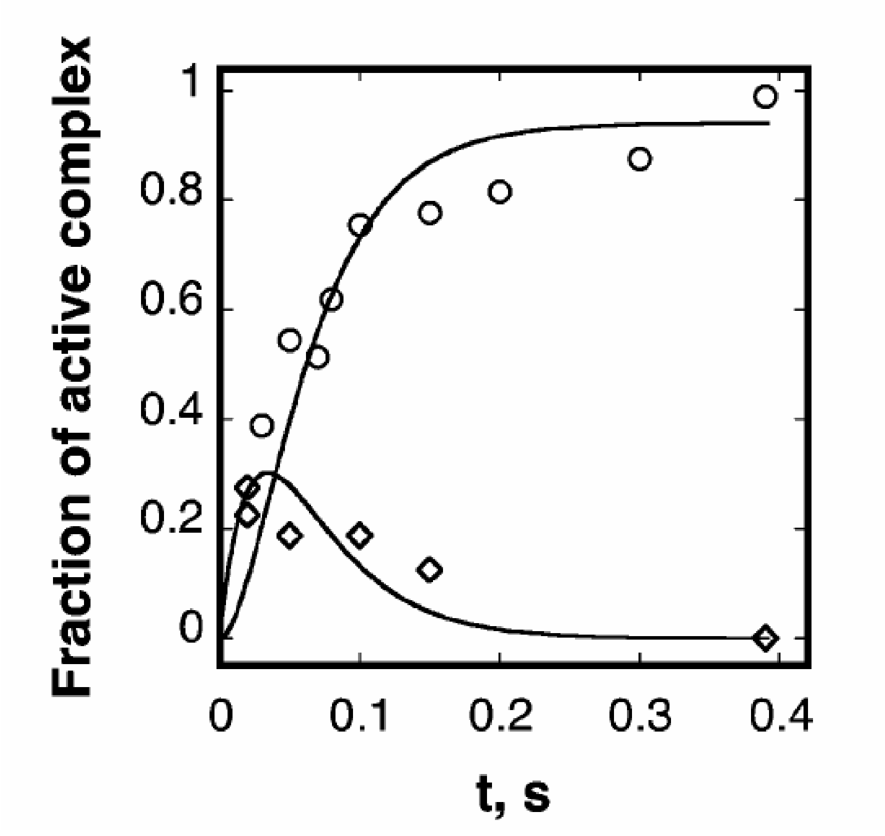

FIGURE 6. Comparison of time courses for Fe(IV)O formation and decay (diamonds) and for DOPA formation (circles). DOPA was quantified by rapid-quench of the reaction at 5 °C of the complex of 500 μM TyrH, 480 μM Fe(II), 1 mM Tyr, and 2 mM 6MPH$_4$ with an equal volume of 1.9 mM oxygen-containing buffer. The lines are simulations using the mechanism of Scheme 5 and values of k_1 and k_2 of 24 s^{-1} and 35 s^{-1}, respectively, assuming that 80% of the enzyme complex is active.

Stopped-Flow Absorbance Spectroscopy. Investigation of the kinetics of the possible intermediates with diagnostic absorbance signatures was carried out using stopped-flow absorbance spectroscopy. The progress of the reaction of an anaerobic solution of TyrH:Fe(II):Tyr:6-MPH_4 in 200 mM Hepes, 10% glycerol and 0.1 M KCl, pH 7.5, with an equal volume of the same buffer containing oxygen (950 µM final) at 5 °C was monitored by the stopped-flow spectrophotometer. The absorbances of the pterin species (*69*) which form during the course of the reaction were dominant in single wavelength traces from 240 nm to 450 nm (*57*). Traces for the absorbance changes at 248 nm, where 4a-hydroxypterin has the largest change, and for 300 nm-350 nm, where both 4a-hydroxypterin and quinonoid dihydropterin absorb, were analyzed using the global fitting software DynaFit (*65*) as described in Experimental Procedures.

Absorbance changes up to 1 s at 248 and 318 nm exhibit biphasic pattern. Global simulation of these traces to a two-step mechanism given in Scheme 6 accounted well for the data (Figure 7). Since 4a-hydroxypterin and Fe(IV)O should form concomitantly (Scheme 3), the rate constant (24 s^{-1}) obtained for the formation of Fe(IV) from RFQ Mössbauer and chemical quench time courses (Scheme 3) was directly used for the first rapid phase in the simulation analysis. A slower second step with a rate constant of 1.4 s^{-1} is necessary to account for the absorbance changes of the second phase. The extinction changes of each step used for the simulation analysis are given in Table 1.

Scheme 6

$$\text{TyrH:Fe(II):Tyr:6MPH}_4\text{:O}_2 \xrightarrow{\mathbf{k_1 = 24\ s^{-1}}} \text{TyrH:Fe(IV)O:Tyr} + \text{4a-HO6MPH}_3^{*}$$

$$\text{4a-HO6MPH}_3^{*} \xrightarrow{\mathbf{k_2 = 1.4\ s^{-1}}} \text{4a-HO6MPH}_3$$

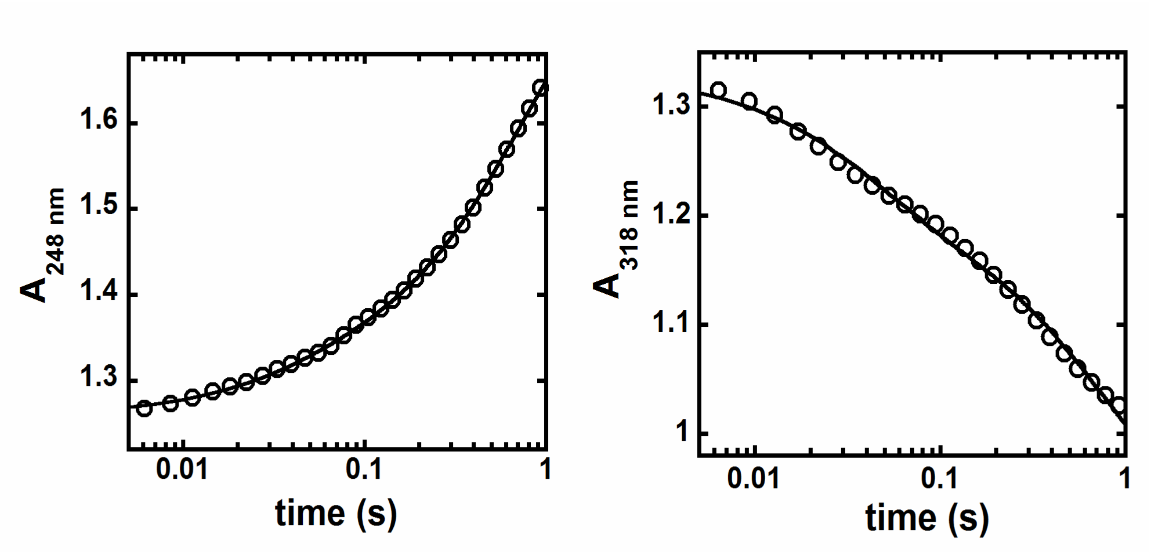

FIGURE 7. Stopped-flow absorbance traces at 248 nm (left) and at 318 nm (right), acquired by mixing an anaerobic solution of TyrH:Fe(II):Tyr:6-MPH$_4$ in 200 mM Hepes, 10% glycerol and 0.1 M KCl, pH 7.5, with an equal volume of the same buffer containing oxygen (950 µM final) at 5 °C. The concentrations after mixing were 35 µM TyrH:Fe(II), 80 µM Tyr and 80 µM 6-MPH$_4$ for the 248 nm trace, and 100 µM TyrH:Fe(II), 235 µM Tyr and 235 µM 6-MPH$_4$ for the 318 nm trace. Experimental data are shown as circles. Solid lines are the simulations using the mechanism and rate constants shown in Scheme 6 as described in Experimental Procedures.

Table 1. Rate Constants and Extinction Changes Obtained from the Global Kinetic Analysis of the Stopped-Flow Data Traces for the Reaction of TyrH.

Step	Rate Constant (s^{-1})	$\Delta\varepsilon_{248nm}$ ($M^{-1}cm^{-1}$)	$\Delta\varepsilon_{318nm}$ ($M^{-1}cm^{-1}$)
k_1	24 s^{-1}	+2400	-1400
k_2	1.4 s^{-1}	+11700	-2400

DISCUSSION

A high-valent Fe(IV)O species has for long been proposed to be the hydroxylating intermediate in the reaction of TyrH. Although there is extensive spectroscopic data demonstrating the involvement of such an intermediate in heme enzymes and dinuclear non-heme enzymes (*53-56*), the first direct evidence for the presence of an Fe(IV)O intermediate in a mononuclear non-heme system has only become available very recently (*57*). Similarities between the reactions catalyzed by TyrH and the enzyme systems that use Fe(IV)O as intermediates (*21*) strongly suggest the involvement of Fe(IV)O as the hydroxylating species in TyrH reaction, encouraging us to carry out rapid reaction studies in conjunction with spectroscopy for direct characterization of this intermediate.

RFQ Mössbauer spectroscopy, a powerful technique for kinetic and chemical characterization of iron-based intermediates (*53*), has been used to obtain evidence for the presence of an Fe(IV)O intermediate in TyrH reaction. Mössbauer spectroscopic analysis of the samples collected by rapid freeze quench clearly demonstrate that an Fe(IV) species indeed forms during the catalytic cycle of TyrH. Samples collected at various time points for Mössbauer spectroscopic analysis also allowed kinetic analysis of the intermediate. The highest amount of Fe(IV), about 20% of the starting complex, was quantified for the 20 ms sample, and the signal for Fe(IV) had decayed almost completely at 390 ms. Mössbauer analysis of the 20 ms sample at zero magnetic field allowed the isomer shift (δ) and quadrupole splitting (ΔE_Q) parameters to be calculated as 0.25 mm/s and -1.27 mm/s, respectively. Further analysis of this 20 ms sample at high magnetic field (8 T) is in agreement with a high spin (S=2) Fe(IV).

Although some Fe(III) species can give isomer shift values in a similar range to that of TyrH, these Fe(III) species are generally low spin and are not expected to give a quadrupole doublet at low magnetic field. In addition, the Mössbauer parameter values obtained for TyrH are very similar to the parameters observed for the Fe(IV)O intermediates in TauD, prolyl-4-hydroxylase and cytc3 halogenase (Table 2) (*57, 70, 71*). In the case of TauD, the evidence provided by Mössbauer spectroscopy for the presence of an Fe(IV)O intermediate was supported by additional experiments. The continuous-flow resonance Raman spectrum of the intermediate exhibits a stretching mode characteristic of Fe(IV)=O, and EXAFS spectra show the appropriate bond distance for a Fe(IV)=O unit (*58, 59*). RFQ EPR spectroscopy further supports the presence of an Fe(IV) intermediate in TyrH reaction. The cryoreduced sample showed increased signal intensity at g=4.3, which is characteristic of an Fe(III) species. This can only occur if there is Fe(IV) present in the sample before cryoreduction. One-electron reduction of Fe(IV) will then result in Fe(III), giving increased intensity for g=4.3 signal. A similar result was also observed with TauD (*57*).

Table 2. Comparison of Mössbauer Parameters of TyrH with Those of Other Mononuclear Non-heme Systems.

Enzyme	**δ (mm/s)**	**ΔE_Q (mm/s)**
TyrH	0.25	-1.27
TauD[a]	0.31	-0.88
Prolyl-4-hydroxylase[b]	0.30	-0.82
Cytc3 halogenase[c]	0.30	-1.09

[a] Reference *36*. [b] Reference *69*. [c] Reference *70.*

Although the RFQ Mössbauer and RFQ EPR experiments showed direct evidence for the involvement of an Fe(IV) intermediate in TyrH reaction, they do not provide direct support for this species to be the proposed hydroxylating intermediate, Fe(IV)O. According to the proposed mechanism (Scheme 3), the initial reaction of Fe(II), O_2 and tetrahydropterin leads to the formation of an iron μ-peroxypterin bridge. The heterolytic cleavage of this intermediate should result in Fe(IV)O and 4a-hydroxypterin concomitantly. In the next step of the reaction, the electrophilic attack of Fe(IV)O on the aromatic ring of tyrosine gives the product DOPA. If the Fe(IV) intermediate detected by Mössbauer spectroscopy is indeed the hydroxylating species, the decay of this intermediate should be coupled to DOPA formation. In agreement with this proposal, the Fe(IV) formation and decay and DOPA formation kinetics can be simulated globally (Figure 6) according to the mechanism in Scheme 5, supporting the kinetic competency of Fe(IV) intermediate as the hydroxylating species.

Stopped-flow analysis of the reaction of TyrH further suggests that the Fe(IV) intermediate observed by Mössbauer spectroscopy is indeed the postulated Fe(IV)O species. Since the formation of the Fe(IV)O intermediate and 4a-hydroxypterin occur in the same step, the kinetics for their formation should also be identical. Pterin species have unique absorbances in 200-450 nm region (*69*). The global kinetic analysis of the stopped-flow data traces at 248 and 318 nm are in good agreement with a two-step mechanism (Scheme 6). The signs of the absorbance changes at both wavelengths (an increase at 248 nm and a decrease at 318 nm) for this step are in agreement with the known absorbance spectra of 4a-hydroxypterin (*69, 72, 73*). These observations support the conclusion that this first rapid step is the formation of 4a-hydroxypterin and Fe(IV)O upon cleavage of the putative iron μ-peroxypterin bridged intermediate.

When compared to the reported spectra of pterin species in solution (*69*), the magnitudes of absorbance changes for the first step are less than those that would be expected for the formation of 4a-hydroxypterin species (Table 1). This difference suggests that either the spectrum of 4a-hydroxypterin is perturbed inside the enzyme active site or the initial pterin product from the heterolytic cleavage of the iron μ-peroxypterin bridge is a deprotonated form, thus leading to smaller extinction changes. In fact, a second step with a rate constant of 1.4 s^{-1}, a value close to the k_{cat} of the catalysis, is needed to account for the later time points (up to ~1 s), and the sum of the absorbance changes associated with the first and the second steps match the change that would be expected for the formation of 4a-hydroxypterin from $6MPH_4$ in solution at neutral pH (*72, 73*). This strongly implies that this step is either protonation of 4a-hydroxypterin or release of 4a-hydroxypterin from the active site of the enzyme.

Although studies with TauD revealed that formation of Fe(IV)O is associated with an increasing absorbance change at 318 nm (*57*), no such absorbance pattern related with the formation of Fe(IV) species has been observed for TyrH reaction. A reasonable explanation is that in the case of TauD, Fe(II) is coordinated by the α-KG cofactor in addition to the protein derived facial triad, whereas for TyrH, there are not any external ligands present other than water molecules. Given the different iron environments, the absorbance spectra for Fe(IV)O in TyrH and TauD might be quite different. However, investigation of the 200-500 nm region did not reveal any absorbance change that might be attributed to an Fe(IV)O intermediate. It is very likely that any absorbance from an Fe(IV)O species is being obscured by the highly absorbing pterin species in this wavelength region.

When the results of kinetic analysis from the RFQ Mössbauer, rapid chemical quench and stopped-flow experiments are taken together, the mechanism and rate constants presented in Scheme 7 can be established for TyrH reaction. The first step is the concomitant formation of Fe(IV)O and 4a-hydroxypterin. Then, the Fe(IV)O species attacks tyrosine to give DOPA and the resting form of the enzyme. The third step represents a change in the state of 4a-hydroxypterin that forms in the first step. This might be either product release or a protonation event.

Scheme 7

$$\text{TyrH:Fe(II):Tyr:6MPH}_4\text{:O}_2 \xrightarrow{\boldsymbol{k_1 = 24\ \mathrm{s}^{-1}}} \text{TyrH:Fe(IV)O:Tyr} + \text{4a-HO6MPH}_3^{*}$$

$$\text{TyrH:Fe(IV)O:Tyr} \xrightarrow{\boldsymbol{k_1 = 35\ \mathrm{s}^{-1}}} \text{TyrH:Fe(II)} + \text{DOPA}$$

$$\text{4a-HO6MPH}_3^{*} \xrightarrow{\boldsymbol{k_2 = 1.4\ \mathrm{s}^{-1}}} \text{4a-HO6MPH}_3$$

Overall, this work shows direct spectroscopic evidence for a high-spin Fe(IV) species, presumably the postulated Fe(IV)O, as the hydroxylating intermediate in the reaction catalyzed by TyrH. This is the first example for this family of enzymes as well as the first for a mononuclear nonheme enzyme which catalyzes aromatic hydroxylation.

CHAPTER III

MECHANISTIC INSIGHT INTO O_2 ACTIVATION: SPECTROSCOPY AND KINETICS OF WILD-TYPE AND MUTANT TYROSINE HYDROXYLASE*

INTRODUCTION

The aromatic amino acid hydroxylases (AAH) is a small family of mononuclear non-heme enzymes (*15, 16*). The members of this family use tetrahydropterin as a cofactor for hydroxylation of their amino acid substrates. Tyrosine hydroxylase (TyrH) catalyzes conversion of tyrosine to dihydroxyphenylalanine (DOPA), as the first and the rate limiting step in the biosynthesis of catecholamine neurotransmitters (dopamine, adrenaline and noradrenaline). TyrH is found in the brain and adrenal gland. A deficiency of this enzyme leads to various neurological disorders such as DOPA-responsive Parkinson's disease, progressive encephalopathy, DOPA-non-responsive dystonia and DOPA-responsive dystonia (Segawa's disease) (*17, 18*). The other members of the family include phenylalanine hydroxylase (PheH) and tyrptophan hydroxylase (TrpH). PheH is a liver enzyme and catalyzes hydroxylation of phenylalanine to tyrosine. TrpH, the rate-limiting enzyme in the biosynthesis of serotonin, converts tyrptophan to 5-hydroxytryptophan and is found in the central nervous system.

---

*Reproduced in part with permission from Chow, M. S., Eser, B. E., Wilson, S. A., Hedman, B., Hodgson, K. O., Fitzpatrick, P. F., and Solomon, E. I. *J.Am.Chem.Soc.* **2009**, *131*, 7685–7698. Copyright 2009 American Chemical Society.

All members of the AAH family share a similar mechanism (*38-41*). The mechanism involves formation of the hydroxylating intermediate, Fe(IV)O and subsequent attack of this intermediate on to the aromatic ring to give the product, DOPA, through electrophilic aromatic substitution (*21*). One important aspect of the reaction of TyrH and other members of AAHs is that for each product molecule formed, a pterin molecule is oxidized. This gives 100% coupling between DOPA formation and pterin oxidation for the WT reaction. Certain mutations and use of unnatural substrates lead to uncoupling, which means more pterin being oxidized than the hydroxylated amino acid product being formed (*21, 29, 37*). Another crucial requirement for this family of enzymes is that both cofactor and substrate must be bound before any catalytically relevant reaction takes place between iron, oxygen and pterin (*21*).

Although formation and reactivity of the hydroxylating intermediate, Fe(IV)O, has been explored with recent studies as described in Chapter II, the effects of substrate and cofactor binding on the electronic and geometric structure of the active site and initial reactivity of Fe(II) with oxygen have not been studied in detail. Steady-state studies with TyrH demonstrated a binding sequence of tetrahydropterin binding first and then oxygen second, followed by tyrosine, before any catalytic reaction occurs (*36*). The crystal structure of PheH with both substrate and cofactor bound shows significant changes of the active site in comparison to pterin bound binary complex (*25, 30*). The Fe(II) site becomes 5-coordinate and the glutamate ligand becomes bidentate. XAS and MCD studies with PheH support this observation (*31, 74*). However, there is no such crystal structure available yet for TyrH. Crystal structures of the resting form and oxidized pterin-bound forms of TyrH with Fe(III) show 5C ligation with a similar pattern including two His, one Glu and two water molecules (*23, 27*). In contrast, earlier XAS studies showed that both resting Fe(II) and tetrahydrobiopterin bound TyrH:Fe(II) are 6C (*75*). In order to gain more insight into the structure/reactivity relationship, the electronic and geometric structures of the Fe(II) active site in various TyrH complexes were investigated by means of MCD and XAS spectroscopies in collaboration with Dr. Edward I. Solomon's lab at Stanford University. The kinetics of oxygen reactivity of these complexes was then analyzed by stopped-flow absorption spectroscopy, enabling us to correlate active site structure to reactivity.

EXPERIMENTAL PROCEDURES

Materials. 6-Methyltetrahydropterin ($6MPH_4$) was purchased from Schircks Laboratories (Jona, Switzerland). L-tyrosine and glycerol were from Sigma-Aldrich (St. Louis, MO). D_2O and glycerol-d_3 were from Cambridge Isotopes (Andover, MA). Potassium chloride, EDTA, Hepes, Mops and ferrous ammonium sulfate were from Fisher (Pittsburg, PA). Amicon Ultra-15 and Ultra-4 centrifugal filters were obtained from Millipore Corp. (Billerica, MA). All other chemicals were of the highest purity commercially available.

Enzyme Purification and Preparation. WT, E332A, and S395A rat TyrH were overexpressed in *Escherichia coli* and purified as previously described (*29, 37, 61*). After purification, the enzyme was precipitated with 70% ammonium sulfate. The enzyme samples for stopped-flow spectroscopy were prepared by dissolving the ammonium sulfate pellet in 200 mM Hepes (pH 7.5), 10% glycerol, 0.1 M KCl and 5 mM EDTA. After incubation with this buffer for an hour, the enzyme was dialyzed against the same buffer without EDTA. The enzyme samples for MCD were prepared by dissolving the ammonium sulfate pellet in deuterated Mops (100 mM)/KCl (300 mM) buffer, pD 7.3, (containing either 5 mM EDTA for WT and E332A or 1 equiv of ferrous ammonium sulfate per monomer for S395A), followed by dialysis against the same buffer. At the end of the dialysis, enzyme samples were centrifuged at 15 K to remove the precipitated protein. The samples were then transferred to Amicon Ultra-15 centrifugal filters (Millipore Corp., MA) for concentration process. After a concentration of ~ 1 mM is achieved, glycerol-d_3 was added to a final concentration of 30% (v/v) and the centrifugation process was continued till a concentration of ~2 mM is reached. At this stage more glycerol-d_3 was added bringing the final buffer condition to 100 mM MOPS, pD 7.3, 65% glycerol-d_3 and 300 mM KCl. The samples were transferred to smaller centrifugal filters (Amicon Ultra-4) and subjected to more centrifugation until a final enzyme concentration of ~1.5 mM is reached. The samples for XAS were prepared in the same way as the MCD samples, except that buffer conditions were 100 mM Hepes (pH 7.0), 300 mM KCl and the final concentration of glycerol was 50%. The concentration of TyrH was determined using an extinction coefficient of 58.24 $mM^{-1}cm^{-1}$ at 280 nm. The iron content of the apo-enzyme was measured using a Perkin-Elmer AAnalyst600 atomic absorption instrument. Typical iron content of an apo enzyme preparation was ~0.1 equivalent.

Preparation of XAS and MCD Samples. XAS and MCD samples were prepared by Dr. Marina Chow, in the laboratory of Dr. Edward I. Solomon at Stanford University. Samples for spectroscopy included resting enzyme (TyrH-[ ]), enzyme with only tyrosine bound (TyrH-[L-tyr]), enzyme with only $6MPH_4$ bound (TyrH-[$6MPH_4$]), enzyme with only 5-deaza-6MPH$_4$ bound (TyrH-[5-deaza-6MPH$_4$]) and ternary enzyme complex with both tyrosine and 6MPH$_4$ bound (TyrH-[L-tyr, 6MPH$_4$]). The samples typically contained 0.8-2 mM TyrH, ~0.85 equivalent of ferrous ammonium sulfate, 2-5 mM tyrosine, 3-5 mM 6MPH$_4$ (or 5-deaza-6MPH$_4$) and approximately 60% v/v glycerol-d_3. 6-Methyltetrahydropterin was dissolved in an anaerobic solution of 10 mM HCl. The concentration of the 6MPH$_4$ stock solution was determined from the absorbance at 266 nm (ε_{266nm} = 17.8 mM^{-1}cm^{-1}). The redox inactive cofactor 5-deaza-6MPH$_4$ was synthesized according to literature procedures (*76*). Concentrated solutions of L-tyrosine (L-tyr) were prepared in D_2O adjusted to pD = 10 using NaOD. After the apo enzyme solution was made anaerobic, ferrous ammonium sulfate was added, followed by reducing equivalent of dithionite. The TyrH:Fe(II) samples were incubated for 10 minutes, then tyrosine and 6MPH$_4$ were added as needed and the samples incubated for another 10 to 20 minutes. After removal from the glovebox, the samples were frozen in liquid nitrogen.

XAS and EXAFS. X-ray absorption spectra were recorded at Stanford Synchrotron Radiation Laboratory (SSRL) in collaboration with Dr. Keith O. Hodgson and Dr. Britt Hedman. Experiments and data analysis were carried out by Samuel A. Wilson of Stanford University.

MCD Spectroscopy. Low temperature near-IR MCD data were collected (using a Jasco J200D spectropolarimeter, 600 – 2000 nm) and analyzed (using the program PeakFit, SPSS Science) by Dr. Marina Chow, in the laboratory of Dr. Edward I. Solomon at Stanford University.

Single Turnover Kinetics. Single turnover reactions of WT TyrH and E332A TyrH were monitored using an Applied Photophysics SX20 stopped-flow spectrophotometer in single wavelength absorbance mode. The stopped-flow instrument was made anaerobic by incubation with a solution of excess sodium dithionite for at least two hours. Concentrated stock solution of tyrosine (~20 mM) was prepared by bringing the solution to a final pH of ~10. The concentration of the tyrosine stock solution was determined using an extinction coefficient of 1.34 $mM^{-1}cm^{-1}$ at 275 nm in 0.1 M HCl. Stock solution of $6MPH_4$ (~40 mM) was prepared in 2 mM HCl and an extinction coefficient of 17.8 $mM^{-1}cm^{-1}$ in 2 M perchloric acid was used to determine the concentration. Ferrous ammonium sulfate solutions were prepared fresh by dissolving the appropriate amount of powder in 2 mM HCl. A solution of ~300 μM apo-TyrH and 500 μM tyrosine in 200 mM Hepes (pH 7.5), 10% glycerol and 0.1 M KCl was made anaerobic in a tonometer on ice, through at least 20 argon-vacuum cycles. Ferrous ammonium sulfate (0.9 equivalent of enzyme) was then added to the tonometer under argon. $6MPH_4$ (final 2 mM in tonometer) was placed in the side arm of the tonometer under argon. Additional argon-vacuum cycles were performed prior to mixing the $6MPH_4$ solution with the tonometer contents, which was then loaded to one of the syringes of the stopped-flow instrument. Different oxygen concentrations in buffers were achieved by using a modified MaxBlend medical oxygen blender (Maxtec) to mix argon and oxygen in different ratios and then bubbling through buffer-containing syringes on ice for at least 15 min. The buffer-containing syringes were then attached to the second syringe of the instrument. Data was collected at 5 °C. Concentrations specific to each experiment are given in figure legends. Single wavelength absorbance changes consisted of one or more exponential kinetic phases, which were analyzed by first fitting to single or multiple exponentials using the program KaleidaGraph (Synergy Software); results from these fits were than taken as initial estimates for global fits and simulations. Initial values for k_{on} and k_{off} for the reversible oxygen complex formation steps and estimates for unknown extinction coefficients were determined by global fitting of multiple traces (obtained at multiple wavelengths for varying O_2 concentrations) using the program DynaFit (*65*). Initial concentrations were allowed to float within 10% of the experimental values. The global fitting process was performed in an iterative fashion, in which one or two parameters were varied at a time and the rest of the parameters were kept constant. Best fit parameters obtained this way were than employed for the kinetic simulation (DynaFit) of the experimental data to appropriate mechanisms. Further details are given in figure legends of each simulation.

RESULTS

X-ray Absorption Spectroscopy: Pre-Edge. The pre-edge and edge spectra of four TyrH complexes are shown in Figure 8. Energy bands and intensity values for each complex, obtained by fitting pre-edge peaks, are given in Table 3. Total intensities for TyrH-[ ], TyrH-[$6MPH_4$], and TyrH-[L-tyr] are larger than typical values observed for O_h 6C model complexes with uniform ligation, but they are similar to those found for 6C structures in Fe(II) metalloenzymes (*32, 75, 77, 78*). The normalized data for TyrH-[ ] (resting, in red), TyrH-[L-tyr] (substrate, in blue) and TyrH-[$6MPH_4$] (cofactor, in orange) all look very similar in terms of pre-edge shape and intensity. When both cofactor and substrate are present, TyrH-[L-tyr, $6MPH_4$] (green), the pre-edge shows a significant increase in intensity and a shift to lower energy both of which are reflected in the second derivative (Figure 8, inset). This pattern is similar to the 4 units of increase in intensity observed for model complexes in which going from 6C to 5C distorts the ligand field of the Fe(II) (*79*). There is also difference in the edge slope as well as the maximum intensity of the rising edge. In addition, small differences are observed at higher energies above the edge (7150 eV in Figure 8), suggesting that a structural change has occurred when both substrate and cofactor are bound to TyrH.

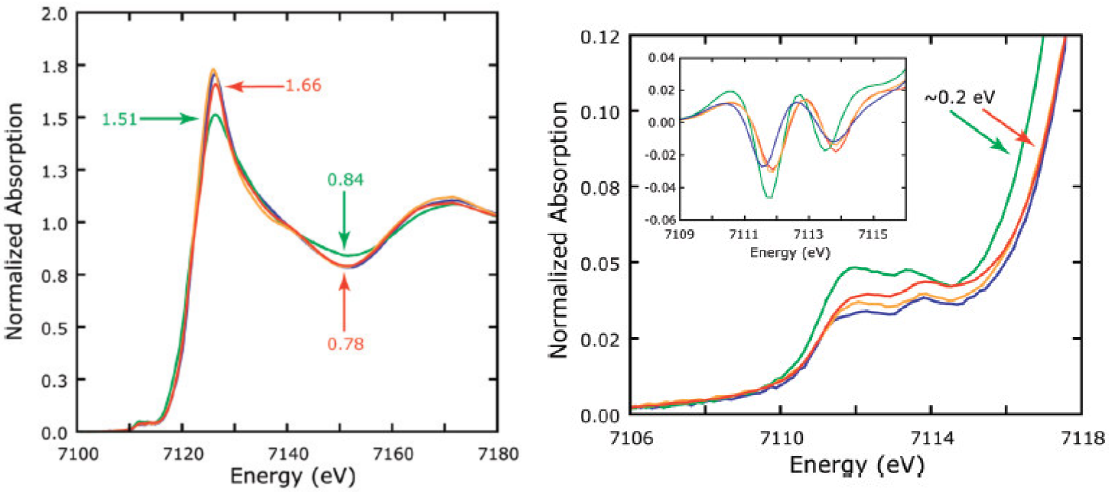

FIGURE 8**.** Fe K edge spectra (Left) and enlarged pre-edge (Right) regions of TyrH-[ ] (red), TyrH-[L-tyr] (blue), TyrH-[6MPH$_4$] (orange) and TyrH-[L-tyr, 6MPH$_4$] (green). The inset shows the smoothed 2nd derivatives of the pre-edge spectra (2nd derivative smoothed for clarity, smoothing = 0.5).

Table 3. XAS Pre-edge Energies and Intensities.[a]

Sample	Peak (eV)	Area	Total Intensity
TH-[ ]	7112.0	4.4	8.3 ± 0.6
	7113.8	3.9	
TH-[L-tyr, 6MPH$_4$]	7111.8	6.4	12.5 ± 1.5
	7113.5	6.1	
TH-[6MPH$_4$]	7111.9	4.6	8.2 ± 0.7
	7113.8	3.6	
TH [L-tyr]	7111.9	4.4	8.5 ± 1.0
	7113.7	4.1	

[a] Pre-edge fit values obtained using EDG_FIT according to established methods. Peak energies are listed at peak maximum, areas are multiplied by 100 for comparison to other data. Total intensity is the sum of both areas. Error values calculated from total intensity standard deviations across all 9 fits per sample.

EXAFS. EXAFS data and their Fourier Transforms (FT) are shown in Figure 9. For all complexes, EXAFS data were collected to k = 15 Å^{-1} and fits were performed to k = 14 Å^{-1}, k = 13 Å^{-1}, k = 14 Å^{-1}, and k = 12 Å^{-1} for TyrH-[ ], TyrH-[L-tyr], TyrH-[6MPH$_4$] and TyrH-[L-tyr, 6MPH$_4$], respectively. 5C and 6C models based on the ferric crystal structure of tyrosine hydroxylase (PDB 1TOH) (*23*) were used for the fits. TyrH-[L-tyr, 6MPH$_4$] was also fit to a 5C model with a bidentate Glu (Figure 10), since a bidentate Glu has been observed in PheH-[L-phe, pterin] (*25*).

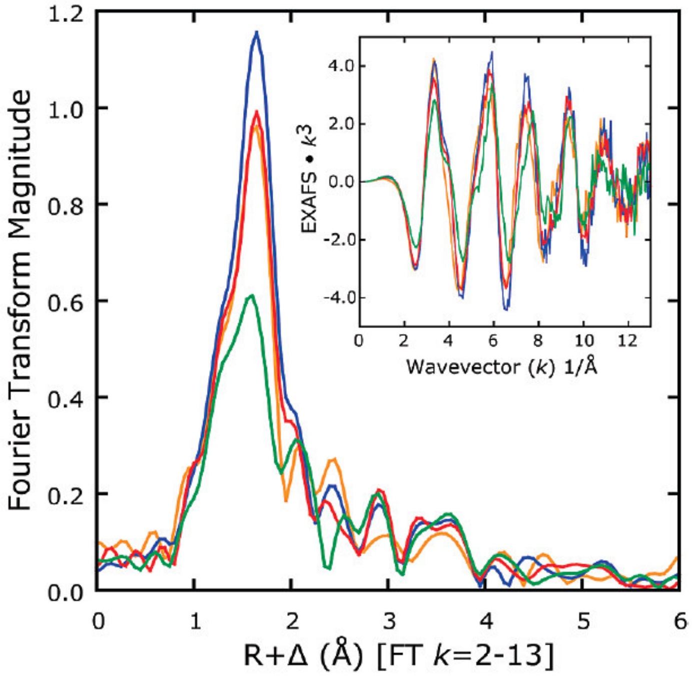

FIGURE 9. Fourier Transforms to $k = 13$ Å^{-1} for tyrosine hydroxylase. TyrH-[ ] (Red), TyrH-[L-tyr] (blue), TyrH-[6MPH$_4$] (orange) and TyrH-[L-tyr, 6MPH$_4$] (green). The inset shows EXAFS data for the respective samples.

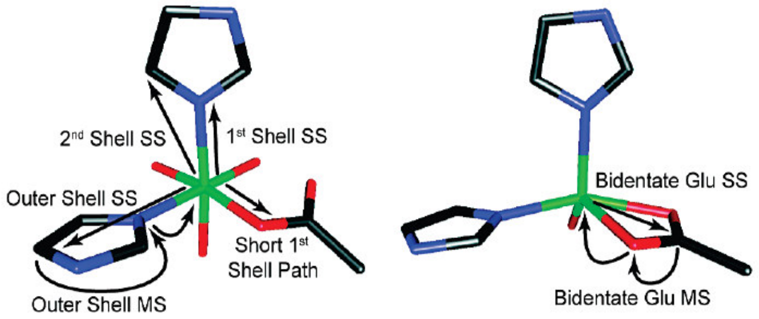

FIGURE 10. TyrH active site models for EXAFS fitting. The 6C model (left), based on active site crystal structure of TyrH:Fe(III) (PDB 1TOH), was used in fitting all EXAFS spectra. The 5C bidentate Glu model (right), from the crystal structure of the ternary complex of PheH (PDB 1MMT), was necessary for successful fitting of TyrH-[L-tyr, 6MPH$_4$]. The iron is shown in green, oxygen in red, carbon in black, and nitrogen in blue.

The EXAFS spectrum for TyrH-[ ] could be fit equally well either to a single 6C first shell where all 6 ligands have a bond distance of ~2.15 Å or to a split first shell in a 1:5 ratio with a bond distance of ~2.10 Å for the shorter bond and a distance of ~2.17 Å for the remaining 5 bonds. The 6C iron site is also supported by the pre-edge data for TyrH-[ ] (presented above) and by the MCD data *(vide infra)*. Fits to the EXAFS data when only cofactor is bound (TyrH-[6MPH$_4$]) are very similar to those of TyrH-[ ], with the best fit indicating a 6C split first shell (1:5 ratio) with a short bond distance of ~2.1 Å and longer distances of ~2.2 Å. When only substrate is bound, the best fit is the one in which all ligands are incorporated into one 6C shell at a single bond distance of 2.16 Å. Thus, TyrH-[ ], TyrH-[6MPH$_4$] and TyrH-[L-tyr] forms of tyrosine hydroxylase all contain a distorted 6C site.

A fit to a 5C first shell model of the EXAFS data for TyrH-[L-tyr, 6MPH$_4$] gives better overall results. There is also an additional single scattering feature at ~2.53 Å and an accompanying multiple scattering feature at 2.65 Å for outer shell. A best fit to the data is obtained in a split 5C model (2:3 ratio) with bond distances of ~2.05 Å and ~2.15 Å, taking into account that the additional outer shell features are due to presence of a bidentate glutamate as shown in Figure 10. A comparison of the residual waves for the monodentate and bidentate coordination modes (Figure 11) clearly shows that the fit to the bidentate Glu model accounts much better for the features at ~ 2.5 Å. The data do not support His dissociation and thus, the ligand which was lost is water, similar to the behavior observed in PheH (*31*).

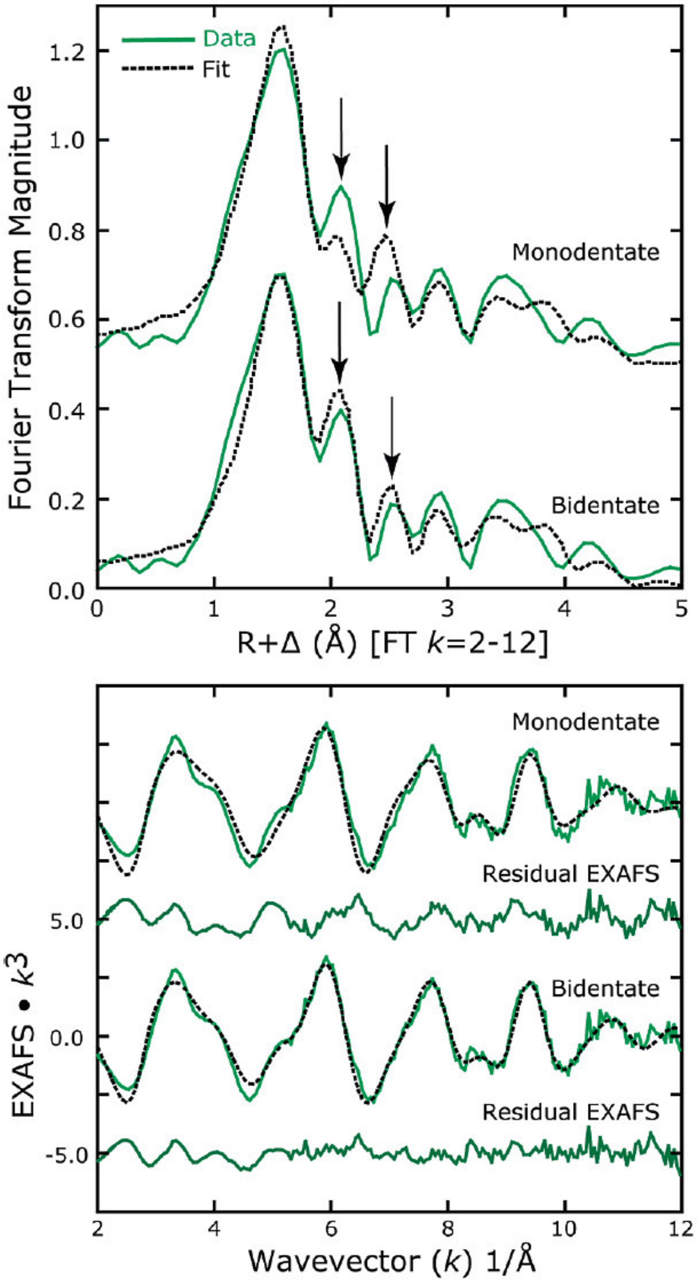

FIGURE 11. (Top) Comparison of Fourier Transforms of the EXAFS fits for the monodentate and bidentate Glu model, illustrating the requirement for a 2.5 Å signal coming from the fixed Glu carbon backscatter. (Bottom) k-space data, fits and residual corresponding to the Fourier transforms above.

MCD Spectroscopy of Wild-type Tyrosine Hydroxylase. MCD spectra of TyrH complexes are shown in Figure 12. Energy values of the two Gaussian bands that correspond to the excited state ligand field (d-d) transitions for each complex are listed in Table 4. For TyrH-[ ], two transitions are observed at around 10 000 cm^{-1} (split by 2030 cm^{-1}), indicating a 6C distorted octahedral ferrous site (*80*). The MCD spectra of TyrH-[L-tyr] and TyrH-[6MPH_4] are also consistent with both species having distorted 6C geometries. The narrower splitting and less intense high energy band observed in these spectra (Figure 12B and 12C) indicate slightly stronger ligand fields (10 *Dq* ~ 400 cm^{-1} higher in energy) and less axial distortion compared to TyrH-[ ]. In agreement with the XAS results (*vide supra*), MCD spectra also show that resting, substrate, or cofactor bound forms of TyrH are 6C.

In contrast, the pattern of the MCD spectrum of TyrH-[L-tyr, 6MPH_4] is consistent with the Fe(II) site being 5C. The spectrum exhibits only one band at 8960 cm^{-1} (Figure 12D), suggesting that the second transition expected at lower energy, should lie below the cutoff of the MCD instrument (*80*). The 5C site in TyrH-[L-tyr, 6MPH_4] complex is also supported by the the XAS results (*vide supra*) and by the VTVH MCD results presented in the next section. The < 10 000 cm^{-1} energy of the band is consistent with a trigonal bipyramidal site, but analysis of VTVH MCD data gives a +ZFS system indicating that the site is closer to square pyramidal (*81, 82*). The shift of the transition to less than 10 000 cm^{-1} suggests a strong axial perturbation to the iron site which would decrease the equatorial ligand field.

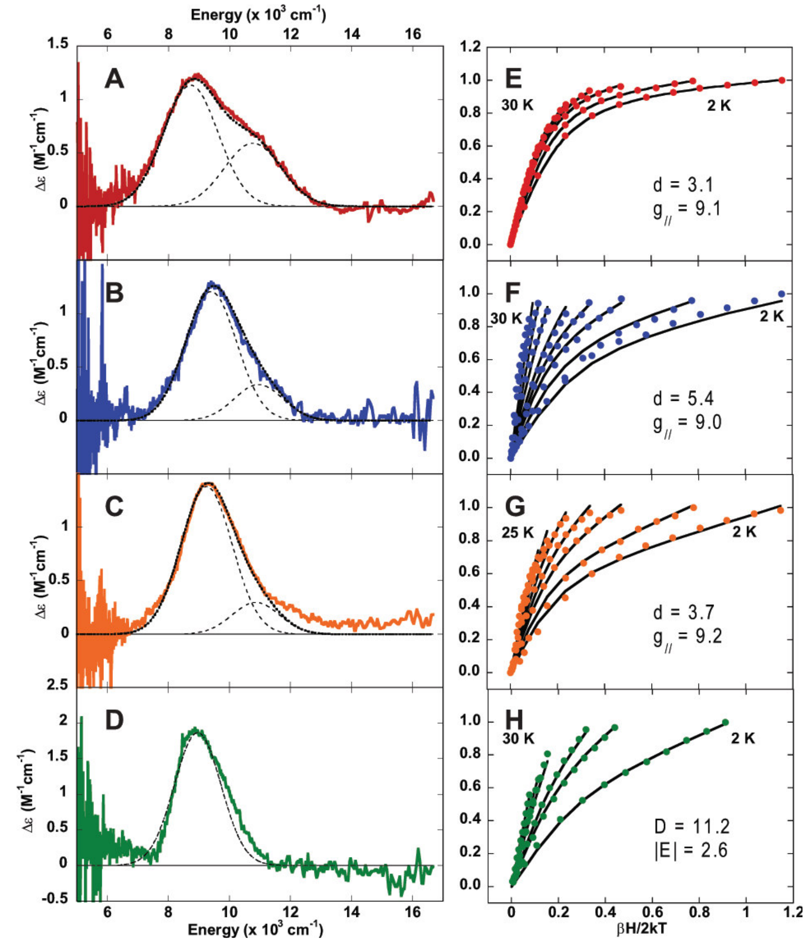

FIGURE 12. Near-IR MCD spectra (Left Panel) and saturation behavior (Right Panel) for TyrH-[ ] (A & E, in red), TyrH-[L-tyr] (B & F, in blue), TyrH-[6MPH$_4$] (C & G, in orange) and TyrH-[L-tyr, 6MPH$_4$] (D & H in green). In A, B and C, the sum of the Gaussian-resolved bandshapes (dotted lines) yield the generated spectrum (solid black lines), which reproduce the observed spectrum well.

VTVH MCD. The VTVH MCD spectra of TyrH complexes are shown in Figure 12E-H. Excited and ground state parameters obtained from the MCD and VTVH analyses are summarized in Table 4. The saturation data of the TyrH-[ ] bands exhibit a very small nesting (Figure 12E), which can be fit with a – ZFS model yielding $^5T_2$ ground state parameters with small t_{2g} d orbital splitting (Table 4). This is typical of a 6C Fe(II) site with moderate rhombic distortion ($|V/2\Delta| \sim 0.15$) (*80*). An experimental d-orbital energy level diagram for TyrH-[ ] can be constructed by combining the splitting of the $^5T_2$ ground state with the excited state splitting obtained from the MCD spectrum (Figure 13, left).

The VTVH MCD data for TyrH-[L-tyr] (Figure 12F) show increased nesting compared to resting TyrH, but still can be fit best as a –ZFS system. The spin-Hamiltonian and ground state parameters (Table 4) are indicative of an Fe(II) site with a higher degree of rhombicity, giving rise to larger splitting of the t_2 orbitals (*80*). As the earlier MCD data shows, tyrosine binding shifts the *e* orbitals to higher energy ($10\ Dq$ = 10,170 cm^{-1}), and decreases their splitting to 1560 cm^{-1}. Taken together, the experimental orbital energy levels for TyrH-[L-tyr] (Figure 13, second panel) are consistent with a distorted 6C Fe(II) site.

The saturation data of TyrH-[6MPH$_4$] also shows more nesting than TyrH-[ ] and can be fit equally well to both –ZFS and +ZFS models. Pterin binding results in a larger total splitting of the orbitals of the ground state, regardless of the sign of the ZFS (Figure 13, third panel). However, the XAS data (*vide supra*) indicates that TyrH-[6MPH$_4$] is 6C, which is consistent with a –ZFS. In addition, the orbitals of the ^5E excited state of TyrH-[6MPH$_4$] are shifted to higher energy, supporting an overall stronger 6C LF at the Fe(II) center compared to the resting form.

The VTVH data of TyrH-[L-tyr, 6MPH$_4$] showed remarkable difference in comparison with TyrH-[ ]. The saturation curves are significantly more nested and must be fit with a +ZFS system. The large t_2 orbital splittings and +ZFS for TyrH-[L-tyr, 6MPH$_4$] are consistent with a 5C site that is closer to square pyramidal in geometry and the ground state analysis yields a high degree of rhombic distortion (Table 4) (*80*). As the MCD data indicated, the excited state transitions for TyrH-[L-tyr, 6MPH4] are also in agreement with a 5C site with a strong axial distortion. The similarity of the MCD data of PheH (*74*) to that of TyrH further supports these findings. Only for the ternary complex of PheH (cofactor and substrate analog bound), is there a crystal structure available (PDB ID 1MMT (*83*)), and this structure shows a 5C Fe(II) site that has one short axial bond and rhombically distorted equatorial ligand TyrH.

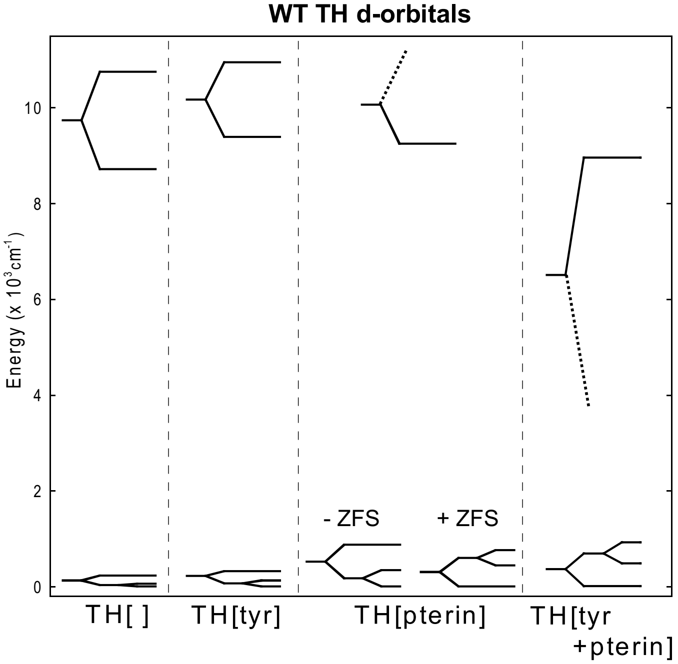

FIGURE 13. Experimental d-orbital energies of TyrH:Fe(II) complexes. The excited state splittings are obtained from band positions in the NIR-MCD spectra and ground state splittings from VTVH MCD. Dotted lines are for uncertainty in the energy positions of the orbitals.

Table 4. Excited State Transition Energies, Spin-Hamiltonian and Ground State Parameters for TyrH:Fe(II) Complexes. All Values in cm^{-1}.

Sample	Band 1	Band 2	10 Dq	Δ^5E	d	g//	D	|E|	Δ	|V|	V/2Δ
TyrH-[ ]	8720	10 750	9735	2030	3.1	9.1	-	-	-200	60	0.15
TyrH-[L-tyr]	9390	10 950	10 170	1560	5.4	9	-	-	-250	130	0.26
TyrH[6MPH$_4$]	9250	~10 900	~10 100	1610	3.7	9.2	-	-	-500	220	0.22
					5.6	8.0	11.4	2.4	600	324	0.27
TyrH[L-tyr, 6MPH$_4$]	8960	-	-	> 4000	5.2	8.0	11.2	2.6	700	420	0.30

MCD Spectroscopy of TyrH Mutants: E332A and S395A. The MCD spectrum of S395A-[ ] (Figure 14A) exhibits two transitions at 8850 cm^{-1} and 10,870 cm^{-1}, similar to wild-type TyrH-[ ], but with two fold higher intensity. The saturation behavior of the LF bands in VTVH MCD shows small nesting (Figure 14B) and fits to a –ZFS system. Together, these indicate that the iron site in S395A-[ ] is distorted 6C. For S395A-[L-tyr, 6MPH$_4$], only one resolvable transition (9330 cm^{-1}) is observed in the MCD spectrum (Figure 14C tan) and the VTVH data (Figure 14D) exhibits a large increase in nesting and yield a +ZFS system, similar to WT TyrH-[L-tyr, 6MPH$_4$], and thus support a 5C square pyramidal active site in S395A-[L-tyr, 6MPH$_4$].

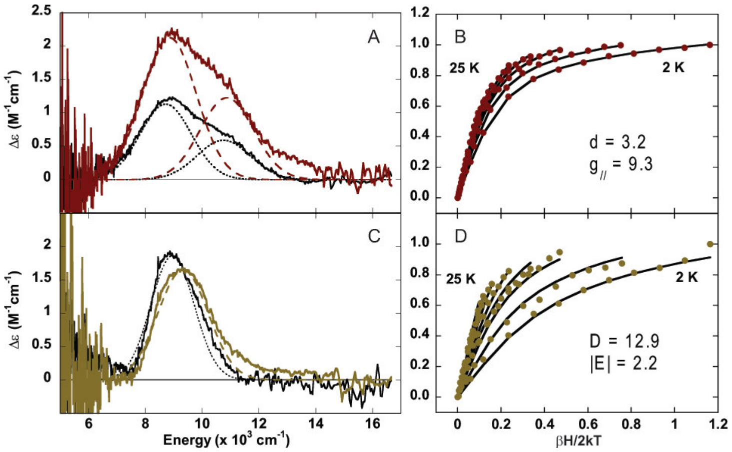

FIGURE 14. MCD spectra at 5K and 7T of S395A mutant. Dashed lines are Gaussian-resolved bandshapes for each spectrum. (A) S395A-[ ] (brown) compared to WT TyrH-[ ] (black), (B) VTVH data (●) and fit (—) of S395A-[ ] collected at 7830 cm^{-1}, (C) S395A-[L-tyr, 6MH$_4$] (tan) compared to WT TyrH-[L-tyr, 6MH$_4$] (black), (D) VTVH data (●) and fit (—) of S395A-[L-tyr, 6MPH$_4$] collected at 8333 cm^{-1}.

The MCD spectrum of E332A-[ ] (Figure 15A, purple) shows two bands at 8880 cm^{-1} and 10 610 cm^{-1}. Compared to WT TyrH-[ ], the higher energy band of E332A-[ ] has more intensity than the lower energy band. The smaller excited state splitting suggests less distortion of this 6C site than WT TyrH-[ ]. The saturation data (Figure 15B) of this mutant show small nesting and are fit to a –ZFS system, confirming that the ferrous site is 6C. The MCD spectrum of E332A-[L-tyr, 6MPH$_4$] exhibits only one band at 9150 cm^{-1} (Figure 15C, light blue). A large amount of nesting is observed in the VTVH data (Figure 15D) and the fitting parameters are in agreement with a +ZFS system. These confirm that the iron site in E332A-[L-tyr, 6MPH$_4$] is 5C distorted square pyramidal.

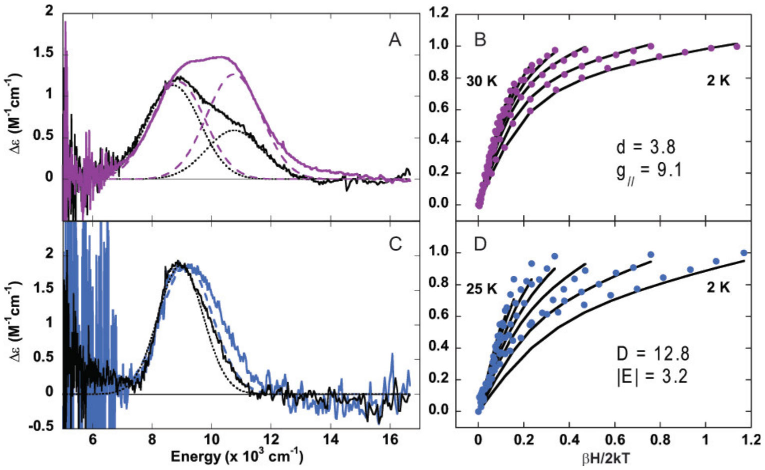

FIGURE 15. MCD spectra at 5K and 7T of E332A mutant. Dashed lines are Gaussian-resolved bandshapes for each spectrum. (A) E332A-[ ] (purple) compared to WT TyrH-[ ] (black), (B) VTVH data (●) and fit (—) of E332A-[ ] collected at 8650 cm^{-1}, (C) E332A-[ ] (light blue) compared to WT TyrH-[L-tyr, $6MH_4$] (black), (D) VTVH data (●) and fit (—) of E332A-[L-tyr, $6MPH_4$] collected at 8306 cm^{-1}.

Stopped-Flow Kinetics of WT TyrH Complexes. In order to gain insight into the initial steps in the reaction of oxygen with TyrH:Fe(II) and tetrahydropterin, stopped-flow single-turnover kinetic experiments were performed for various complexes of WT and E332A TyrH. The oxidation of TyrH:Fe(II) to TyrH:Fe(III) results in a broad increase in the absorbance spectrum between 200 and 450 nm (Figure 16A), due to ligand to Fe(III) charge transfer transitions (*61*). In addition, the reduced and oxidized pterin species involved in the catalytic cycle of TyrH have distinctive absorbance spectra over the same wavelength region (Figure 16B) (*69*). In the stopped-flow experiments, the oxidation of Fe(II) was followed as absorbance increases at 246 and 350 nm (Figure 16A, black to orange) and the oxidation of $6MPH_4$ to quinonoid $6MPH_2$ (q-$6MPH_2$) was detected at 350 – 450 nm (red to green in Figure 16B). The formation of 4a-OH-$6MPH_3$ from $6MPH_4$ can be best followed by absorbance changes at two diagnostic wavelengths:

a maximal initial absorbance increase at 246 nm and an accompanying decrease at 300 – 340 nm (red to blue in Figure 16B). The slow dehydration of 4a-OH-6MPH$_3$ to q-6MPH$_2$ is accompanied by a decrease at 246 nm and an increase at 300 – 450 nm (blue to green in Figure 16B).

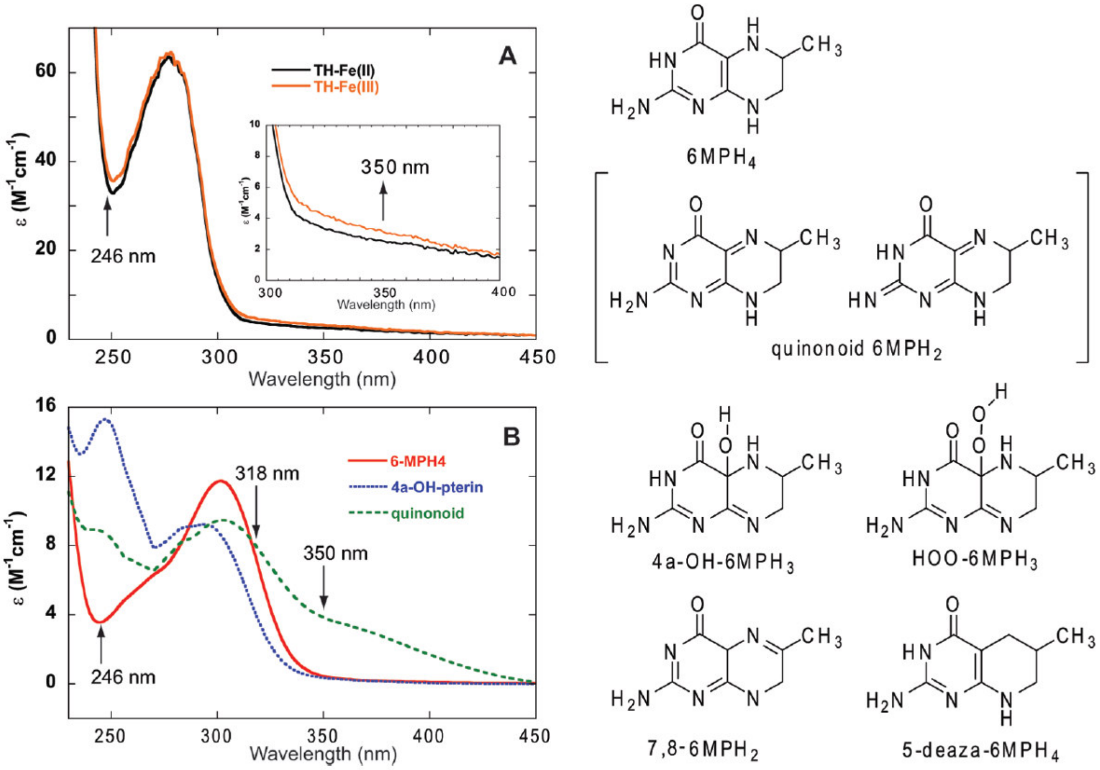

FIGURE 16. Left, absorbance spectra of Fe(II)TyrH (A) and pterin species (B) at neutral pH. Right, structures of pterin species.

Comparison of the stopped-flow absorbance traces from the reactions of the resting form and various binary forms of TyrH (~100 µM final concentration) with varied concentrations of O$_2$ (95 µM to 950 µM) at 5 °C are shown in Figure 17. All the reactions could be successfully simulated using one of the mechanisms in Scheme 8. The rate constants used in the simulations are summarized in Table 5. Addition of O$_2$ to resting

Fe(II)TyrH-[ ] results in monophasic absorbance increases at 246 nm and 350 nm (Figure 17, dashed red trace) and these traces can be well simulated as a single step second-order mechanism with a rate constant of 0.037 $mM^{-1}s^{-1}$ (Scheme 8A and Figure 18), in agreement with previous studies at 20 °C (*61*). Similarly, the oxidation of $6MPH_4$ to q-$6MPH_2$ in the apo-TyrH-[$6MPH_4$] is well-described as a single second-order reaction with a rate constant of 1.7×10^{-4} $mM^{-1}s^{-1}$ (Table 5), comparable to the rate of tetrahydropterin auto-oxidation in solution under the same conditions (1.3×10^{-4} $mM^{-1}s^{-1}$, results not shown), indicating that the presence of apo-TyrH does not affect the rate of tetrahydropterin oxidation.

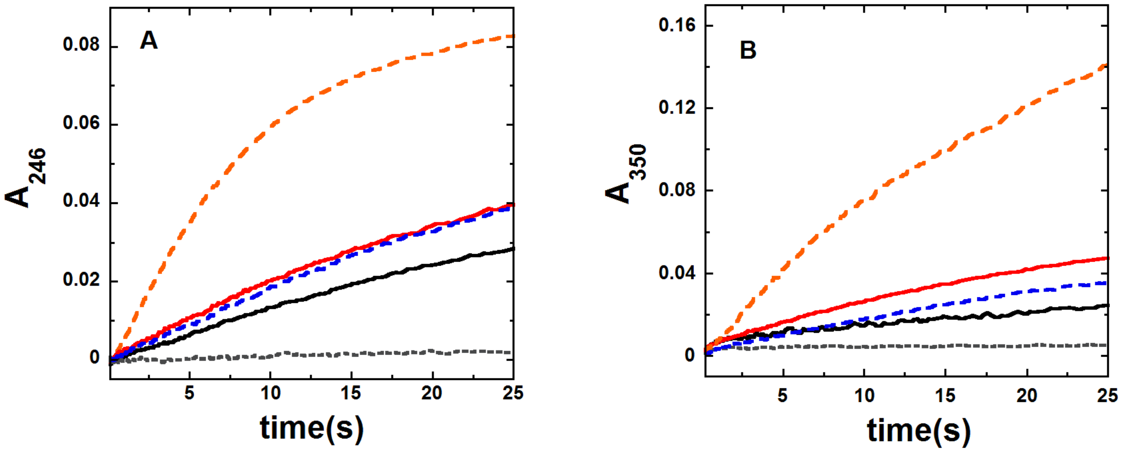

FIGURE 17. Kinetic traces at 246 nm (A) and 350 nm (B) upon mixing a final concentration of 950 μM O_2 with the following TyrH:Fe(II) complexes (90 to 140 μM): TyrH:Fe(II)-[ ] (dashed red line), TyrH:Fe(II)-[$6MPH_4$] (dashed orange line), TyrH:Fe(II)-[5-deaza-$6MPH_4$] (solid grey line), TyrH:Fe(II)-[L-tyr] (solid blue line) and TyrH:Fe(II)-[$6MPH_2$] (dotted black line).

Scheme 8**.** Reactions of various TyrH complexes with O_2

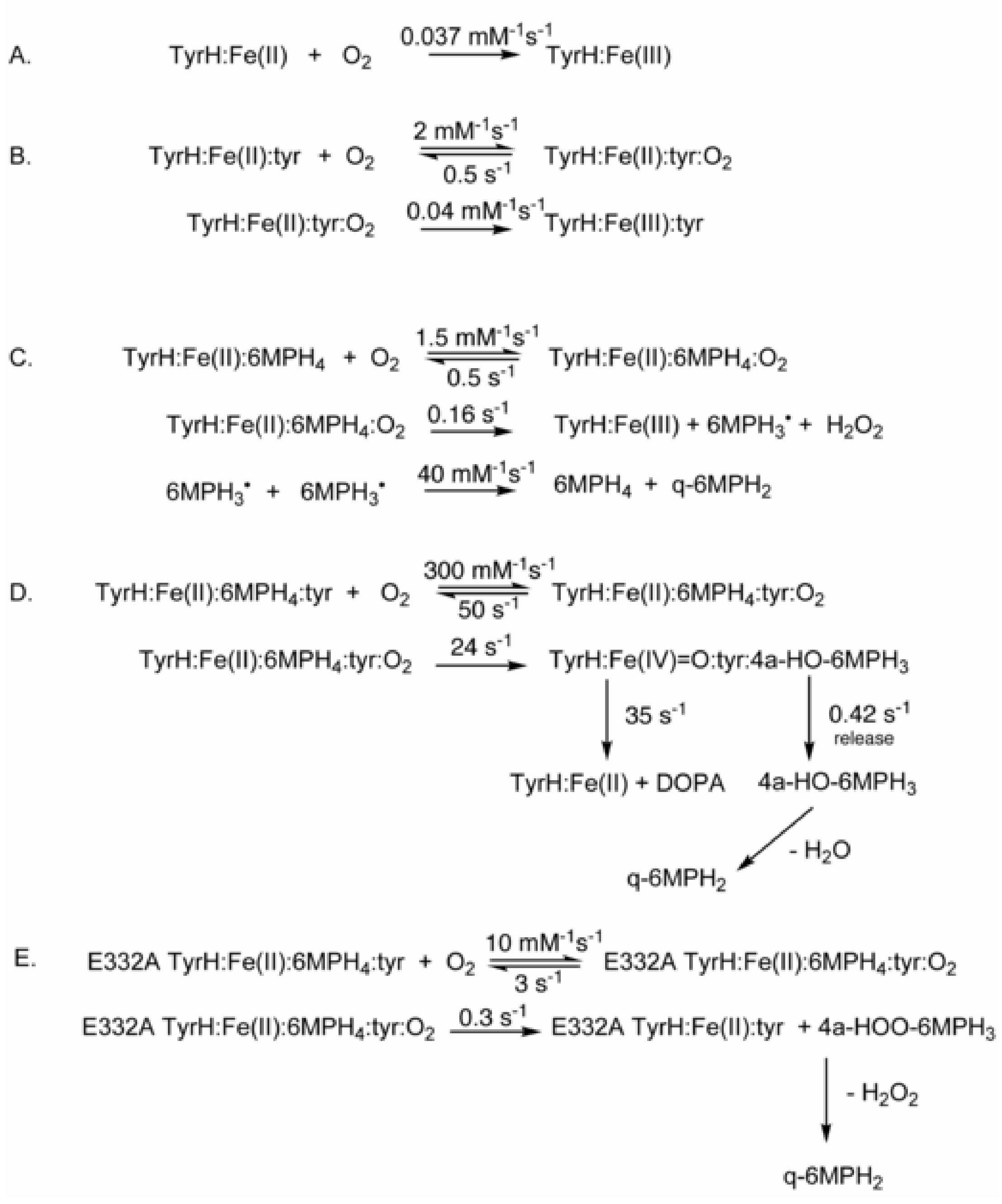

Table 5. Rate Constants for the Reactions of WT and E332A TyrH Complexes with O_2 at 5 °C.

	$Fe^{II}TyrH + O_2 \rightarrow Fe^{III}TyrH$ ($mM^{-1}s^{-1}$)			
$Fe^{II}TyrH$-[ ]	0.037			
	$Fe^{II}TyrH + O_2 \Leftrightarrow Fe^{II}TyrH{:}O_2$ **k_{on} ($mM^{-1}s^{-1}$)**	**k_{off} (s^{-1})**	**$Fe^{II}TyrH{:}O_2 \rightarrow Fe^{III}TyrH$ (s^{-1})**	**$6MPH_4 \rightarrow q\text{-}6MPH_2$ ($mM^{-1}s^{-1}$)**
$Fe^{II}TyrH$-[$6MPH_4$]	1.5	0.5	0.16	40
apoTyrH-[$6MPH_4$]				0.00017
$Fe^{II}TyrH$-[5-deaza-$6MPH_4$]			No reaction	
$Fe^{II}TyrH$-[$6MPH_2$]	2.0	0.5	0.032	
$Fe^{II}TyrH$-[L-tyr]	2.0	0.5	0.040	
$Fe^{II}TyrH$-[5-deaza-$6MPH_4$,L-tyr]	2.0	0.4	0.026	
$Fe^{II}TyrH$-[$6MPH_2$, L-tyr]	6.0	0.5	0.050	
			$Fe^{II}TyrH{:}O_2 \rightarrow Fe^{IV}{=}O$ + 4a-HO-$6MPH_3$	
$Fe^{II}TyrH$-[L-tyr, $6MPH_4$]	300	50	24 s^{-1}	
			$Fe^{II}TyrH{:}O_2 \rightarrow Fe^{II}$ + HOO-$6MPH_3$	
E332A-[L-tyr, 6MPH4]	10	3	0.3 s^{-1}	

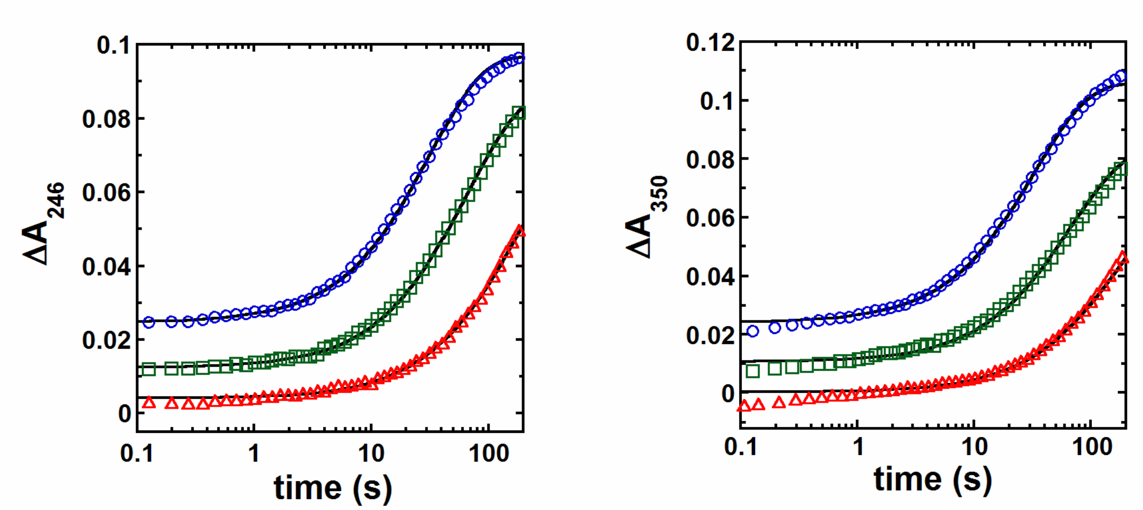

FIGURE 18. Stopped-flow absorbance traces at 246 (left) and 350 nm (right), acquired by mixing an anaerobic solution of ~ 120 µM (final) TyrH:Fe(II)-[ ] in 200 mM Hepes, 10% glycerol and 0.1 M KCl, pH 7.5, with an equal volume of oxygenated buffer at 5 °C. The symbols are the experimental data at final O_2 concentrations of 950 (blue circles), 480 (green squares), or 120 µM (red triangles). The solid lines are simulations according to the mechanism of Scheme 8A, using extinction coefficients from Figure 16.

The absorbance changes accompanying the reaction with oxygen of TyrH complexes containing substrates or analogs are more complex (Figure 17). All are better described by an initial reversible oxygen binding step to form Enz:O_2 complexes followed by chemical transformations (Schemes 8B-D and Figure 19). The presence of only tyrosine or only cofactor analogue 6MPH_2 has little effect on the kinetics of Fe(II) oxidation, and the reactions of both TyrH:Fe(II)-[6MPH_2] and TyrH:Fe(II)-[tyr] can be simulated with similar rate constants for the oxidation step (Figures 17&19, Table 5). The TyrH:Fe(II)-[5-deaza-6MPH_4] complex is an exception; in this case, the rate constants are the same as for TyrH:Fe(II)-[6MPH_2], but the magnitudes of the absorbance changes are much smaller and are consistent with the amount of the free enzyme in these samples (Figure 17, grey dotted and black solid lines, respectively), suggesting that binding of 5-deaza-6MPH_4 to TyrH significantly decreases the reactivity with oxygen.

The kinetic analysis of the reaction of oxygen with TyrH:Fe(II)-[6MPH_4] complex shows that the rate constant for Fe(II) oxidation in this complex is about 5-fold faster than that for the other binary complexes containing the redox-inactive pterins (6MPH_2 or 5-deaza-6MPH_4). This suggests that a change in the oxidation state of the pterin accompanies oxidation of the Fe(II). Scheme 8C, in which the reaction of O_2 with Fe(II)TyH-[6MPH_4] results in concomitant oxidation of Fe(II) to Fe(III) and 6MPH_4 to 6MP$H_3^{\bullet}$ in the first step, followed by disproportionation of 6MP$H_3^{\bullet}$ to give q-6MPH_2 and 6MP$H_4^{\bullet}$, accounts well for the absorbance traces at 246 nm and 350 nm (Figures 17 and 19). The rate constant for 6MPH_4 oxidation in the TyrH:Fe(II)-[6MPH_4] complex shows a three order of magnitude acceleration over the auto-oxidation reaction in apo-TyrH-[6MPH_4] ($0.16\ s^{-1}$ vs $1.7 \times 10^{-4}\ s^{-1}$, respectively). Such rate enhancements observed for

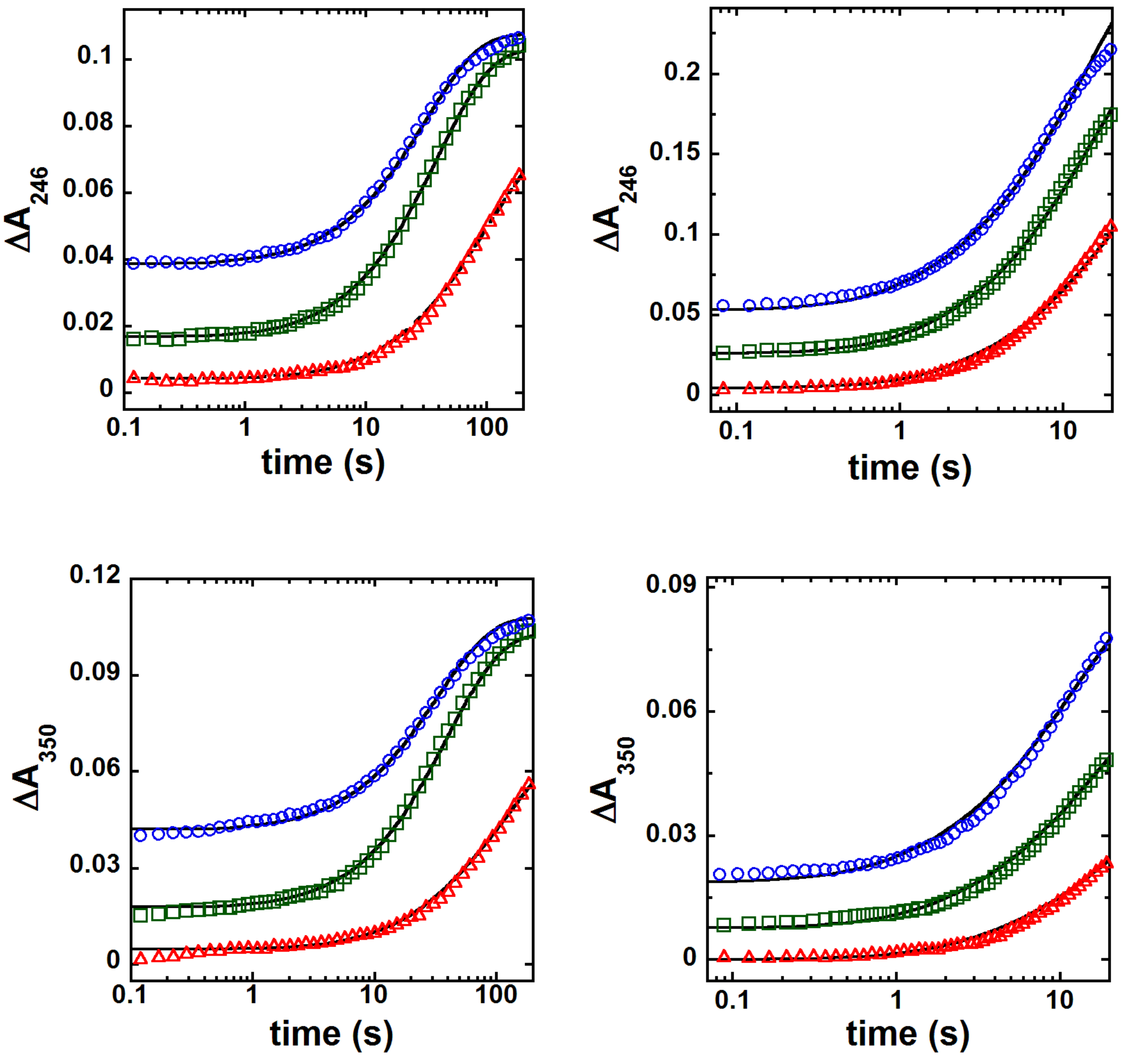

FIGURE 19. Stopped-flow absorbance changes at 246 and 350 nm upon mixing an anaerobic solution of ~ 85 μM (final) WT TyrH:Fe(II)-[L-tyr] (left panels) or ~ 150 μM (final) WT TyrH:Fe(II)-[6MPH$_4$] (right) in 200 mM Hepes, 10% glycerol and 0.1 M KCl, pH 7.5, with an equal volume of oxygenated buffer at 5 ^{o}C. The symbols are the experimental data with final O$_2$ concentrations of 950 (blue circles), 480 (green squares), or 95 μM (red triangles). The solid lines are simulations using mechanisms in Scheme 8 D (left) or E.

both Fe(II) and 6MPH$_4$ in the TyrH:Fe(II)-[6MPH$_4$] are quite reasonable when the redox potentials of the individual species are considered for the mechanism of Scheme 8C. Using an E^0 of + 210 mV for the Fe(II) in TyrH (*84*), the 1-electron oxidation of $Fe^{2+} + O_2 \rightarrow Fe^{3+} + O_2^{-\bullet}$ ($O_2 + e^- \rightarrow O_2^{-\bullet}$, E^0 = -330 mV) (*85*) has ΔE^0 = - 537 mV and is uphill by 12.5 kcal/mol. Similarly, the reaction of 6MPH$_4$ to $6MPH_3^{\bullet}H^+$ (E^o = - 270 mV) (*86*) with O_2 has ΔE^0 = - 600 mV and is energetically uphill by 14 kcal/mol. However, the two electron reaction between Fe(II), O_2 and 6MPH$_4$, ($O_2 + 2e^- \rightarrow H_2O_2$, E^0 = + 280 mV) (*85*) has ΔE^0 = + 83 mV, and is downhill at - 1.9 kcal/mol. Taken together, all these results indicate that the concerted 2-electron transfer to O_2 from 6MPH$_4$ and Fe(II) (equation 2) is more favorable than the individual 1-electron oxidation processes.

$$Fe^{2+} + O_2 + 6MPH_4 \rightarrow Fe^{3+} + H_2O_2 + 6MPH_3^{\bullet} \qquad (2)$$

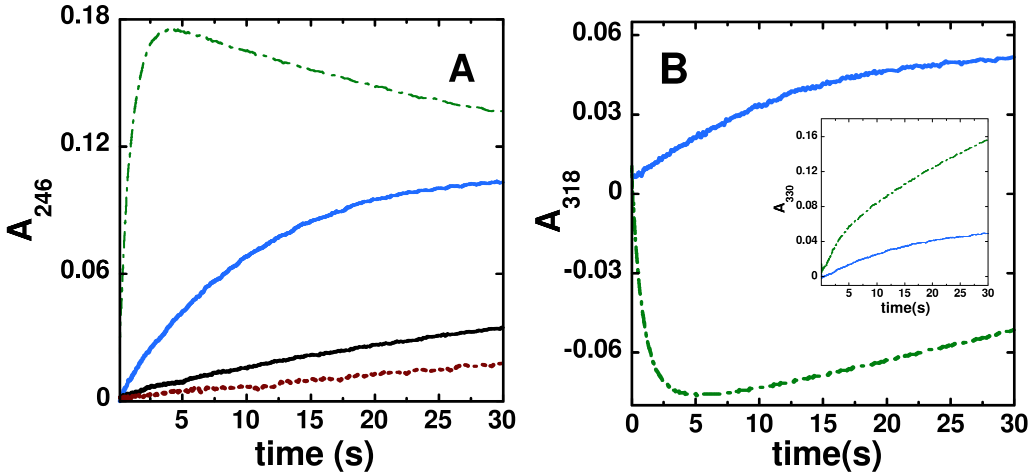

FIGURE 20. Kinetic traces at 246 nm (A) and at 318 nm (B) upon mixing a final concentration of 95 µM O_2 with the following TyrH:Fe(II) complexes: 150 µM WT TyrH:Fe(II)-[L-tyr,6MPH$_4$] (dashed green line), 150 µM E332A TyrH:Fe(II)-[L-tyr,6MPH$_4$] (light blue line), 100 µM WT TyrH:Fe(II)-[L-tyr,5-deaza-6MPH$_4$] (solid grey line) and 120 µM WT TyrH:Fe(II)-[L-tyr,6MPH$_2$] (dotted brown line).

When O_2 is mixed with TyrH:Fe(II)-[L-tyr,6MPH$_4$] to form a catalytically competent complex, a reversible oxygen complex is initially formed with no observable absorbance change (Figure 20, dashed green trace). This is followed by biphasic absorbance changes at 246 nm, 318 nm and 330 nm over approximately 4 s. This rapid initial first phase corresponds to the formation of 4a-HO-6MPH$_3$ with a rate constant of 24 s^{-1} (Scheme 8D and Figure 21). The 4a-HO-6MPH$_3$ is formed in the same step as the Fe(IV)=O intermediate (Scheme 8D). Rapid-quench Mössbauer spectroscopy has shown, as described in the previous chapter, that the Fe(IV)=O intermediate is also formed with a rate constant of 24 s^{-1} under the same conditions used here. No absorbance change associated with the formation of the Fe-OO-pterin could be detected, so we assume that this step occurs after the reversible formation of the initial oxygen adduct, with a rate constant faster than 24 s^{-1}. The slower second phase was successfully modeled as the release of 4a-HO-6MPH$_3$ from the enzyme active site into the solution with a rate constant of 0.42 s^{-1} (Figure 21), a value which matches k_{cat} under these conditions. The 4a-HO-6MPH$_3$ subsequently dehydrates in solution to produce q-6MPH$_2$, resulting in a gradual decrease at 246 nm and increases at 318 nm and 330 nm, with a rate constant of ~0.02 s^{-1}. Although there is no structural data on TyrH:Fe(II)-[L-tyr,5-deaza-6MPH$_4$] and TyrH:Fe(II)-[L-tyr,6MPH$_2$], earlier studies on PheH:Fe(II)-[L-phe,5-deaza-6MPH$_4$] (*31, 74*) and PheH:Fe(II)-[thienylalanine,BH$_4$] (*25, 30*) showed that Fe(II) is 5C in these complexes. This suggests that TyrH:Fe(II)-[L-tyr,5-deaza-6MPH$_4$] and TyrH:Fe(II)-[L-tyr,6MPH$_2$] presumably have similar 5C sites. The reactions of O_2 with TyrH:Fe(II)-[L-tyr,5-deaza-6MPH$_4$] and TyrH:Fe(II)-[L-tyr,6MPH$_2$] are similar to Fe(II) oxidation in TyrH:Fe(II) with either 6MPH$_2$ or tyrosine bound (Figure 20A and Table 5). This indicates that both a 5C Fe(II) and a redox active pterin are needed for the two (and greater) orders of magnitude rate enhancement in the reactivity with O_2 seen with TyrH:Fe(II)-[L-tyr,6MPH$_4$] compared to TyrH:Fe(II)-[ ], TyrH:Fe(II)-[L-tyr], and TyrH:Fe(II)-[6MPH$_4$].

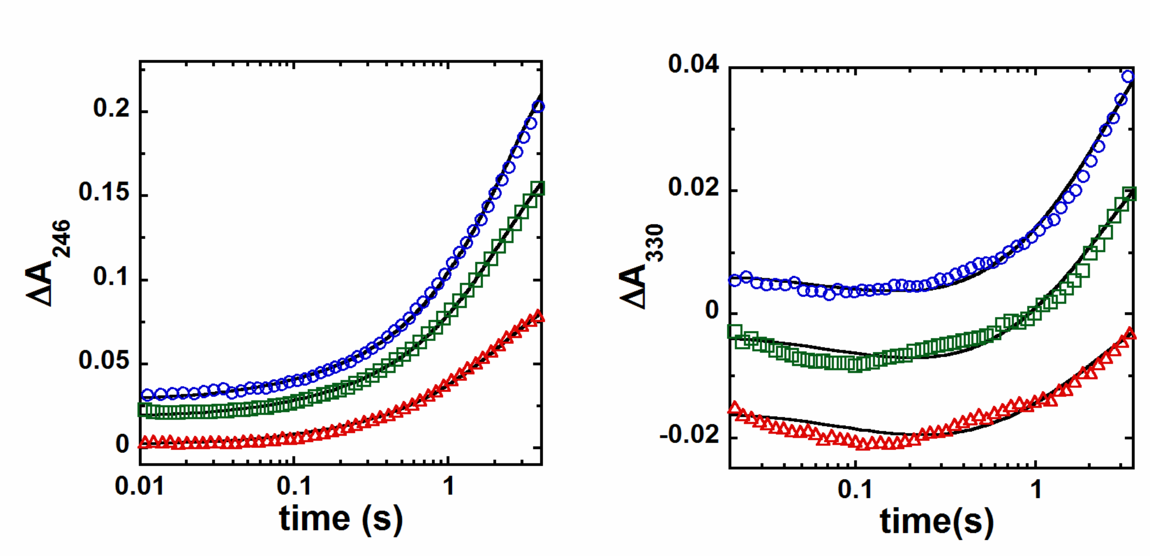

FIGURE 21. Stopped-flow absorbance traces at 246 and 330 nm for WT TyrH (left) upon mixing an anaerobic solution of TyrH:Fe(II)-[L-tyr,6MPH$_4$] (160 μM final for WT) in 200 mM Hepes, 10% glycerol and 0.1 M KCl, pH 7.5, with an equal volume of oxygenated buffer at 5 ^{o}C. The symbols are the experimental data with final O_2 concentrations of 140 (blue circles), 95 (green squares) and 50 μM (red triangles) for WT TyrH. The solid lines are simulations using the mechanism in Scheme 8D. The extinction coefficients were from Figure 16. For unknown extinction coefficients, global analysis was used to obtain initial estimates. The decay of Fe(IV)=O to form the product DOPA was not included in this model, since there is no detectable absorbance change for these species. The slow formation of the q-6MPH$_2$ (~0.02s^{-1}) at later time points was omitted in this analysis.

Stopped-Flow Kinetics of E332A TyrH. The absorbance changes upon addition of O_2 to E332A-TyrH:Fe(II)-[L-tyr,$6MPH_4$] are shown in Figure 20 (solid blue traces). The enzyme clearly catalyzes a reaction between Fe(II), O_2 and tetrahydropterin, but the absorbance changes are distinct from those seen with WT TyrH:Fe(II)-[L-tyr,$6MPH_4$]. In the case of the E332A mutant, the observed absorbance changes can be accounted for by initial reversible oxygen addition followed by formation of an intermediate in a single slow step with a rate constant of 0.3 s^{-1}; this value almost matches k_{cat} for this mutant enzyme (Figure 22). The intermediate decays nonenzymatically with almost the same rate constant (~0.02 s^{-1}) as the dehydration of 4a-HO-$6MPH_3$ to q-$6MPH_2$. The reaction catalyzed by the E332A mutant is clearly slower than that of the wild-type enzyme. The rate constant for the second step is similar to the rate constant for release of the 4a-HO-$6MPH_3$ from the wild-type enzyme. This raises the possibility that the observed rate constant is a net rate constant which includes formation of the intermediate and its release from the enzyme; however, these two rate constants are too similar to resolve. Compared to WT TyrH, the magnitudes of the absorbance changes at 246 nm and 330 nm and the sign of the absorbance change at 318 nm after O_2 binding are different for E332A TyrH (Figure 20, solid blue traces). The spectrum of the intermediate could be obtained by global analysis of the absorbance changes between 240 and 450 nm, fitting the data to a three step kinetic model (Scheme 9 and Figure 23). The starting spectrum and those of the final two species match those for $6MPH_4$, q-$6MPH_2$, and 7,8-$6MPH_2$. The spectrum of the unknown intermediate exhibits a number of differences from that of 4a-HO-$6MPH_3$, including a much lower absorbance at 246 nm and a red-shifted absorbance maximum. These differences establish that, in contrast to WT TyrH, a 4a-HO-$6MPH_3$ is not formed in the reaction of E332A-TyrH:Fe(II)-[L-tyr, $6MPH_4$] with O_2. However, the decay of the intermediate in the E332A TyrH reaction to q-$6MPH_2$ with a rate constant nearly identical to that for 4a-HO-$6MPH_3$ suggests that this intermediate is similar to it. Spectral differences similar to those between this intermediate and that of 4a-HO-$6MPH_3$ have been observed previously for 4a-HO and 4a-HOO-flavins, intermediates in the reaction of the flavoprotein phenol hydroxylases (*87*). Thus, a possible candidate for this intermediate species in the E332A TyrH reaction is a hydroperoxy-pterin, HOO-$6MPH_3$.

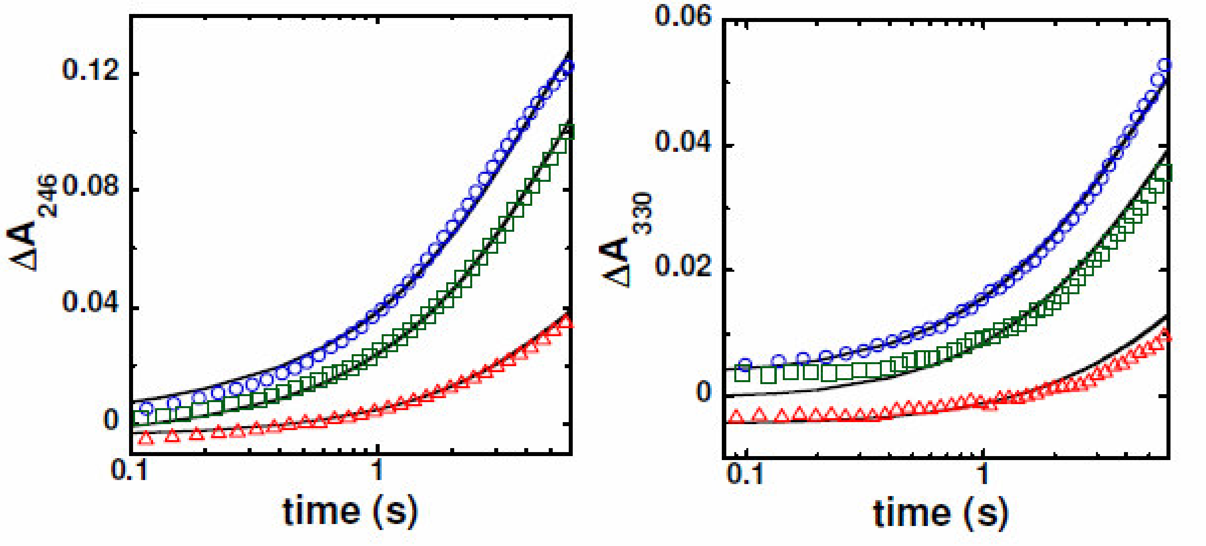

FIGURE 22. Stopped-flow absorbance traces at 246 and 330 nm for E332A TyrH upon mixing an anaerobic solution of TyrH:Fe(II)-[L-tyr,$6MPH_4$] (125 µM final for E332A) in 200 mM Hepes, 10% glycerol and 0.1 M KCl, pH 7.5, with an equal volume of oxygenated buffer at 5 °C. The symbols are the experimental data with final O_2 concentrations of 950 (blue circles), 480 (green squares), or 190 µM (red triangles). The solid lines are simulations using the mechanism in Scheme 8E. The E332A TyrH reaction was modeled similarly to WT TyrH, except that the final two steps were replaced by a single step corresponding to the formation of a hydroperoxy-pterin (HOO-$6MPH_3$).

The rapid single-turnover kinetics experiments presented above allow the dissection of individual steps of TyrH reaction, and show that the presence of a 5C Fe(II) site and a redox-active pterin greatly accelerates the enzyme reaction with O_2. The data on the WT vs E332A reactions also provide insights into the nature of the intermediates formed in the coupled vs uncoupled reaction.

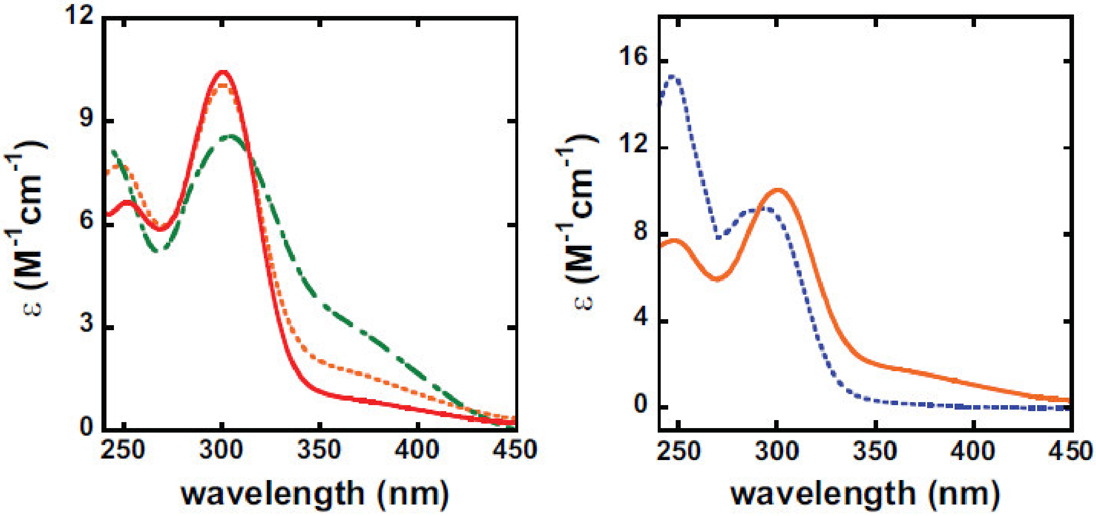

FIGURE 23. Left panel: UV-visible spectra of intermediates in the E332A TyrH reaction (40 μM $6MPH_4$, 10 μM E332A TyrH, 200 μM tyrosine and 250 μM oxygen, in 10 μM ferrous ammonium sulfate, 200 mM Hepes at pH 8.0 and 25 ^{o}C) calculated by globally fitting the absorbance changes (collected at 1 s intervals for a total of 400 s) to the model in Scheme 9 using the program Specfit (Spectrum Software Associates). The spectra that are shown are for $6MPH_4$ (red), A (orange) and B (green). Right panel: Comparison of intermediate A (orange) spectrum with that of 4a-HO-$6MPH_3$ (blue).

Scheme 9

$$\mathbf{6MPH_4} \xrightarrow{k_1} \mathbf{A} \xrightarrow{k_2} \mathbf{B} \xrightarrow{k_3} \mathbf{C}$$

DISCUSSION

In this study, new kinetic and spectroscopic information on various TyrH complexes are presented in order to gain more insight into the reactivity of ferrous active site of TyrH with oxygen and to determine the influence of tyrosine and 6-methyltetrahydropterin ($6MPH_4$) binding on this reactivity. XAS and MCD spectroscopies show that the Fe(II) active site is 6C in resting TyrH. The geometric and electronic structure of the Fe(II) site is slightly perturbed when either tyrosine or pterin is bound to TyrH, but the site remains 6C in both cases. The active site becomes 5C when both tyrosine and pterin are bound, possibly opening up a coordination position for the O_2 reaction. The EXAFS data for TyrH-[L-tyr, $6MPH_4$] are also consistent with a 5C Fe(II) site with 2 His, 1 bidentate Glu and 1 water as ligands, comparable to the crystal structure determined for PheH:Fe(II) with thienylalanine and BH_4 bound (PDB ID 1KWO) (*25*). The 6C to 5C change in the TyrH active site is consistent with the general mechanistic strategy observed in other non-heme iron enzymes that use redox-active cofactors to activate O_2 for reaction with substrates (*80, 88, 89*).

Earlier steady-state kinetic studies on WT TyrH were consistent with an ordered binding sequence of pterin followed by oxygen in rapid equilibrium and then tyrosine before the DOPA product is released (*36*). This suggests that the Fe(II) site in TyrH undergoes a structural change upon pterin binding that allows the Fe(II), pterin and O_2 to react before tyrosine binds. The protein itself does undergo conformational changes upon pterin binding (*34*). However, our spectroscopic data show only a slight perturbation to the 6C Fe(II) site upon pterin binding.

For the resting form of the enzyme, TyrH:Fe(II)-[ ], the single turnover kinetic results indicate that the isolated one-electron oxidation reactions of Fe(II) to Fe(III) is slow due to unfavorable thermodynamics. The oxidation of Fe(II) in binary complexes of TyrH, either with only tyrosine bound or with a cofactor analogue (a non-redox active pterin) bound, also exhibits slow kinetics. Even in the case of non-catalytic ternary complexes (bound with both tyrosine and a non-redox active pterin), which are expected to have 5C Fe(II) active site, there is not any rate acceleration, with the oxidation rate of Fe(II) being very similar to that of the resting enzyme. Oxidation kinetics of tetrahydropterin to quinonoid dihydropterin (q-$6MPH_2$) in apoTyrH-[$6MPH_4$] is no different than the autoxidation reaction of tetrahydropterin in solution. However, the combination of Fe(II) and redox-active pterin in TyrH: Fe(II)-[$6MPH_4$] accelerates both the Fe(II) oxidation and uncoupled pterin oxidation reactions, even though the Fe(II) site remains 6C, as indicated by the spectroscopic investigation. The faster reaction rates in TyrH: Fe(II)-[$6MPH_4$] can be ascribed to the favorable thermodynamics of the two-electron reduction of O_2 to peroxide by the combined reaction of $Fe^{II} \rightarrow Fe^{III}$ and $6MPH_4 \rightarrow 6MPH_3^{\bullet}$.

The catalytically relevant complex of TyrH, TyrH: Fe(II)-[L-tyr, $6MPH_4$], as the MCD and XAS data clearly showed, has a 5C TyrH: Fe(II) site. In the reaction of TyrH: Fe(II) -[L-tyr, $6MPH_4$] complex with oxygen, the first observable step, corresponding to the breakdown of the putative Fe(II)-OO-pterin intermediate, is 2 – 3 orders of magnitude faster than the Fe(II), $6MPH_4$ and Fe(II) + $6MPH_4$ oxidation reactions involving the 6C and non-catalytic 5C forms of TyrH (Table 5). The measured rate constant for this step necessarily sets a lower limit for the rate constant for the initial reaction with oxygen to form this intermediate. Thus, the two electron transfer from the 5C Fe(II) and reduced pterin to O_2 is far more favorable than in the 6C TyrH: Fe(II)-[$6MPH_4$] site and than in the 5C TyrH: Fe(II)-[L-tyr,5-deaza-$6MPH_4$] and TyrH: Fe(II)-[L-tyr,$6MPH_2$] sites, confirming that the open coordination position on the Fe(II) and the presence of a redox active pterin are both critical for catalytic TyrH reactivity. The requirement for the presence of both cofactor and substrate for a catalytically relevant oxygen reactivity of the active site iron has been demonstrated in other groups of mononuclear non-heme enzymes. In the case of α-KG dependent TauD, binding of the substrate taurine has been shown to activate Fe(II) active site for O_2 reactivity by 3 orders of magnitude (*10*). Although there is no direct structural evidence for a coordination change of the active site of TauD, MCD studies on another α-KG dependent enzyme, clavaminate synthase, showed that iron center becomes 5-coordinate when both cofactor and substrate are bound (*90*). Thus, sluggish reactivity of protein active sites with oxygen in the absence of substrate has been considered as a control mechanism of these enzymes with two significant benefits; preventing consumption of cofactors in the absence of the target substrates and protecting enzymes from self-inactivation by avoiding formation of reactive radical species (*10*).

Earlier observations under steady-state conditions with E332A TyrH suggested that 4a-hydroxypterin is not formed in the uncoupled reaction of E332A TyrH (*29*). Stopped-flow kinetic studies were performed in order to compare the individual reaction steps of the uncoupled E332A reaction with those of the coupled WT reaction. The first step with observable kinetics of WT TyrH is the decay of the putative Fe(II)-OO-pterin intermediate to form 4a-HO-pterin, which occurs at a rate of 24 s^{-1}. The 4a-HO-pterin that forms in WT TyrH and in the S395A mutant (*37*) is not observed in the E332A mutant, which also does not hydroxylate tyrosine, indicating that the Fe(IV)=O intermediate also does not form. The first observable step of the E332A TyrH reaction is the formation of an oxidized pterin species, possibly the HOO-pterin, with a rate constant of 0.3 s^{-1}. This intermediate may form either by direct reaction of O_2 with $6MPH_4$ (however this reaction is much slower at 1.7×10^{-4} $mM^{-1}s^{-1}$), or, more likely, through a Fe(II)-OO-pterin intermediate as in WT TyrH. In the latter case, the E332A mutation may change the reactivity of the Fe(II)-OO-pterin intermediate such that it decomposes with a slower rate and through a different mechanism than WT. In both, decay of the intermediate likely involves protonation of the Fe(II)-OO-pterin. In WT TyrH, the nature of the cleavage products, Fe(II)=O and 4a-OH-pterin indicate that the O distal (O_{dis}) to the Fe(II) is protonated to heterolytically cleave (Scheme 10, top). In the E332A mutant, an oxidized pterin species, possibly the HOO-pterin, is formed. This would involve the protonation of the O proximal to Fe (O_{prox}) in the Fe(II)-OO-pterin, followed by the cleavage of the Fe-O_{prox} bond (Scheme 10, bottom). These results suggest that the E332 residue participates in the reactivity of TyrH by directing the distal protonation of the Fe(II)-OO-pterin intermediate.

Scheme 10. Proposed protonation sites in WT and E332A TyrH

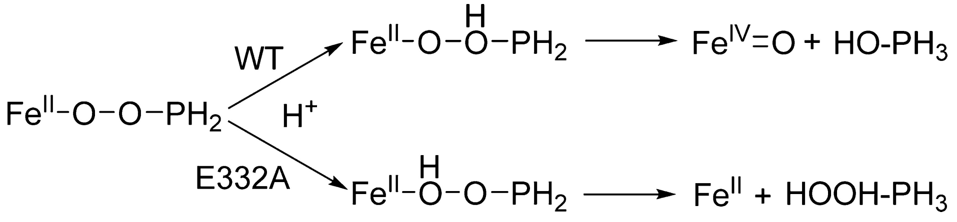

The crystal structure of Fe(II)-PheH with thienylalanine and tetrahydrobiopterin bound (PDB 1KWO, Figure 24) indicates that the E332 carboxylate group is oriented towards the pterin, and could hydrogen bond to it, either through direct interaction with the proton on the N3, or through solvent molecules (*25*). The E332 residue could either directly transfer the proton from N3 to O_{dis} (N3 is deprotonated in the final quinonoid pterin product) or direct a solvent water via an H-bond to the O_{dis}. The water ligand is not likely to be the proton source for heterolytic O-O cleavage, because the MCD data of the TyrH-[L-tyr, $6MPH_4$] complexes in WT and E332A indicate that the geometric and electronic structures of the 5C sites are very similar. Apparently, when E332 is mutated to an alanine, the enzyme can no longer direct a proton to O_{dis}, and the O_{prox} is protonated instead, leading to the cleavage of the Fe-O bond to regenerate Fe(II) and HOO-pterin.

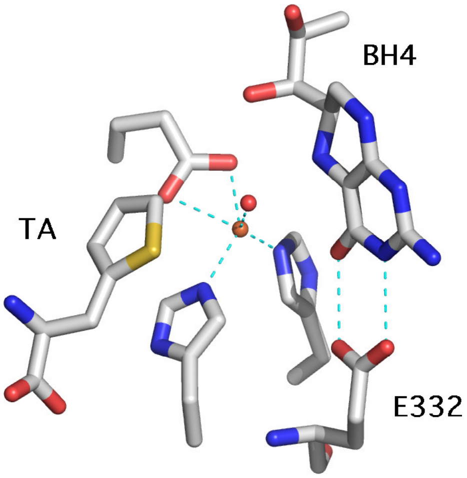

FIGURE 24. Crystal structure of the Fe(II) active site of PheH showing the binding positions of the amino acid substrate (TA, thienylalanine, cofactor (BH_4, tetrahydrobiopterin), metal ligands and the E332 residue (using the TyrH numbering). The figure was created from the PDB file 1KW0.

In summary, this study shows through XAS and MCD spectroscopy that the Fe(II) active site in TyrH is 6C until both tyrosine and pterin are bound. This 6C → 5C conversion is consistent with the general mechanistic strategy observed in other mononuclear non-heme iron enzymes. Single turnover kinetic data on WT TyrH indicate that at a 6C active site, the two electron reduction of O_2 to peroxide by Fe(II) and pterin is favored over individual one electron reactions. However, this reaction is still slow. Importantly, this reaction is greatly accelerated in the TyrH: Fe(II)-[L-tyr, $6MPH_4$] complex, indicating that both 5C Fe(II) and pterin are required for the O_2 reaction. Comparison of the kinetics of WT and E332A TyrH: Fe(II)-[L-tyr, $6MPH_4$] reactions with O_2 indicate that the E332 residue plays a role in directing the protonation of the bridged Fe(II)-OO-pterin complex to produce the Fe(IV)=O hydroxylating intermediate and hence is important for tuning the TyrH active site for productive coupled turnover.

CHAPTER IV

INVESTIGATIONS OF THE CHEMICAL AND PHYSICAL STEPS IN THE CATALYTIC MECHANISM OF TYROSINE HYDROXYLASE: RAPID REACTION AND VISCOSITY STUDIES

INTRODUCTION

Tyrosine hydroxylase (TyrH) is a member of the pterin dependent aromatic amino acid hydroxylase family, which utilize a mononuclear non-heme iron and a reduced pterin cofactor to activate molecular oxygen for the hydroxylation of their corresponding amino acid substrates. TyrH, which is found in the brain and adrenal gland, catalyzes conversion of L-tyrosine to L-dihydroxyphenylalanine (DOPA) (Scheme 1). This is the first and rate-limiting step in the biosynthesis of catecholamine neurotransmitters dopamine, noradrenaline and adrenaline (*15, 21*). A deficiency of TyrH is related to several neurological disorders including DOPA-responsive Parkinson's disease, progressive encephalopathy, DOPA-non-responsive dystonia and DOPA-responsive dystonia (Segawa's disease) (*17, 18*). The other members of the family are also of physiological significance; phenylalanine hydroxylase, a liver enzyme, catalyzes the conversion of phenylalanine in the diet to tyrosine, and tyrptophan hydroxylase, a brain enzyme, converts tryptophan to 5-hydroxytryptophan as a precursor to the neurotransmitter serotonin (*15, 21*).

All members of the aromatic amino acid hydroxylase family have similar active sites, where the mononuclear non-heme iron is coordinated by the common motif of 2-His-1-Glu facial triad (*12, 23*). Studies of the three enzymes show that they share a common catalytic mechanism (*38-41*). The proposed mechanism for TyrH is shown in Scheme 2 (*21*). The earlier steps in this mechanism include a reaction between iron, tetrahydropterin and molecular oxygen to give an iron μ-peroxypterin. Heterolytic cleavage of this intermediate leads to the formation of the hydroxylating intermediate, a high valence Fe(IV)O species, and the side product 4a-hydroxypterin. In the later stage, reaction of the Fe(IV)O with the aromatic ring gives the hydroxylated amino acid product through electrophilic aromatic substitution (*44*). Studies in Chapter II provided direct evidence from Mössbauer spectroscopy for the postulated Fe(IV) intermediate in the reaction pathway of TyrH. Complementary single turnover rapid chemical quench experiments and stopped-flow absorption spectroscopy further showed that Fe(IV) and 4a-hydroxypterin intermediates are kinetically competent to be on the reaction pathway of the proposed mechanism(Scheme 2). These experiments also revealed that the rate constant for the formation of DOPA is much faster than the steady-state k_{cat} value (*36*). In this study, we employed a combination of rapid reaction and steady-state kinetics to elucidate the nature of the rate-limiting step or steps in the mechanism of WT TyrH.

EXPERIMENTAL PROCEDURES

Chemicals. 6-Methyltetrahydropterin was from Schircks Laboratories (Jona, Switzerland). Hepes, ferrous ammonium sulfate, sucrose and trehalose were purchased from Fisher (Pittsburgh, PA). Glycerol and tyrosine were from Sigma-Aldrich (Milwaukee, WI). The GEMINI reverse-phase C 18 HPLC column was obtained from Phenomenex (Torrance, CA). All other reagents were of the highest purity commercially available.

Expression and Purification of TyrH. TyrH was expressed in E. coli and purified as previously described (*61*). After purification, the enzyme was dissolved in 200 mM Hepes (pH 7.5), 10% glycerol and 0.1 M KCl containing 5 mM EDTA and incubated for one hour on ice before dialyzing against the same buffer without EDTA. The iron content was determined using a Perkin-Elmer Analyst 700 atomic absorption spectrophotometer. For experiments where viscogen was used, the enzyme was dialyzed into the buffer that contains no glycerol (200 mM Hepes, pH 7.5, 0.1 M KCl).

Steady-State Assays. Steady-state kinetic parameters of WT TyrH were obtained using a colorimetric end point assay to measure DOPA production, as previously described (*36*). Conditions were 0.1-0.5 μM TyrH, 100 μg/ml catalase, 1 mM DTT, 10 μM ferrous ammonium sulfate and either 1 mM $6MPH_4$ when tyrosine was the varied substrate (3-300 μM) or 200 μM tyrosine when $6MPH_4$ was the varied substrate (5 μM-1 mM). The buffer was 200 mM Hepes (pH 7.5), 0.1 M KCl with or without viscogen. The viscosity of the buffer was varied by adding glycerol, sucrose or trehalose. The absolute viscosities for buffers (η) at 5 °C and 30 °C were calculated using values reported in literature (*91-93*). The small effect of buffer and salt on the viscosity of the solutions was neglected.

Rapid Chemical Quench. Rapid chemical quench experiments of TyrH were performed using an SFM-400/Q rapid-mixing instrument from Bio-Logic (Claix, France) in quenched-flow mode. The instrument was made anaerobic through incubation with excess sodium dithionite solution for at least two hours. Water bath solution was made anaerobic through bubbling with nitrogen gas to prevent any possible diffusion of O_2 to the system. Apo-TyrH (30-40 μM) in 200 mM Hepes (pH 7.5), 10% glycerol and 0.1 M

KCl (total volume of ~10 ml) was made anaerobic in a tonometer through at least 20 argon-vacuum cycles. Ferrous ammonium sulfate (~20 μl, ~0.9 equivalent of enzyme) was then added to the tonometer under argon. The $6MPH_4$ stock solution (~40mM) was prepared in 2 mM HCl and an extinction coefficient of 17.8 $mM^{-1}cm^{-1}$ in 2 M perchloric acid was used to determine the exact concentration. A volume corresponding to a final concentration of 2 mM (in the tonometer) $6MPH_4$ was placed in the side arm of the tonometer under argon. Additional argon-vacuum cycles were performed prior to mixing the $6MPH_4$ solution with the tonometer contents, which was then loaded into one of the syringes of the rapid-mixing instrument. A second syringe was loaded with buffer containing 500 μM tyrosine that had been bubbled with pure oxygen gas for at least 20 min. This was done either on ice to obtain a concentration of 1.9 mM oxygen or at room temperature to get a concentration of 1.2 mM. The quenching solution, 5 M HCl, was loaded into a third syringe. The tonometer contents were mixed with the tyrosine-containing oxygenated buffer and quenched with acid after being aged through a 90 μl (N° 3) delay line. Tyrosine and DOPA present in the collected samples were separated on a C18 Phenomenex HPLC column (250-4.6 mm) with an isocratic mobile phase of 15 mM sodium phosphate, pH 7.0, at a flow rate of 1 ml/min. The amount of DOPA was quantified using a Waters 2475 Multi λ fluorescence detector with an excitation wavelength of 270 nm and an emission wavelength of 310 nm.

Stopped-Flow Spectrophotometry. Single turnover kinetics of TyrH, at conditions of varied viscosities, were monitored using an Applied Photophysics (Leatherhead, UK) SX20 stopped-flow spectrophotometer in absorbance mode. The instrument was made anaerobic in the same way as described above for the rapid chemical quench experiment.

A solution of apo-TyrH (430 μM) and tyrosine (750 μM) in 200 mM Hepes (pH 7.5), 0.1 M KCl (with or without sucrose, 22%, w/w) was made anaerobic in a tonometer through at least 20 argon-vacuum cycles. A stoichiometric amount of ferrous ammonium sulfate (~20 μl, ~0.9 equivalent of enzyme) was then added to the tonometer under argon. $6MPH_4$ solution, corresponding to a final concentration of 1.3 mM (in the tonometer), was placed in the side arm of the tonometer under argon. Additional argon-vacuum cycles were performed before mixing the $6MPH_4$ solution with the tonometer contents. The tonometer was then loaded into one of the syringes of the stopped-flow instrument. The second syringe was loaded with the same buffer as in tonometer, having oxygen concentrations corresponding to the O_2 solubility at 5 °C (400 μM for buffer without viscogen, 270 μM for buffer with 22% sucrose) (*94*). The mixing of the contents of the two stopped-flow syringes was initiated through the instrument software and wavelengths of 246 nm and 318 nm were monitored. In cases where the viscosity of the reaction medium was varied, each side of the stopped-flow instrument contained exactly the same concentration of viscogen to prevent mixing artifacts.

Data Analysis. Kinetics of DOPA formation obtained through rapid chemical quench experiments were analyzed using the global analysis program KinTek Explorer Pro (KinTek Corp., Austin, TX). The active enzyme concentration was varied within 5 % of the experimental values to account for pipetting errors or inactivation of the enzyme during the experiment. The agreement of the data points with simulation traces were visually inspected in the live display option of KinTek by varying the rate constants. Thus it was possible to observe the change in the quality of the simulations within the varied limits of the enzyme concentration upon a range of rate constants.

Analyses of the effects of viscosity on the steady-state kinetics were performed by a global analysis method. All the initial rate data sets obtained with or without viscogen at a given temperature were fit simultaneously to equation 3 using the analysis program Igor Pro (Wavemetrics, Lake Oswego, OR). Equation 3 is a modified Michaelis-Menten equation that describes separate viscosity effects on k_{cat} and $k_{\mathrm{cat}}/K_{\mathrm{m}}$ values. In this equation, S is the concentration of the varied substrate, μ is relative viscosity ($\eta/\eta°$) minus 1 and m and n are the viscosity effects on $k_{\mathrm{cat}}/K_{\mathrm{m}}$ and on k_{cat}, respectively. Due to severe substrate inhibition at high concentrations of tyrosine at 5 °C, initial rate data obtained at low tyrosine concentrations were fit globally to eq 4 instead of eq 3 to calculate the viscosity effects on $k_{\mathrm{cat}}/K_{\mathrm{m}}$ for tyrosine.

$$v = \frac{k_{\mathrm{cat}}\,\mathrm{S}}{K_{\mathrm{m}}\,[1 + m(\mu)] + \mathrm{S}[1 + n(\mu)]} \tag{3}$$

$$v = \frac{k_{\mathrm{cat}}\,\mathrm{S}}{K_{\mathrm{m}}\,[1+m(\mu)]} \tag{4}$$

Calculation of association rate constants (k_1) and forward commitments (k_2/k_{-1}) was performed by a fit to eq 5 of the $k_{\mathrm{cat}}/K_{\mathrm{m}}$ values for tyrosine at various relative viscosities from multiple experiments using the program Igor Pro.

$$k_{\mathrm{cat}} / K_{\mathrm{m}} = \frac{k_1(\eta^o/\eta)}{1 + [(k_{-1}/k_2)(\eta^o/\eta)]} \tag{5}$$

To analyze the stopped-flow kinetic data, the absorbance traces were first fit simultaneously to various sequential mechanisms using the program SpecFit (Spectrum Software Associates). The results from this analysis gave an estimate for the number of observable phases and for the corresponding rate constants for further analysis. The data were then analyzed globally using the program KinTek Explorer Pro (KinTek Corp., Austin, TX). Estimates for the rate constants and extinction coefficients were taken from studies presented in Chapters II and III and from the SpecFit analysis. The global analysis by KinTek was first performed in an iterative fashion by fitting one or two parameters at a time and by keeping other parameters constant. This way the estimates for unknown parameters were determined. The best-fit parameters obtained in this fashion were then employed for a global simulation of the absorbance traces.

RESULTS

Rapid Chemical Quench Experiments. Single turnover experiments presented in Chapter II showed that the rate constant for the formation of the product DOPA in the first turnover of TyrH reaction is much faster than the k_{cat} value observed in steady-state experiments (~15 s^{-1} vs. ~ 0.4 s^{-1} at 5 °C). This suggests that k_{cat} is limited by subsequent slow steps. Since this should result in a pre-steady-state burst of DOPA formation in the first turnover (*95*), the reaction of TyrH was analyzed by rapid chemical quench. The anaerobic complex of ferrous TyrH(30-40 μM):6MPH$_4$(2.0 mM) was mixed with an equal volume of buffer containing tyrosine (500 μM) and O$_2$ (1.9 mM at 5 °C and 1.2 mM at 30 °C). Tyrosine and 6MPH$_4$ concentrations were chosen to be high enough to assure complete and rapid binding (K_m values are ~30 μM and ~70 μM at 5 °C for tyrosine and 6MPH$_4$, respectively). The reaction was quenched with 5 M HCl at various time points from 10 ms to several seconds and the samples collected were analyzed by HPLC to quantify the amount of the product DOPA. The time courses of product formation obtained from these analyses are shown in Figure 25. An initial burst can be clearly seen at both temperatures. For quantitative analysis, the data were simulated according to the mechanism in Scheme 11. In the first step of this mechanism, binding of tyrosine, $6MPH_4$ and O_2 is rapid *(vide supra)*, thus k_{burst} is determined by the much slower chemical rate for DOPA formation. Using the live simulation display option of the program KinTek, the agreement of the data points with the simulation traces were visually inspected. The data at 5 °C could be well simulated with rate constants in the range of 7-14 s^{-1} for the burst phase and 0.6-0.7 s^{-1} for the linear phase when the active enzyme concentration is varied in a range of 0.95-1.05 equivalent of the experimental concentration. This rate constant for the burst phase is close to the earlier value for DOPA formation from single turnover experiments at this temperature, 14 s^{-1} *(vide supra)*. With the same approach, the kinetic data at 30 °C could be simulated well with rate constants in the range of 14-22 s^{-1} and 3-4 s^{-1} for the burst and the linear phases, respectively. Figure 25 shows the simulations obtained with k_{burst} of 12 s^{-1} and k_{linear} of 0.7 s^{-1} for the data at 5 °C and k_{burst} of 20 s^{-1} and k_{linear} of 3.5 s^{-1} for the data at 30 °C.

Scheme 11

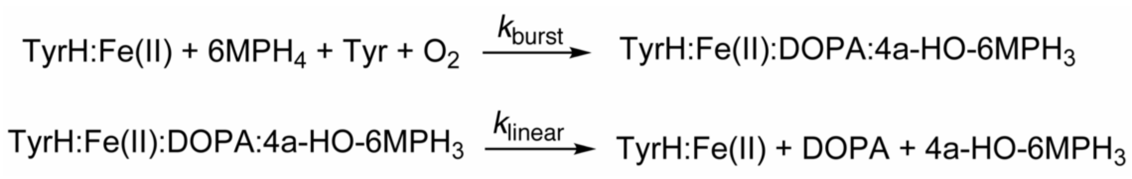

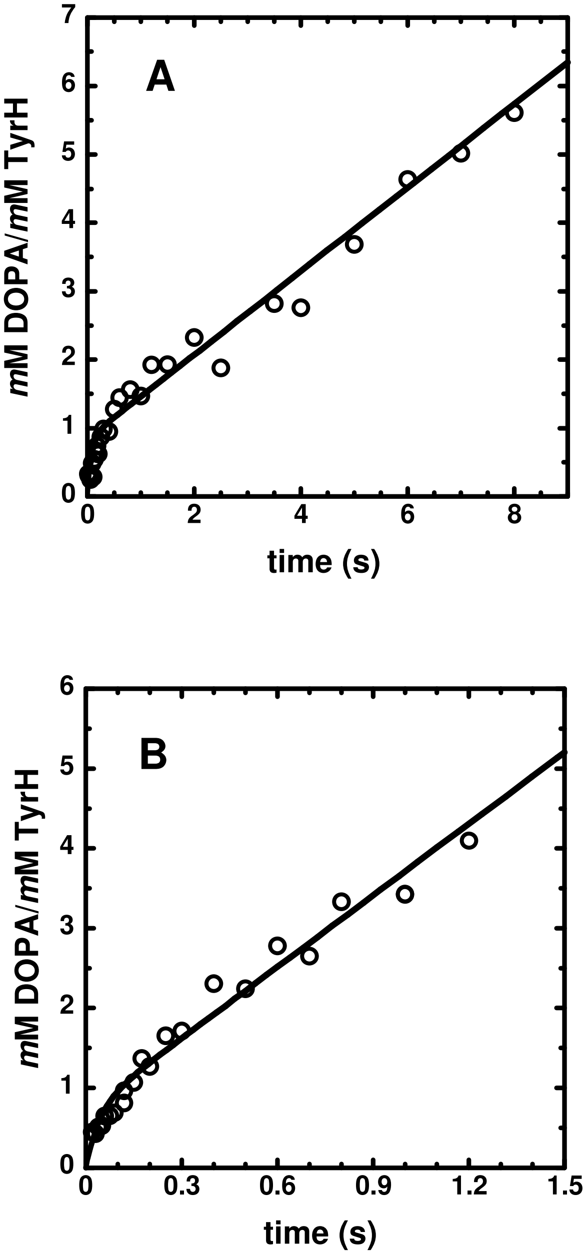

FIGURE 25. Time course (A) at 5 °C or (B) at 30 °C for the formation of the product DOPA from the reaction of TyrH (30-40 uM):6MPH$_4$ (2 mM) with an equal volume of Tyr (500 uM):O$_2$ (1.9 mM at 5 °C and 1.2 mM at 30 °C). Circles are the data obtained from rapid chemical quench analyses for DOPA. The lines are from the simulations to the mechanism in Scheme 11 with rate constants given in the text.

Steady-State Viscosity Experiments. The rapid chemical quench experiments established that the chemical steps in the TyrH reaction that result in DOPA formation are significantly faster than the following steps. In many enzymatic systems, such subsequent steps are either product release steps or conformational changes associated with product release (*96-103*). Product release should be diffusion limited, so that the rates are dependent on the viscosity of the medium (*96*). To investigate if product release is a rate-limiting step in the TyrH reaction, k_{cat} was measured in the presence of various viscogens. Three different viscogens were employed: glycerol, sucrose and trehalose. Experiments with glycerol showed inhibition at high concentrations. This might be due to the binding of relatively small glycerol molecules in the active site of the enzyme. In fact, PheH has been reported to be inhibited by glycerol due to the perturbation of the iron (*104*). Therefore, the analysis was carried out with sucrose and trehalose as viscogens. Viscosity effect is a measure of the rate decrease for a reaction upon increasing solvent viscosity and can take values between 0 and 1. A viscosity effect of 0 means the rate of the reaction is completely independent of solvent viscosity, whereas an effect of 1, which is the theoretical limit, indicates a completely diffusion-limited event. The steady-state rate data were analyzed by a global fit according to eq 3 or 4, a modified Michaelis-Menten equation where viscosity effects are included as coefficient values and the relative viscosity is an independent variable. In this approach, all the initial rate data obtained at different viscogen concentrations are fit to a single set of rate parameters (k_{cat} and k_{cat}/K_m). Results from the global analysis are given in Table 6.

Table 6. Viscosity Effects on Kinetic Parameters for TyrH Reaction[a] from Global Analysis.

Viscogen	Temp (°C)	$(k_{\mathrm{cat}})^{\eta}$ [b]	$(k_{\mathrm{cat}}/K_{\mathrm{tyr}})^{\eta}$ [c]	$(k_{\mathrm{cat}}/K_{\mathrm{6MPH4}})^{\eta}$ [b]
Sucrose	5	0.89 ± 0.09	0.49 ± 0.09	1.41 ± 0.26
Sucrose	30	0.83 ± 0.03	0.30 ± 0.11	1.93 ± 0.27
Trehalose	5	0.78 ± 0.07	0.38 ± 0.10	0.27 ± 0.10
Trehalose	30	0.94 ± 0.10	0.54 ± 0.15	1.26 ± 0.29

[a] Conditions: 0.1-0.5 μM TyrH, 100 μg/ml catalase, 1 mM DTT, 10 μM ferrous ammonium sulfate, 200 mM Hepes (pH 7.5) and 0.1 M KCl. Appropriate amounts sucrose or trehalose was included in the reaction medium to obtain desired solvent viscosities. Global analysis was performed as described in experimental procedures. [b] 200 μM tyrosine with varied concentrations of $6MPH_4$ (5 μM-1 mM). [c] 1 mM $6MPH_4$ with varied concentrations of tyrosine (3-300 μM).

Both sucrose and trehalose had almost the same effect on k_{cat} at 5 °C and 30 °C. A viscosity effect of about 0.8-0.9 was determined (Table 6 and Figure 26). This indicates that k_{cat} of TyrH reaction is significantly limited by a diffusional event.

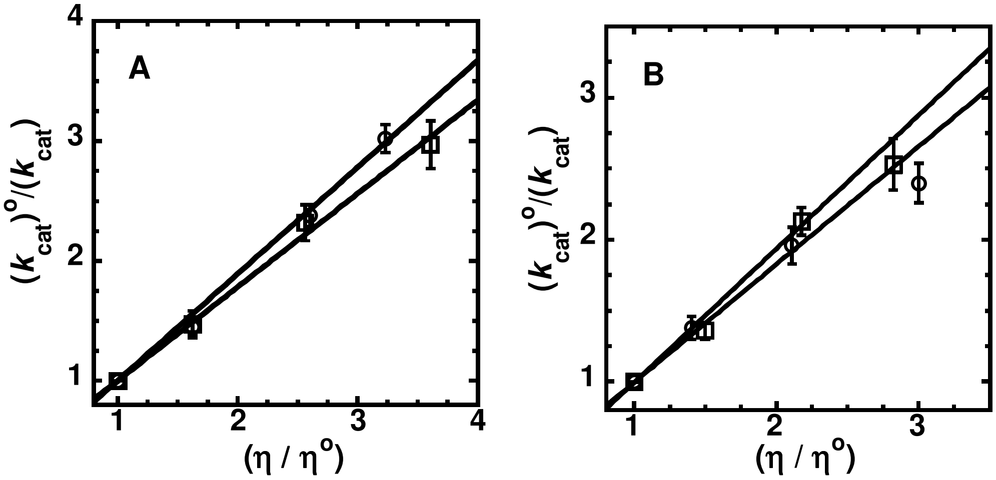

FIGURE 26. Effect of solvent viscosity on the k_{cat} value (A) at 5 °C and (B) at 30 °C for sucrose (circles) and trehalose (squares) as viscogens. The solid lines are linear regression fits with slopes corresponding to the viscosity effects reported in Table 6.

Effects of viscosity on k_{cat}/K_m values reflect contributions of diffusional events to the steps in catalysis up to and including the first irreversible step. Since substrate entry into the active site is expected to be diffusion limited, the degree of rate limitation for substrate binding can be deduced from viscosity effects on k_{cat}/K_m (*96, 98-101*). The effects of sucrose and trehalose on the k_{cat}/K_m values for both 6MPH$_4$ and tyrosine were determined. The results are summarized in Table 6. Sucrose and trehalose had similar effects on k_{cat}/K_m for tyrosine at both 5 °C and 30 °C (Figure 27). The values suggest that the k_{cat}/K_m value for tyrosine is ~50% limited by diffusion of tyrosine into the active site.

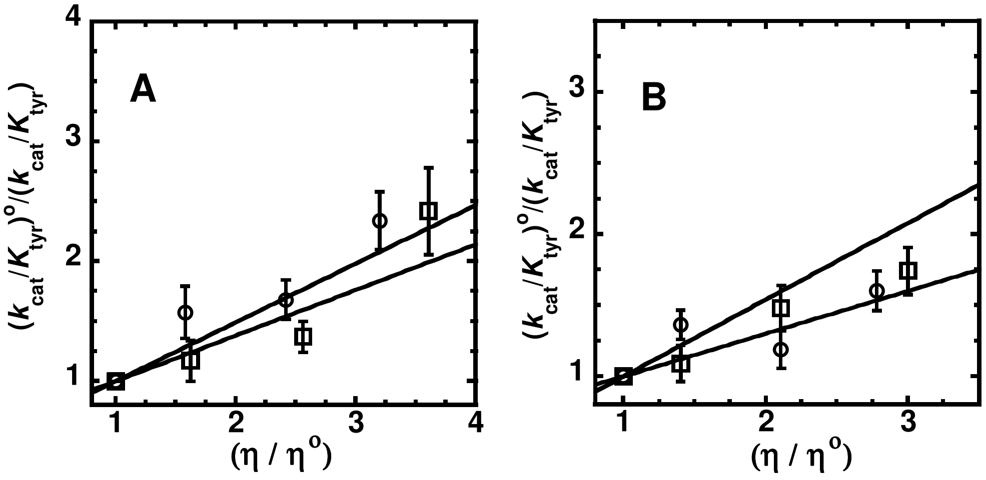

FIGURE 27. Effect of solvent viscosity on the k_{cat}/K_m value for tyrosine at (A) 5 °C and (B) 30 °C for sucrose (circles) and trehalose (squares) as viscogens. The solid lines are linear regression fits with slopes corresponding to the viscosity effects reported in Table 6.

The viscosity effects on k_{cat}/K_{tyr} were also used to calculate the association rate constant (k_1) and the forward commitment (k_2/k_{-1}) for tyrosine according to eq 5 (*96*), where k_1 and k_{-1} are the rate constants for the association and dissociation of tyrosine, respectively, and k_2 is the rate constant for the first irreversible step. The resulting numbers are given in Table 7.

Table 7. Values of Association Rate Constants and Forward Commitments for Tyrosine Binding, Calculated from Viscosity Effects on k_{cat}/K_{tyr} according to eq 5 as Described in Experimental Procedures.

Temp (°C)	k_1 (mM^{-1}s^{-1})	k_2/k_{-1}
5	$1.22\times10^3 \pm 320$	1.03 ± 0.62
30	$7.04\times10^3 \pm 2.02\times10^3$	0.93 ± 0.60

For 6MPH$_4$, the viscosity effects on the k_{cat}/K_m value exhibited significant variation with temperature and with the viscogen used (Figure 28 and Tables 6). At 5 °C, for both sucrose and trehalose, the effect on k_{cat}/K_{6MPH4} was much lower than at 30 °C (Figure 28B and Table 6). Theoretically, the maximum value a viscosity effect can take is 1.0 (*96*). At 30 °C, the values observed for k_{cat}/K_{6MPH4} were significantly greater than 1.0 with both viscogens. Such deviations from the expected limit have been attributed to internal movements in proteins that occur concomitantly with binding events or other diffusional processes (*103, 105-107*).

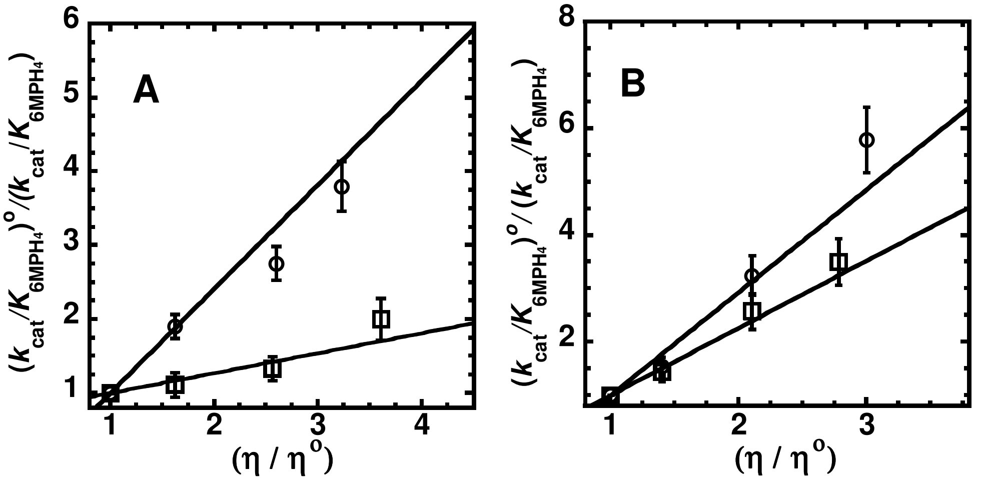

FIGURE 28. Effect of solvent viscosity on the k_{cat}/K_m value for $6MPH_4$ at (A) 5 °C and (B) 30 °C for sucrose (circles) and trehalose (squares) as viscogens. The solid lines are linear regression fits with slopes corresponding to the viscosity effects reported in Table 6.

Single Turnover Stopped-Flow Experiments. Pterin species that form during the reaction of TyrH can be monitored in the UV-Visible region (200-450 nm) using stopped-flow absorbance spectroscopy (*69*). Global kinetic analysis of the single-wavelength absorbance traces up to ~5 s in Chapters II and III established the rate constants for the initial steps in TyrH reaction. In this study, an anaerobic solution of TyH(430 μM):$6MPH_4$(1.3 mM):Tyr(750 μM) was mixed with an equal volume of the oxygenated buffer (400 μM and 270 μM with and without sucrose respectively) at 5 °C in the absence and presence of sucrose (22%, w/w). The concentration of oxygen was limiting to assure single turnover conditions. The data up to 30 s were initially analyzed by fitting the absorbance traces at 246 nm and 318 nm concomitantly to various sequential mechanisms using the program SpecFit to get estimates for the number of observable phases and rate constants (*10*). A three step sequential mechanism accounted well for the traces in the absence of sucrose, with rate constants of 15 s^{-1}, 0.7 s^{-1} and 0.02 s^{-1}, respectively. However, a four step sequential mechanism was required to fit the absorbance data in the presence of sucrose, with rate constants of 15 s^{-1}, 0.7 s^{-1} , 0.66 s^{-1} and 0.02 s^{-1}, respectively . This suggested that the additional phase is due to a viscosity sensitive step that becomes distinguishable only in the presence of sucrose. In order to address this issue, a more extensive kinetic analysis was carried out by simulating both absorbance traces simultaneously using the program KinTek. The analysis initially employed the known values for the rate constants and extinction coefficients for the steps that were studied in previous chapters and the estimates from SpecFit analysis. For the rest of the parameters, a step by step fitting procedure was carried out by Kintek in which only one or two parameters were varied at a time and the rest of the parameters kept constant. A five-step mechanism shown in Scheme 12 accounts well for the data in the absence and presence of sucrose (Figure 29). Both data sets can be simulated well with the same group of rate constants and extinction coefficients with the exception of the fourth step, which corresponds to the additional exponential term observed in the presence of sucrose when the data is fit as the sum of exponentials. The rate constants and extinction changes used in the simulations as parameters are given in Tables 8 & 9. The first step in this mechanism is the oxygen-binding step with no observable absorbance change and the rate constant used in the simulations for this step was taken directly from Chapter III. The second step is the first step with an observable absorbance change and corresponds to the concomitant formation of Fe(IV)O and 4a-hydroxypterin, with a rate constant of 24 s^{-1}, in agreement with the results in Chapter II. The third step exhibits an increase at 246 nm and a decrease at 318 nm, with a rate constant of 0.8 s^{-1}

and accounts for much higher absorbance changes at both wavelengths in comparison to the second step. The fourth step of the mechanism could not be simulated with the same rate constant for data sets obtained in the absence and presence of sucrose. There is almost a 2.3-fold decrease in this rate constant (1.3 s^{-1} vs. 3.0 s^{-1}) when sucrose is present in the reaction medium, consistent with the relative viscosity of 2.4 at this sucrose concentration. The final step in the simulated mechanism is the slow dehydration of 4a-hydroxypterin to give quinonoid dihydropterin in solution with a rate constant of 0.02 s^{-1} (*69*).

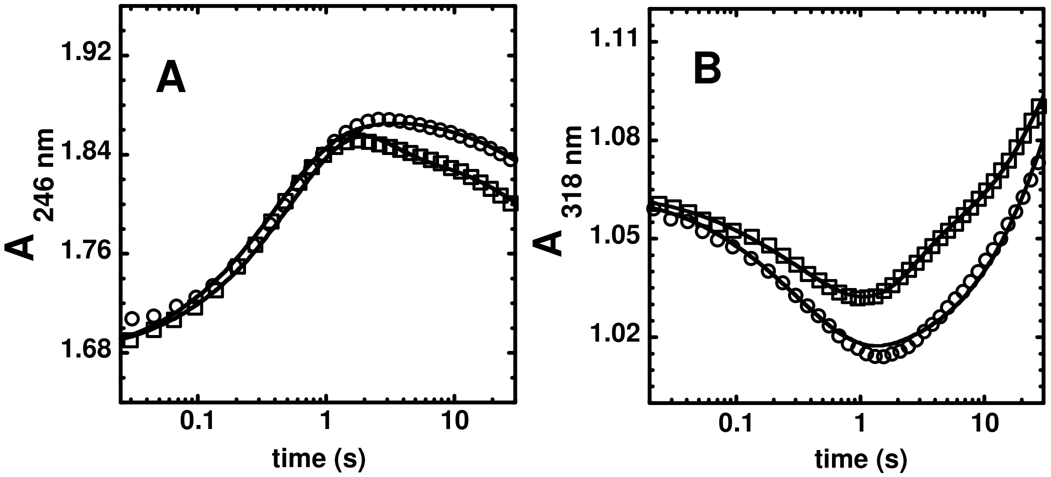

FIGURE 29. Stopped-flow absorbance traces at 246 nm (A) and 318 nm (B) for the reaction of 215 μM TyH:Fe(II):6MPH$_4$:Tyr with 200 μM O_2 in the absence of sucrose (circles) and with 135 μM O_2 in the presence of 22% (w/w) sucrose (squares). The solid lines are from simulations of the data at 5 °C to the mechanism in Scheme 12, using the rate constants and the extinction coefficients in Tables 8 & 9.

Scheme 12

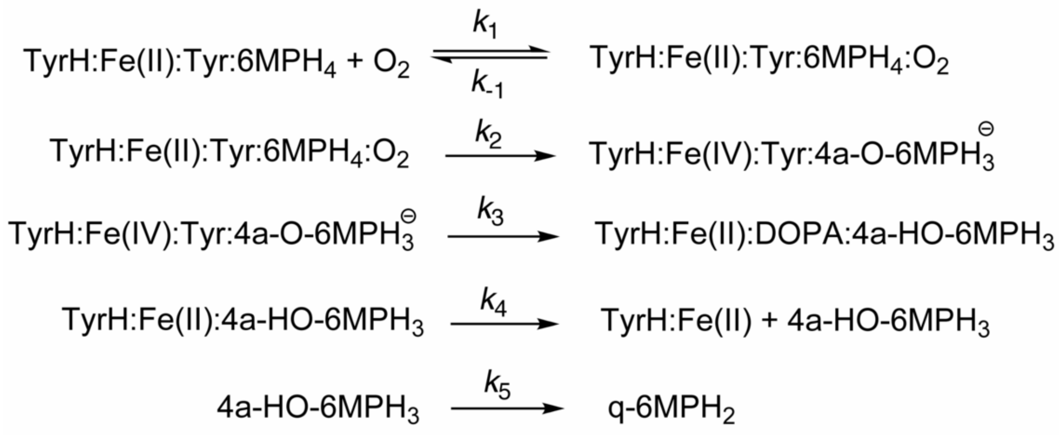

Table 8. Rate Constants and Associated Extinction Changes Obtained from Simulation of the Stopped-Flow Absorbance Traces in the Absence of Viscogen to the Mechanism in Scheme 12. Reaction Conditions Were 200 mM Hepes (pH 7.5), 0.1 M KCl at 5 °C.

Step	Rate Constant	$\Delta\varepsilon_{246\ \mathrm{nm}}$ ($\mathrm{mM^{-1}cm^{-1}}$)	$\Delta\varepsilon_{318\ \mathrm{nm}}$ ($\mathrm{mM^{-1}cm^{-1}}$)
k_1	300 $\mathrm{mM^{-1}s^{-1}}$	0	0
k_{-1}	50 $\mathrm{s^{-1}}$	0	0
k_2	24 $\mathrm{s^{-1}}$	+ 1.8	- 0.6
k_3	0.8 $\mathrm{s^{-1}}$	+ 9.9	- 2.6
k_4	3.0 $\mathrm{s^{-1}}$	- 7.0	+ 2.0
k_5	0.02 $\mathrm{s^{-1}}$	- 2.0	+ 3.6

Table 9. Rate Constants and Associated Extinction Changes Obtained from Simulation of the Stopped-Flow Absorbance Traces in the Presence of Viscogen to the Mechanism in Scheme 12. Reaction Conditions Were 200 mM Hepes (pH 7.5), 0.1 M KCl, 22 % (w/w) Sucrose at 5 °C.

Step	Rate Constant	$\Delta\varepsilon_{246\ \mathrm{nm}}$ ($\mathrm{mM^{-1}cm^{-1}}$)	$\Delta\varepsilon_{318\ \mathrm{nm}}$ ($\mathrm{mM^{-1}cm^{-1}}$)
k_1	300 $\mathrm{mM^{-1}s^{-1}}$	0	0
k_{-1}	50 $\mathrm{s^{-1}}$	0	0
k_2	24 $\mathrm{s^{-1}}$	+ 2.0	- 0.6
k_3	0.8 $\mathrm{s^{-1}}$	+ 10.5	- 2.0
k_4	1.3 $\mathrm{s^{-1}}$	- 6.6	+ 2.1
k_5	0.02 $\mathrm{s^{-1}}$	- 3.4	+ 3.9

DISCUSSION

Recent studies towards the elucidation of the mechanism of TyrH established direct evidence for the involvement of Fe (IV)O as the hydroxylating intermediate in the catalytic cycle. These studies also revealed that the rate of DOPA formation is significantly faster than k_{cat} of the enzyme obtained in steady-state assays. Although earlier studies (*21*) suggested formation of the hydroxylating intermediate as being the rate-limiting step in TyrH reaction, recent observation indicated that chemical steps up to and including the step for DOPA formation are not rate limiting. In this study, we used a combination of pre-steady-state and steady-state techniques to determine the nature of the steps that contribute to the overall rate of the catalysis.

Rapid chemical quench experiments performed at multiple turnover conditions clearly show the presence of a DOPA burst during the first turnover of the reaction. The rate constant for this burst phase matches that for DOPA formation rate obtained in Chapter II at 5 °C. The presence of the burst indicates that a slow step subsequent to formation of DOPA is at least partially rate-limiting. A likely candidate for such a step is a product release step or a conformational change associated with product release (*97, 107*).

Product release is a diffusional event, thus the rate of this step is dependent on solvent viscosity (*96*). For a completely rate-limiting event, the viscosity effect takes a value of 1 and partial rate-limiting steps take values between 0 and 1 (*96, 100*). With TyrH, we obtained a slope of about ~0.9, close to the theoretical maximum value of 1, showing that k_{cat} for the TyrH reaction is almost completely limited by diffusion. This can be interpreted as product release, rather than a conformational change, being strictly rate limiting (*97, 107*).

In order to further test the consistency of rapid chemical quench results with viscosity effects, the burst and linear phase rate constants from rapid chemical quench data were used to calculate the theoretical viscosity effects on k_{cat} using eq 6 (*99, 100*). A value of 0.95 at 5 °C and a value of 0.85 at 30 °C were determined from this analysis. These are very similar to the experimental values obtained from the analysis of the steady-state data (Table 6). Overall, rapid chemical quench and steady-state viscosity experiments are in good agreement, supporting the conclusion that the first turnover in TyrH reaction is substantially limited by a diffusion controlled event, most probably a product release step.

$$(k_{cat})^{\eta} = k_{burst}/(k_{burst} + k_{linear}) \qquad (6)$$

Further mechanistic insight was obtained through analysis of the viscosity effects on k_{cat}/K_m values for both tyrosine and $6MPH_4$. In general these effects are indicative of forward commitment (k_2/k_{-1}) to catalysis (*96, 98*). The viscosity effects on k_{cat}/K_m for tyrosine allowed calculation of the forward commitments at 5 °C and 30 °C (Table 7). The commitment values indicate that the dissociation rate constant for tyrosine is comparable to the value of the rate constant for the first irreversible step of the reaction at both temperatures, consistent with a moderate forward commitment to catalysis for tyrosine binding. The first irreversible step in the TyrH reaction is either a chemical step preceding Fe(IV)O formation, most likely the formation of the proposed iron-peroxypterin bridge, or formation of Fe(IV)O. In the latter case, the rate constant at 5 °C is known. This rate constant, 24 s^{-1}, can be taken as the lower limit for the first irreversible step, placing a lower limit on the dissociation rate constant for tyrosine of 15-75 s^{-1}.

The viscosity effect on k_{cat}/K_m for $6MPH_4$ is well above 1 for all conditions (except when trehalose is the viscogen at 5 °C), the theoretical limit for a diffusion-limited event. However, in systems where there is an accompanying conformational change upon binding of a substrate, slopes over 1 have been observed and this behavior attributed to the cumulative effect of more than one diffusional events (*103, 105-107*). According to Kramer's theory, which relates the effects of friction on unimolecular diffusive events to their rate constants, the free energy barrier will be inversely proportional to the solvent friction, which is a function of solvent viscosity (η) (*108, 109*). In the case of $6MPH_4$ binding, the solvent friction that retards the encounter of $6MPH_4$ with the enzyme will increase the free energy barrier. In addition, for a protein conformational change coupled with binding event, the interaction of the moving portion of the protein with viscogen molecules will further increase the energy barrier, resulting in upward deviation from the maximum slope value, as in the case of $6MPH_4$ binding for TyrH. Since sucrose and trehalose molecules are not expected to diffuse inside the protein, this moving portion of the protein should be located on the protein surface.

In fact, previous studies on TyrH using fluorescence anisotropy showed that the movement of a catalytically important mobile surface loop (consisting of amino acid residues 177-193) from a solvent exposed position towards the active site is associated with $6MPH_4$ binding (*33, 34*). This is in good agreement with the deviation observed for the viscosity effect on k_{cat}/K_m for $6MPH_4$. Hydrogen/Deuterium exchange studies revealed that this loop shows a high percentage of deuterium incorporation in the resting state of the enzyme, suggesting significant interaction between loop residues and solvent molecules (*110*). Loop residues can make hydrogen bonding interactions directly with viscogen molecules as well as with water molecules surrounding viscogen molecules. In addition to their available groups for hydrogen bonding, both sucrose and trehalose can affect the dynamic structure of the water molecules in their vicinity (*111, 112*). The altered interactions in the presence of viscogen molecules could stabilize the resting position of the loop before $6MPH_4$ binding, thus increasing the energy barrier for movement of the loop from the surface.

The viscosity effects on k_{cat}/K_m for $6MPH_4$ show a dependency on the nature of the viscogen and on temperature. The effects obtained in the presence of sucrose are higher than those obtained in the presence of trehalose (Table 6). In addition, only in the case of trehalose at 5 °C is the viscosity effect on k_{cat}/K_m for $6MPH_4$ below unity (~0.3), possibly indicating that the effect from internal movements of the protein is absent and only the effect on $6MPH_4$ diffusion is observed. These observations imply that there are differences in the interaction behavior of sucrose and trehalose molecules with the surface of the protein and with water molecules. Although sucrose and trehalose are both disaccharides of the same molecular weight, the differences in the orientation of their hydroxyl groups at chiral carbon atoms lead to different hydration and interaction patterns (*111*), thus sucrose and trehalose will set different energy barriers for loop movement. Such a pattern might arise from differences in either direct hydrogen bonding interactions between viscogen molecules and the protein surface or in the perturbations of the hydrogen bonding network between water molecules and the protein surface. For the latter case, studies show that dynamic structure of the water molecules are affected to different extents by sucrose and trehalose (*112, 113*). Sucrose has been reported to make more hydrogen bonding interactions with the protein than trehalose in the case of carboxy-myoglobin (*112*). Trehalose molecules are more effective in decreasing the mobility of water molecules in their surroundings (*113, 114*). These observations may account for the viscogen-dependent variations observed in TyrH system of the viscosity effects on k_{cat}/K_m values for $6MPH_4$.

The viscosity effects for k_{cat}/K_{6MPH4} also exhibits a temperature-dependent variation. The effects at 30 °C are much higher at 5 °C for both viscogens. This behaviour can be explained if the temperature dependence of the free energy barrier for the viscogen-loop interaction is different from the temperature dependence of the free energy barrier for diffusional encounter of the enzyme and $6MPH_4$.

In order to gain more insight into the intrinsic rate constants that contribute to the k_{cat} for TyrH reaction, the progress of the reaction was monitored by stopped-flow absorbance spectrophotometer in the absence and presence of the viscogen sucrose. These experiments allowed us to dissect the individual steps as viscosity dependent or viscosity independent. Single wavelength traces from the two experiments performed in the absence and presence of sucrose can be simulated with the same set of rate constants, except the fourth step, and with similar extinction coefficients (Scheme 12, Table 8&9). Slight differences in extinction changes between the experiments, with and without sucrose, can be attributed to the perturbed absorbance spectra of pterin species due to sucrose. The rate constants obtained for the first and second steps of this mechanism, the oxygen binding step and subsequent 4a-hydroxypterin formation step, respectively, are in agreement with the studies presented in Chapters II and III. The absorbance changes for the second step are less than that would be expected for the formation of 4a-hydroxypterin at neutral pH (*69*). However, the amplitude of the sum of the absorbance changes for the second and third steps at both wavelengths, 246 nm and 318 nm, are consistent with the formation of 4a-hydroxypterin from $6MPH_4$. This suggests that the species that form in the second step is a deprotonated form of 4a-hydroxypterin and the third step is the protonation of this species, giving the expected form of 4a-hydroxypterin at neutral pH. Absorption spectra of the basic and neutral forms of 4a-hydroxypterin derivatives reported in literature support this assumption for the extinction change at 246 nm (*42*).

The decrease in the rate constant of the fourth step of the mechanism (Scheme 12) upon increasing viscosity is indicative of a diffusion-limited step. The relative viscosity of the reaction medium with sucrose is 2.4 at the experimental conditions used. If this step is a product release step, the ratio of the rate constants for this step in the presence and absence of viscogen should be close to the relative viscosity value of 2.4 (*97, 107*). A rate decrease of 2.3-fold was obtained for the rate constants from simulations (3 s^{-1} vs. 1.3 s^{-1}), which strongly supports that this step is product release. The fourth step is also associated with absorbance changes at both 246 nm and 318 nm in the absence and presence of sucrose. Thus it is reasonable to attribute this step to the release of 4a-hydroxypterin and not DOPA, which does not absorb at these wavelengths. The extinction changes for this step are possibly due to the differences in the absorbance spectra of 4a-hydroxypterin inside the enzyme active site and in solution.

$6MPH_4$ is the first substrate to bind in TyrH catalysis. This suggests that DOPA is the first product to be released followed by 4a-hydroxypterin. Although DOPA release is not detectable by absorption spectroscopy, a step prior to 4a-hydroxypterin release can be added as a DOPA release step to the mechanism in Scheme 12 (Scheme 13). Since the first and the second steps are much faster than the subsequent steps, eq 7 can be used to calculate the rate for DOPA release (the final step is a non-enzymatic step in solution, so it was not taken into account in this calculation). Using an average value of 0.5 s^{-1} for k_{cat} obtained from steady-state assays and the rate constants of k_3 and k_4 from simulations (Scheme 12, Table 8), a value of 2.4 s^{-1} was determined as the DOPA release rate in the absence of sucrose. If the same calculation is carried out to calculate the DOPA release rate in the presence of sucrose, using rate constants of 0.8 s^{-1} for k_3 and 1.3 s^{-1} for k_4 from Table 9 and a k_{cat} value of 0.23 s^{-1} (calculated from the linear regression fit of relative k_{cat} vs. relative viscosity) a rate of 0.6 s^{-1} is obtained. Theoretically the rate decrease for the DOPA release step can not be more than 2.4-fold, the relative viscosity value of the reaction medium. Since the rate calculated in the absence of viscogen for DOPA release step is 2.4 s^{-1}, the lowest value that the rate constant of the same step in the presence of viscogen can take is 1 s^{-1}. However, the actual value calculated as above is 0.6 s^{-1}, much lower than 1 s^{-1}, the theoretical lowest limit. This result suggests the presence of other slow diffusion-limited steps coupled with the release step, most possibly conformational changes. Since $6MPH_4$ binding has already been shown to be associated with a surface loop movement that causes significant effect on K_{6MPH4} *(vide supra)*, it is reasonable to expect a viscosity effect that will further lower k_{cat}, as the loop moves back to its initial position during the release event. Thus, a combination of release events and conformational changes are most likely to be responsible for the significant viscosity dependence of k_{cat} of TyrH reaction.

$$k_{\mathrm{cat}} = (k_3 k_4 k_{\mathrm{DOPA}})/(k_3+k_4+k_{\mathrm{DOPA}}) \tag{7}$$

Scheme 13

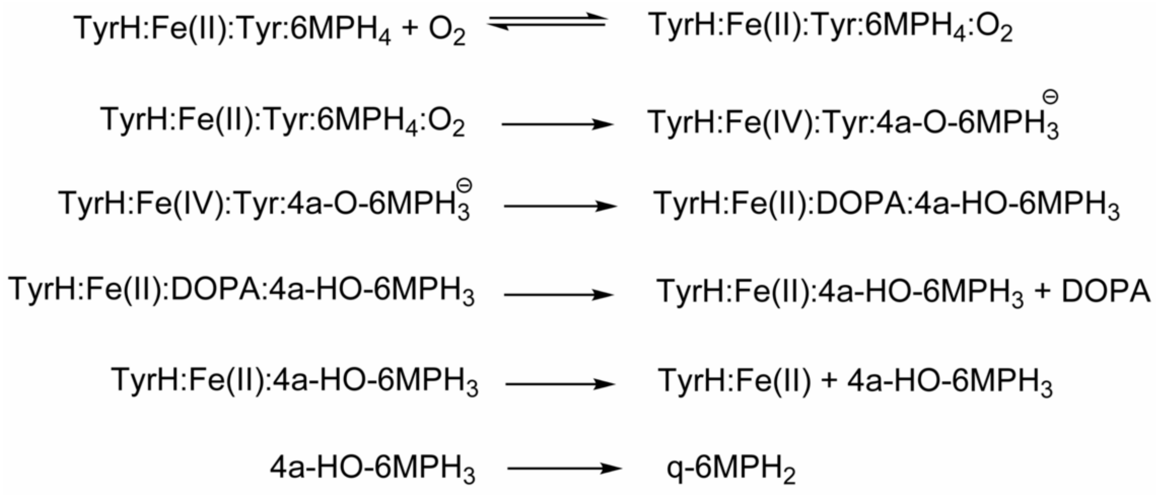

Overall this study brings further insight into the mechanism of TyrH. Product burst and viscosity studies showed that chemistry is not rate determining in TyrH catalysis and that product release makes a significant contribution to the rate-limiting step. Stopped-flow analysis further showed that k_{cat} of the reaction is determined by a combination of chemical and physical steps; possibly protonation of 4a-hydroxypterin at the enzyme active site, diffusion-limited release of DOPA and 4a-hydroxypterin and an associated conformational change. The relative magnitude of the rate constants for these steps indicates that conformational change makes a significant contribution to the overall rate of the catalysis. Viscosity effects measured on $k_{\mathrm{cat}}/K_{\mathrm{m}}$ for $6MPH_4$ brings further insight, supporting the coupling of the movement of a surface loop with $6MPH_4$ binding, as indicated in earlier studies with different techniques.

CHAPTER V

SPECTROSCOPIC INVESTIGATION OF THE NITRIC OXIDE COMPLEXES OF TYROSINE HYDROXYLASE

INTRODUCTION

All members of the AAH family share a similar mechanism (*21*). The proposed mechanism for TyrH is shown in Scheme 1. The mechanism involves formation of the hydroxylating intermediate, Fe(IV)O, and subsequent reaction of this intermediate with the aromatic ring to give the product, DOPA, through electrophilic aromatic substitution. Studies on TyrH presented in the previous chapters have revealed the active site structure in the absence and presence of amino acid substrate/pterin cofactor and brought insight into the oxygen reactivity of iron as well as provided evidence for the identity of the hydroxylating intermediate that forms when the O-O bond is cleaved *(vide supra)*. However, it hasn't been possible up to date to trap and investigate possible intermediate complexes before the cleavage of the O-O bond with bound molecular oxygen, due to the rapid reactivity of oxygen with the active site iron *(vide supra).*

NO has been used as an O_2 analogue for many non-heme enzyme systems and for model complexes (*115-122*). In addition to its advantage of being a dioxygen analogue, NO also converts EPR silent high-spin ferrous systems (S = 2) to an EPR active form with a spin of S = 3/2. This EPR active form is denoted as $\{FeNO\}^7$, where 7 is the the sum of the Fe d and NO π^* electrons and the spin state, S = 3/2, is described as the antiferromagnetic coupling of a S = 5/2 ferric center with S = 1 NO^- (*115, 118*). NO binding to the active site iron also provides a visible chromophore that can be monitored by optical absorption spectroscopy (*115-117, 122*). Thus, investigation of the NO complexes of Fe(II) enzymes have two significant benefits: 1) the electronic environment of active site Fe(II) upon binding of substrates and cofactors can be probed; and 2) spectroscopic information on the NO bound enzyme complexes provides insight into O_2 bound intermediates that would otherwise be impossible to trap due to the rapid reactivity of O_2.

This chapter will describe studies conducted on the NO complexes of TyrH by means of visible absorption and EPR spectroscopy in order to get a better understanding of the electronic structure of Fe(II) in TyrH. In addition to CW EPR, a pulsed-EPR technique, ESEEM (Electron Spin Echo Envelope Modulation) was also used for further investigation of the NO complexes of TyrH, in collaboration with the lab of Dr. John McCracken at Michigan State University.

EXPERIMENTAL PROCEDURES

Materials. 6-Methyltetrahydropterin ($6MPH_4$) and 6-methylpterin were purchased from Schircks Laboratories (Jona, Switzerland). Methylamine hexamethylene methylamine (MAHMA NONOate), ethylenediamine tetraacetic acid (EDTA), L-tyrosine and glycerol were from Sigma-Aldrich (St. Louis, MO). L-3,5-$^2H_2$-Tyrosine and deuterium gas were from Cambridge Isotopes (Andover, MA). Potassium chloride and ferrous ammonium sulfate were from Fisher (Pittsburg, PA). All other chemicals were of the highest purity commercially available.

Protein Purification. Wild-type TyrH and F184A TyrH were expressed in *E. coli* and purified as previously described (*33, 61)* In order to remove iron from the protein, the ammonium sulfate pellet at the end of the purification was resuspended in 5 mM EDTA, 200 mM Hepes, (pH 7.5), 10% glycerol and 0.1 M KCl, and incubated on ice for one hour. The enzyme solution was then dialyzed against the same buffer without EDTA and concentrated using Amicon Ultra-15 and Ultra-4 centrifugal filters (Millipore Corp., MA). The enzyme samples for ESEEM were brought to a final glycerol concentration of 30% (v/v) during the concentration stage. The iron content of the apo-enzyme was measured using a Perkin-Elmer AAnalyst600 atomic absorption instrument. Typical iron content of an apo enzyme preparation was ~0.1 equivalent.

Snythesis of Deuterated 6MPH$_4$. Deuterated 6MPH$_4$ was synthesized by reduction of the commercially available 6-methylpterin to the level of tetrahydropterin using deuterium gas, as previously described (*123*).

Preparation of NO Samples for Spectroscopy. Methylamine hexamethylene methylamine (MAHMA NONOate) was used as the nitric oxide donor. Stock solutions of MAHMA NONOate were prepared in 0.01 M NaOH just before the experiment and were always kept on ice. Exact concentrations of the MAHMA NONOate solutions were determined from the UV absorbance at 250 nm in 0.01 M KOH, using an extinction coefficient of 7.3 mM^{-1}cm^{-1}(*124*). Highly concentrated stock solutions of tyrosine and 3,5-^{2}H$_2$-tyrosine (~50 mM) were prepared by bringing the solution to a final pH of ~10. The exact concentrations of the tyrosine stock solutions were determined using an extinction coefficient of 1.34 mM^{-1}cm^{-1} at 275 nm in 0.1 M HCl. Stock solutions of the proteated and deuterated 6MPH$_4$ were prepared in 2 mM HCl and an extinction coefficient of 17.8 mM^{-1}cm^{-1} in 2 M perchloric acid was used to determine the concentrations. Ferrous ammonium sulfate solutions were prepared fresh by dissolving the appropriate amount of powder in 2 mM HCl. Samples for the UV-Visible and EPR experiments were prepared inside an anaerobic cuvette at 25 °C. Apo TyrH (~100 uM for UV-Vis and EPR experiments, 0.9-1.2 mM for ESEEM experiments) and tyrosine (if the complex contains tyrosine) was placed at the bottom of the cuvette. Ferrous ammonium sulfate solution (0.9 equivalent in ~10 μl) was placed on the lower neck of the cuvette. $6MPH_4$ and MAHMA NONOate solutions were either placed in the side arms or on the upper neck of the cuvette, for large and small volumes, respectively. Buffer conditions were 250 mM Hepes (pH 7.4), 10% glycerol, 0.1 M KCl for UV-Visible and EPR experiments and 100 mM Mops (pH 7.0), 0.3 M KCl and 30% glycerol for ESEEM experiments. Each MAHMA NONOate molecule releases two molecules of NO (*124*) and the half-life of MAHMA NONOate is ~35 s under these buffer and temperature conditions (data not shown). The contents of the cuvette (a total volume of 400-800 μl) were made anaerobic by the application of argon-vacuum exchange for at least 20 minutes. The anaerobic enzyme solution was then mixed with ferrous ammonium sulfate and incubated for 10 minutes. This was followed by mixing with $6MPH_4$ (if the complex contained $6MPH_4$). After 3 minutes, a blank was taken by the UV-Visible spectrophotometer (Hewlett-Packard model HP 8453). Finally MAHMA NONOate (~1 equivalent of the enzyme for UV-Visible and EPR samples and ~0.6 equivalent of the enzyme for ESEEM samples) at the upper neck of the cuvette was introduced to the enzyme-substrate mixture and the UV-Visible spectra were taken at 1 min periods until the maximum absorbance at 450 nm is reached, which takes about 3-5 minutes under the experimental conditions. At this point, ~200 μl of the reaction mixture was quickly transferred to the quartz EPR tubes (4 mm OD, 707-SQ-250M, Wilmad, Buena, NJ) using a glass pipette and immediately frozen in liquid nitrogen. UV-Visible spectra collected at increasing concentrations of MAHMA NONOate showed that NO was saturating under the concentrations used.

EPR Spectroscopy. EPR spectra were taken at 10 K using a Bruker EMX X-band EPR spectrometer operating in perpendicular mode with an Oxford instruments EM 910 cryostat. The frequency was 9.45 GHz and the microwave power was 2 mW, which was non-saturating as determined from spectra taken at various powers. g-values of the EPR signals were determined from the peak positions measured directly from the spectra. Since the all the EPR spectra measured exhibited low rhombicity ((E/D < 0.15), E/D values were determined from g_x and g_y using eqs 8 and 9 (*120*). The E/D parameter represents the degree of distortion from axial symmetry (where D and E are the axial and rhombic zero-field splitting parameters, respectively).

$$g_x = g_0[2-3(E/D)-3/2(E/D)^2] \tag{8}$$

$$g_y = g_0[2+3(E/D)-3/2(E/D)^2] \tag{9}$$

ESEEM Spectroscopy. ESEEM spectra were collected and analyzed in the laboratory of Dr. John McCracken at Michigan State University by Matthew Krzyaniak, as following. Measurements were made on a Bruker E-680X spectrometer operating at X band and equipped with a model ER 4118X-MD-X5-W1 probe that employs a 5 mm dielectric resonator. The temperature was maintained at 4K using an Oxford Instruments liquid helium flow system equipped with a CF-935 cryostat and an ITC-503 temperature controller. ESEEM data was collected using a three-pulse (stimulated echo) sequence, 90°-τ-90°-T-90°, with 90° microwave pulse widths of 16 ns (FWHM). The deuterium contributions to ESEEM spectra were obtained using the ratio method introduced by

Mims (*125*) together with processing tools provided by Bruker. Three-pulse ESEEM data were normalized by dividing each data set by its maximum amplitude. These data were then divided by the corresponding, normalized ^{1}H ESEEM data. This resulted in ESEEM data dominated by ^{2}H. ESEEM spectra were obtained by taking the absolute value of the real part of the Fourier transforms of the time domain data. Simulations of the ^{2}H hyperfine couplings were carried out using scripts written in MATLAB. Parameters for the spin Hamiltonian simulations are given in the figure legends.

RESULTS

UV-Visible Spectra of WT TyrH:Fe(II):NO Complexes. Studies on inorganic Fe:NO model complexes show that formation of an Fe:NO complex gives rise to a number of electronic transitions in the UV-Visible region with fairly low extinctions (less than 1000 $M^{-1}cm^{-1}$) (*115*). Absorptions at 443 nm, 510 nm and 575 nm have been assigned to the NO^- to Fe(III) charge transfer transitions. The most intense of these transitions is the ~450 nm band, and the other two transitions (~510 nm and ~575 nm) generally appear as a shoulder with weaker intensities. The absorption magnitude of these transitions are indicative of the degree of orbital overlap between the d orbitals of Fe(III) and the 2π* orbital of NO^-, which is dependent on the Fe-N-O bond angle (*115, 122*). Another significant transition is a Fe(III) ligand field band observed at ~650 nm (*117*).

The binary (TyrH:Fe(II):NO), ternary (TyrH:Fe(II):NO:tyr and TyrH:Fe(II):NO:6MPH$_4$) and quaternary complexes (TyrH:Fe(II):NO:tyr:6MPH$_4$) of WT TyrH were investigated by UV-Visible absorption spectroscopy. The reaction of NO (60 μM) with resting or substrate/cofactor bound TyH:Fe(II) (100 μM) was monitored over a period of 20 min by acquiring diode-array absorption spectra in the UV-Visible region at every minute after the reaction was initiated. As the NO complex formed, the reaction mixture took on the characteristic bright yellow color of an Fe:NO species, and a well-defined peak was observed at 450 nm with a shoulder extending up to ~600 nm. A broad peak at 650 nm was also observed with much less intensity compared to the 450 nm peak. The maximum absorbance at 450 nm was reached in 3-5 min and started decreasing slowly after ~10 min, indicating the reversibility of NO binding. In order to obtain spectra of the NO complexes of TyrH, the spectra of the enzyme complexes before NO addition were subtracted from the spectra with maximum intensity at 450 nm after NO addition (Figure 30). The largest absorbance intensity for the 450 nm transition was observed for the quaternary (TyrH:Fe(II):NO:tyr:6MPH$_4$) complex with an extinction change of ~800 $M^{-1}cm^{-1}$. The transitions in 500-600 nm region corresponding to the other charge transfer bands and the peak at ~650 nm corresponding to Fe(III) ligand field transition were also much more intense in the quaternary complex in comparison to the binary and ternary complexes. The extinction coefficient varied from 250 to 400 $M^{-1}cm^{-1}$ for the 450 nm transition among the binary and ternary complexes, with TyrH:Fe(II):NO:tyr complex having the most intense peak of all. The peak maximum for the 450 nm transition is shifted to higher energy (435 nm) for the TyrH:Fe(II):NO:6MPH$_4$ complex.

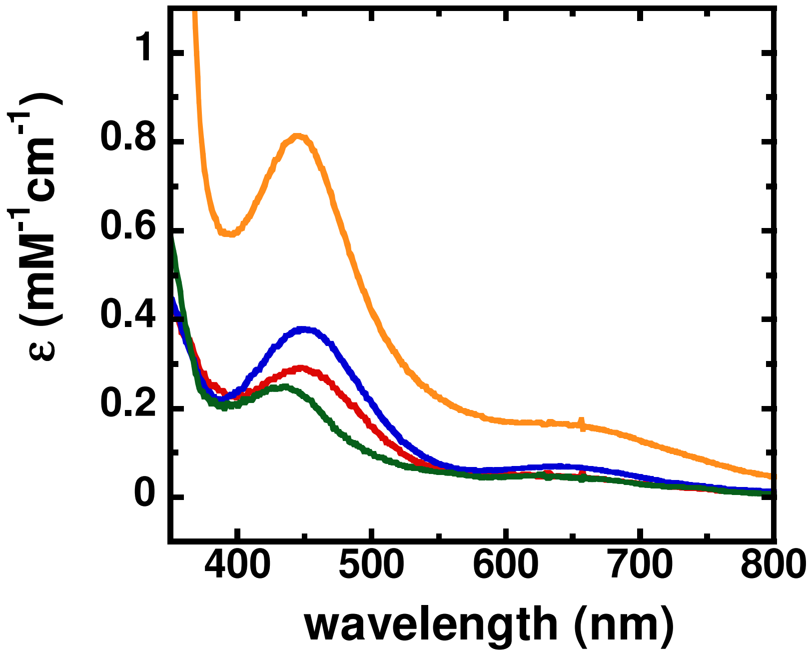

FIGURE 30. UV-visible absorption difference spectra of the NO complexes of TyrH:Fe(II) (red), TyrH:Fe(II):tyr (blue), TyrH:Fe(II):6MPH$_4$ (green) and TyrH:Fe(II):tyr:6MPH$_4$ (orange). Difference spectra were obtained by subtracting the spectrum of each complex before NO addition from the spectrum that has the maximum absorbance value (at ~ 450 nm) after NO addition. Reaction conditions were as follows: 100 μM ferrous TyrH, 300 μM tyrosine, 200 μM 6MPH$_4$ and 100 μM MAHMA NONOate in 250 mM Hepes (pH 7.4), 10 % glycerol, 0.1 M KCl with a final volume of 800 μl at 25 °C.

EPR Spectra of WT TyrH:Fe(II):NO and F184A TyrH:Fe(II):NO Complexes. Although high spin Fe(II) systems have an integer spin of S = 2 and thus are EPR silent, binding of NO to Fe(II) gives an EPR detectable $\{FeNO\}^7$ system, with a spin of S = 3/2, due to the antiferromagnetic coupling of the S = 5/2 ferric center with S = 1 NO^- (*115, 117*). Figure 31 shows the EPR spectra of the NO complexes of WT TyrH. Consistent with previous studies (*115, 122*), all complexes exhibited nearly axial signals with g_x and g_y close to 4 and g_z close to 2. Due to the overlap with the signal of free NO at g = 2, only the informative g = 4 region is shown (*115*). Experimental g-values and E/D parameters are given in Table 10. An increase in the E/D parameter indicates an increase in the degree of the rhombicity of the $\{FeNO\}^7$ spin system (*119*). EPR spectra of TyrH:Fe(II):NO and TyrH:Fe(II):NO:$6MPH_4$ exhibit a single resonance with very similar E/D values suggesting that both complexes exist as a single population and the iron environment is not affected much by $6MPH_4$ binding. The EPR spectrum of the TyrH:Fe(II):NO:tyr is composed of a mixture of two components, indicating the presence of two different populations of enzyme with slightly different active site environments. The more intense component has an E/D value of 0.007 and the minor component exhibits a greater degree of rhombicity with an E/D value of 0.017. The EPR spectrum of the TyrH:Fe(II):NO:tyr:$6MPH_4$ complex also exhibits two overlapping resonances. The major component has an E/D value of 0.018 whereas the minor component has a much larger E/D parameter of 0.053, indicating significant changes around the active site iron with this specific population of enzyme.

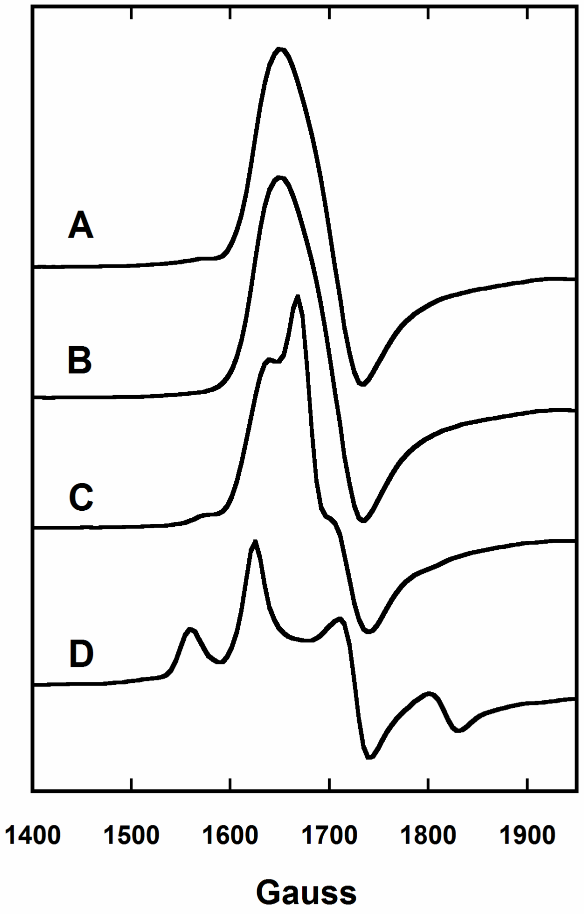

FIGURE 31. EPR spectra of the g = 4 region of the NO complexes of WT TyrH at 10 K. (A) TyrH:Fe(II):NO (B) TyrH:Fe(II):NO:6MPH$_4$ (C) TyrH:Fe(II):NO:tyr (D) TyrH:Fe(II):NO:tyr:6MPH$_4$. Spectra were taken at a frequency of 9.45 GHz and a microwave power of 2 mW. Experimental conditions are as given in the legend of Figure 30.

Table 10. Experimental Parameters Obtained from g = 4 Region of EPR Spectra of the NO Complexes of WT and F184A TyrH.

complex	g_x	g_y	*E/D*
WT TyrH:Fe(II):NO	4.09	3.96	0.011
WT TyrH:Fe(II):NO:6MPH$_4$	4.09	3.93	0.013
WT TyrH:Fe(II):NO:tyr	4.05	3.97	0.007*
	4.12	3.92	0.017
WT TyrH:Fe(II):NO:tyr:6MPH$_4$	4.13	3.91	0.018*
	4.30	3.67	0.053
F184A TyrH:Fe(II):NO	4.09	3.93	0.013
F184A TyrH:Fe(II):NO:6MPH$_4$	4.09	3.93	0.013
F184A TyrH:Fe(II):NO:tyr	4.04	3.97	0.006
	4.09	3.92	0.014
F184A TyrH:Fe(II):NO:tyr:6MPH$_4$	4.13	3.91	0.018
	4.30	3.68	0.052

* Components with higher intensities.

F184 is in the middle of an ~20 amino acid long surface loop (residues 174-194) that moves toward the active site upon 6MPH$_4$ binding and packs against the residues that make up the hydrophobic pocket for the side chain of the substrate tyrosine (*21, 34*). The movement of this loop is believed to play a role in the control of coupling of tyrosine hydroxylation to pterin oxidation by bringing the substrates closer and preventing discharge of the hydroxylating intermediate through prevention of water access to the active site (*33*). F184A TyrH shows a significant decrease in activity and exhibited only ~15% coupling of DOPA formation to 6MPH$_4$ oxidation. This was attributed to the decrease in the rate constant for tyrosine hydroxylation due to perturbation of the position of tyrosine in the active site (*33*). To determine if the activity loss and uncoupling is due to the perturbations of the iron environment of the active site, EPR spectra of the NO complexes of F184A TyrH were collected (Figure 32). Experimental EPR parameters are given in Table 10. The E/D values for the F184A TyrH are very similar to those of WT TyrH. The differences in the shape of the tyrosine and tyrosine/6MPH$_4$ complexes of F184A TyrH spectra in comparison to WT TyrH are likely due to changes in the relative intensities of the components that overlap in g = 4 region. This suggests that the relative amounts of the different populations of the enzyme change in the mutant enzyme compared to WT TyrH.

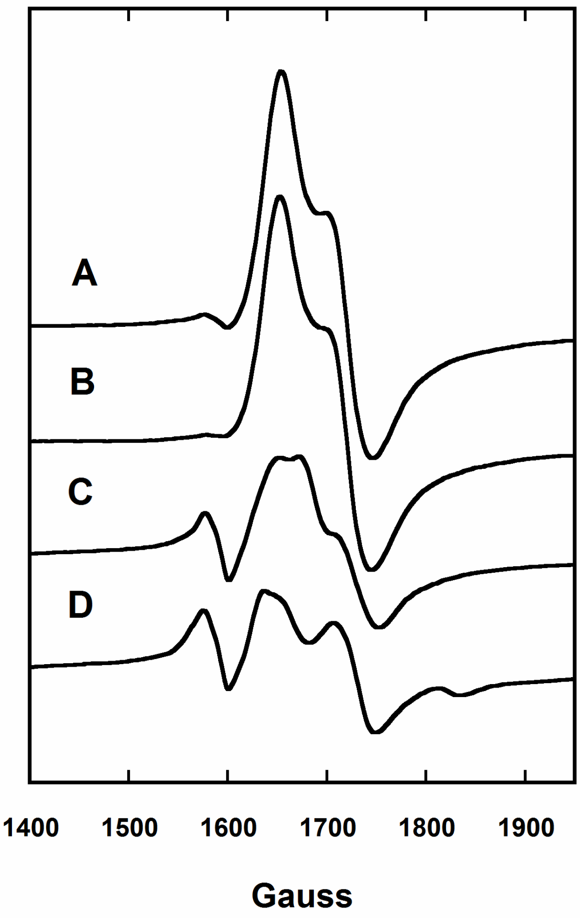

FIGURE 32. EPR spectra of the g = 4 region of the NO complexes of F184A TyrH at 10 K. (A) TyrH:Fe(II):NO (B) TyrH:Fe(II):NO:6MPH$_4$ (C) TyrH:Fe(II):NO:tyr (D) TyrH:Fe(II):NO:tyr:6MPH$_4$. Spectra were taken at a frequency of 9.45 GHz and a microwave power of 2 mW. Experimental conditions are as given in the legend of Figure 30.

ESEEM Spectra of WT TyrH:Fe(II):NO Complexes. ^{2}H ESEEM spectra were obtained for the complexes of TyrH:Fe(II):NO with deuterated and proteated substrate and/or cofactor (Figure 33). This enables identification of the deuterium couplings with Fe-NO spin system, thus giving information about the distance and angle of the substrate/cofactor with respect to the Fe-NO bond (*126*). The ^{2}H ESEEM spectrum of TyrH:Fe(II):NO-[^{2}H-6MPH$_4$] can be simulated with a single deuteron at 5.9 Å from the paramagnetic center with an angle of 57° between the Fe-NO axis and the hyperfine principal axis (Figure 34). The TyrH:Fe(II):NO-[^{2}H-tyrosine] ESEEM spectrum (Figure 35) gives a signal that can be simulated with hyperfine parameters that correspond to a deuterium-Fe distance of 4.33 Å with an angle of 72° between the Fe-NO bond and the deuterium-Fe vector.

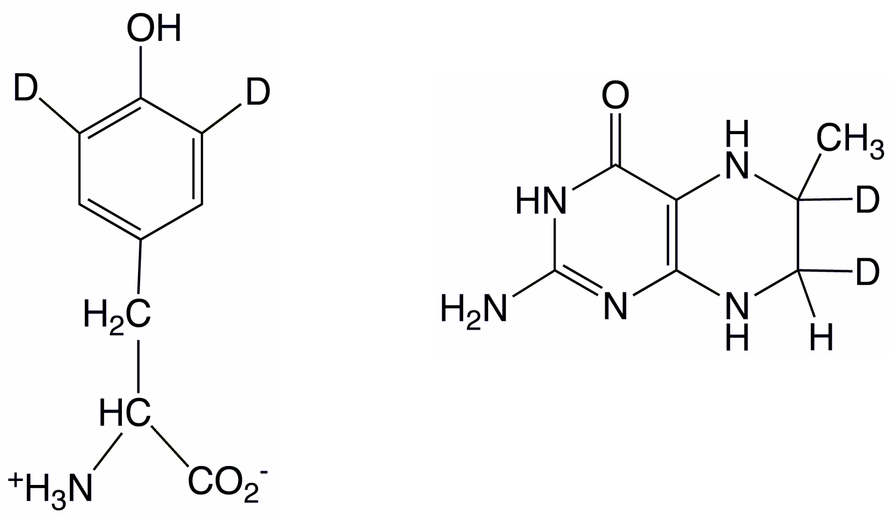

FIGURE 33. Structures of 3,5-deuterated tyrosine (left) and deuterated 6MPH$_4$.

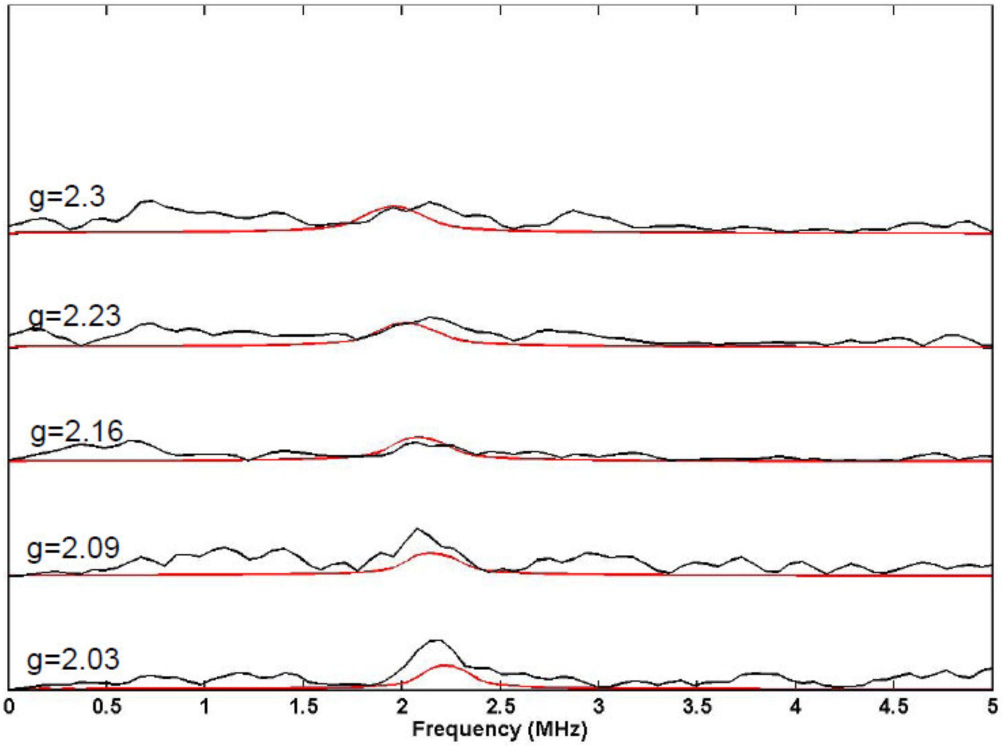

FIGURE 34. ^{2}H ESEEM spectra of TyrH:Fe(II):NO-[^{2}H-6MPH$_4$] at corresponding g values. Red lines are the simulations of the spectra with the following Hamiltonian parameters: principal deuterium hyperfine values of [-0.06, -0.06, 0.12] MHz with Euler angles for the hyperfine tensor of (0, 57°, 0); $e^2qQ = 0.2$ MHz; Euler angles relating the nuclear quadrupole interaction to the hyperfine interaction of (0, 57°, 0). Concentrations were 1.05 mM ferrous TyrH, 1.7 mM ^{2}H-6MPH$_4$ and 0.7 mM MAHMA NONOate in 100 mM Mops (pH 7.0), 0.3 M KCl and 30% glycerol. Samples were prepared at 25 °C.

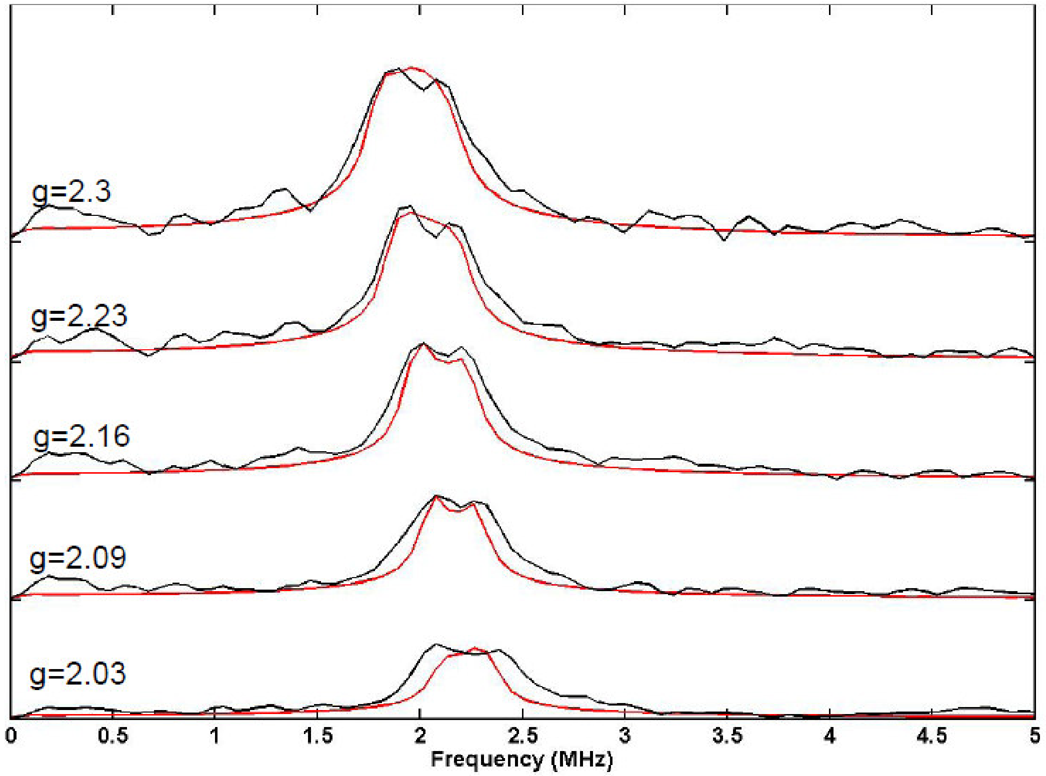

FIGURE 35. ^{2}H ESEEM spectra of TyrH:Fe(II):NO-[3,5-^{2}H-tyrosine] at corresponding g values. Red lines are the simulations of the spectra with the following Hamiltonian parameters: principal deuterium hyperfine values of [-0.15, -0.15, 0.3] MHz with Euler angles for the hyperfine tensor of (0, 72°,0); $e^{2}qQ = 0.2$ MHz; Euler angles relating the nuclear quadrupole interaction to the hyperfine interaction of (0, 40°,0). Concentrations were 0.95 mM ferrous TyrH, 1.3 mM 3,5-^{2}H-tyrosine and 0.7 mM MAHMA NONOate in 100 mM Mops (pH 7.0), 0.3 M KCl and 30% glycerol. Samples were prepared at 25 °C.

The ^{2}H ESEEM spectrum of TyrH:Fe(II):NO-[6MPH$_4$, ^{2}H-tyrosine] can be simulated with a single deuteron-Fe distance of 4.95 Å and with an angle of 69° between the Fe-NO axis and the hyperfine principal axis (Figure 36). The simulations of ^{2}H ESEEM spectrum of TyrH:Fe(II):NO-[^{2}H-6MPH$_4$, tyrosine] are in agreement with a single deuteron at a distance of 4.23 Å from Fe center at an angle of 66° from the Fe-NO axis (Figure 37).

The only available crystal structure of a ternary complex in the AAH family is for PheH (*25*). This crystal structure shows that the first coordination sphere of the iron is rather open on the side opposite from the facial triad. NO binding to this area will be restricted due to the steric hindrance from the substrate and the cofactor. Taking into account this restriction and using the Euler angles and distances obtained from the ESEEM data for TyrH:Fe(II):NO-[3,5-^{2}H-tyrosine, 6MPH$_4$] and TyrH:Fe(II):NO-[tyrosine, ^{2}H-6MPH$_4$], the Fe-NO bond axis can be drawn on the crystal structure of the ternary complex of PheH as the g_z axis (Figure 38).

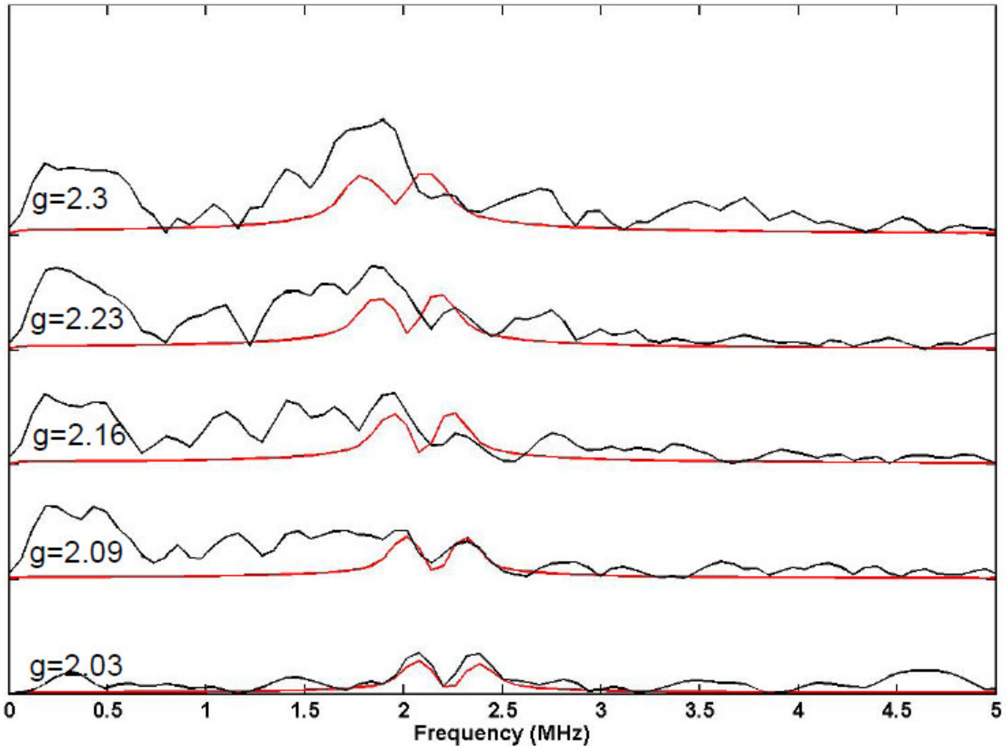

FIGURE 36. ^{2}H ESEEM spectra of TyrH:Fe(II):NO-[3,5-^{2}H-tyrosine, 6MPH$_4$] at corresponding g values. Red lines are the simulations of the spectra with the following Hamiltonian parameters: principal deuterium hyperfine values of [-0.1,-0.1, 0.2] MHz with Euler angles of (0, 69°, 0), $e^2qQ = 0.2$ MHz; Euler angles relating the nuclear quadrupole interaction to the hyperfine interaction of (0, 90°, 0). Concentrations were 0.9 mM ferrous TyrH, 1 mM tyrosine, 1.4 mM ^{2}H-6MPH$_4$ and 0.6 mM MAHMA NONOate in 100 mM Mops (pH 7.0), 0.3 M KCl and 30% glycerol. Samples were prepared at 25 °C.

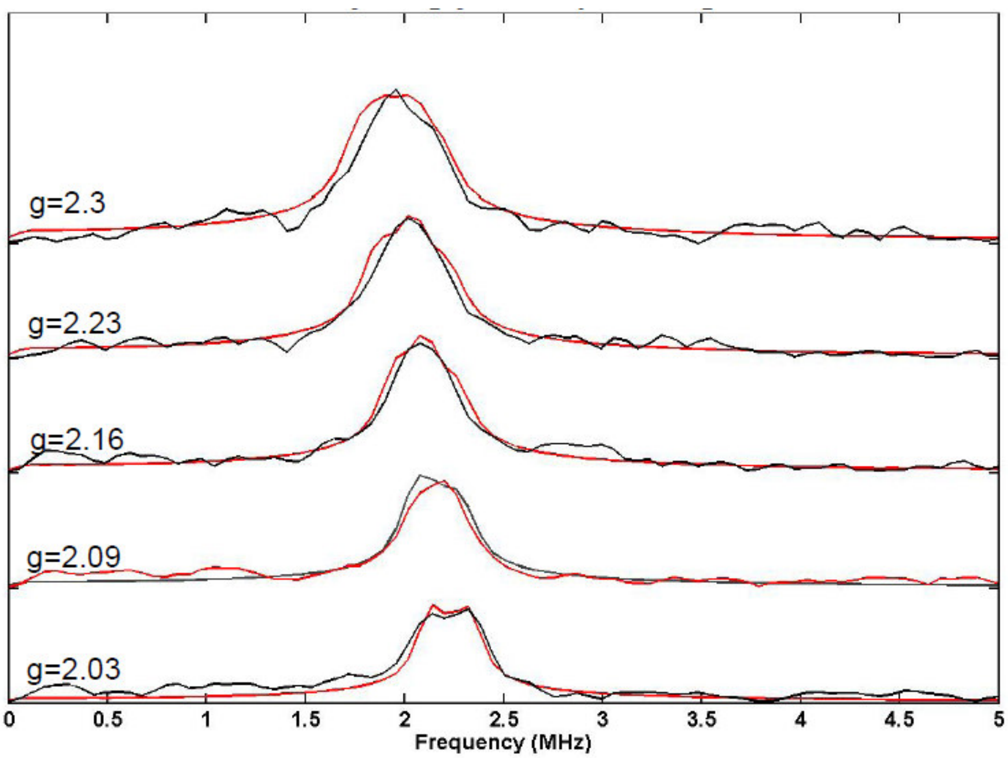

FIGURE 37. ^{2}H ESEEM spectra of TyrH:Fe(II):NO-[tyrosine, ^{2}H-6MPH$_4$] at corresponding g values. Red lines are the simulations of the spectra with the following Hamiltonian parameters: principal deuterium hyperfine values of [-0.16,-0.16, 0.32] MHz with Euler angles of (0, 66°, 0), e^2qQ = 0.2 MHz; Euler angles relating the nuclear quadrupole interaction to the hyperfine interaction of (0, 43°,0). Concentrations were 0.95 mM ferrous TyrH, 1 mM tyrosine, 1.5 mM ^{2}H-6MPH$_4$ and 0.6 mM MAHMA NONOate in 100 mM Mops (pH 7.0), 0.3 M KCl and 30% glycerol. Samples were prepared at 25 °C.

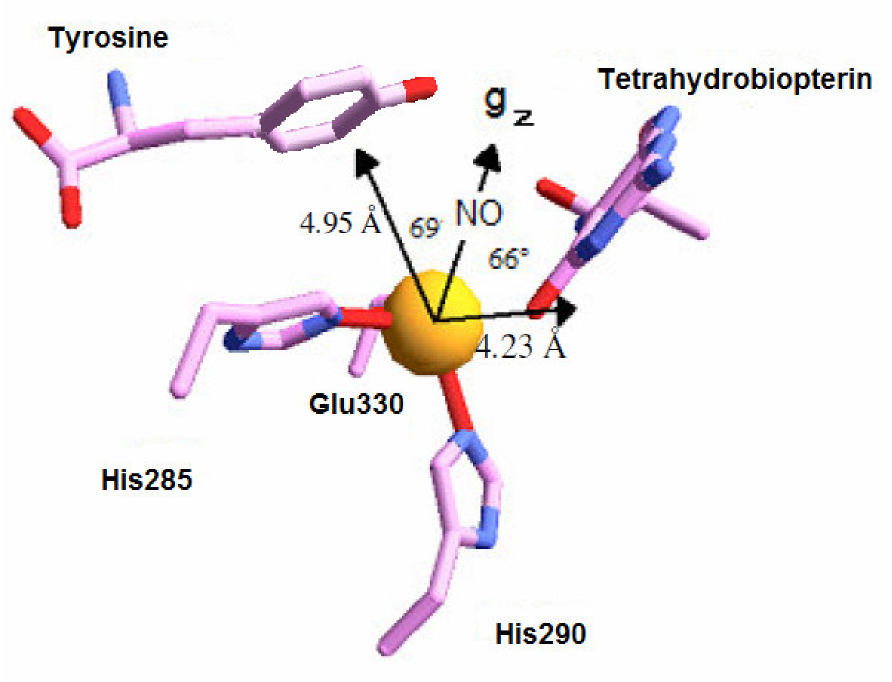

FIGURE 38. Position of the Fe-NO bond axis (g_z axis) with respect to the substrate tyrosine and pterin cofactor deuterons in the quaternary complex. The model is based on the crystal structure of PheH with thienylalanine and tetrahydrobiopterin bound (PDB entry 1KW0). Tyrosine was modeled in the place of thienylalanine.

DISCUSSION

Complexes of TyrH:NO were investigated by various spectroscopic techniques to reveal the active site structure in a catalytically relevant O_2-mimic bound form. Since NO can bind to the active site iron, it acts as an oxygen mimic and thus provides information about the active site changes at the stage of oxygen binding and about possible oxygen intermediates. In addition, binding of NO to the iron produces a $\{Fe\text{-}NO\}^7$ spin system with S = 3/2 that allows probing the active site by EPR techniques, which would be otherwise impossible due to the S = 2 of high spin ferrous iron (*115*).

The ESEEM data for TyrH:Fe(II):NO-[^{2}H-6MPH$_4$] complex shows that the distance of 6MPH$_4$ to the iron atom is 5.9 Å. At such a distance, no significant interaction of the active site iron is expected with 6MPH$_4$. This is consistent with the similar pattern observed for the EPR spectra of TyrH:Fe(II):NO and TyrH:Fe(II):NO:6MPH$_4$. Both complexes have very similar E/D values and exist as a single population.

Based on the studies of nonheme enzyme systems and model complexes, the increase in rhombicity in a nonheme $\{Fe\text{-}NO\}^7$ complex can be attributed to the effects on the Fe-NO environment due to a decrease in the Fe-N-O bond angle (*127*) and/or an increase in the strength of the equatorial ligands with respect to the axial Fe-NO bond (*120, 121*). The EPR spectrum of TyrH:Fe(II):NO:tyr indicates the presence of two populations of enzyme. The major component is more axial than TyrH:Fe(II):NO, whereas the minor component is more rhombic. These differences indicate that tyrosine binding affects the Fe-NO environment. This observation is further supported by the ESEEM data of TyrH:Fe(II):NO:tyr, which shows an interacting tyrosine deuteron at a distance of 4.33 Å from the iron, with an angle of 72° with respect to Fe-NO bond.

The most rhombic patterns in the EPR spectra were observed for the two distinct populations of the TyrH:Fe(II):NO:tyr:6MPH$_4$ complex with the minor component being much more rhombic, suggesting larger changes in the Fe-NO environment than in the tyrosine bound complex. This is consistent with the previous crystallographic (*25*) and spectroscopic *(vide supra)* studies in the absence of a dioxygen analogue, which showed that a water ligand leaves and the glutamate ligand becomes bidentate upon binding of both the substrate and the cofactor. The ESEEM analysis of the TyrH:Fe(II):NO:tyr:6MPH$_4$ indicates that 6MPH$_4$ moves closer to the active site, resulting in a distance of 4.23 Å to the iron, in agreement with the crystal structure (*25*). Overall, the previous data and our current data together show that the active site iron environment goes through a number of significant changes that affect the Fe-NO bond angle. Since NO is a dioxygen mimic, presumably these changes are effective in fine tuning the O$_2$ bonding mode of the active site for catalysis only when all substrates are present.

The largest absorption peaks seen upon addition of NO to the resting, substrate and/or cofactor bound forms were observed at 450 nm, consistent with the formation of the corresponding Fe-NO complexes (*115, 117*). The absorbance changes at 450 nm and in the 500-600 nm region for the quaternary complex (when both tyrosine and 6MPH$_4$ were present) were much larger than the changes in the binary and ternary NO complexes. Since the intensity of the Fe(III) to NO$^-$ charge transfer band is dependent on the strength of the overlap between the iron d orbitals and NO 2π* orbitals, such an increase in intensity can be attributed to the decrease in the Fe-N-O bond angle, consistent with the observations from the EPR spectra. A similar pattern has been observed with a number of other mononuclear nonheme enzymes (*117, 122*). A blue shift (~15 nm) with respect to the other complexes was also observed for the 450 nm transition in the pterin bound complex. This might be indicative of an effect on the Fe-N-O bond due to $6MPH_4$ binding or be due to the conformational change (*vide supra*) upon $6MPH_4$ binding, even though the EPR and ESEEM data do not support such a conclusion. The similar EPR patterns of TyrH:Fe(II):NO and TyrH:Fe(II):NO:$6MPH_4$ (Figure 31 and Table 10) suggest a similar angle for the Fe-N-O bond. However, as shown in Figure 36, an interaction between π system of $6MPH_4$ and π orbitals of NO is possible, giving rise to a change in the energy of the π^* orbital of NO^- without a corresponding change in the Fe-N-O bond angle, thus making it compatible with the EPR spectra. Therefore, the absence of the blue shift in the quaternary NO complex can be explained by a diminished interaction between the π system of $6MPH_4$ and the π orbitals of NO, since the Fe-N-O angle decreases in the quaternary complex.

When the ESEEM analyses of various complexes of TyrH:Fe(II):NO are compared, it can be concluded that binding of $6MPH_4$ pushes tyrosine away from the active site such that the 4.33 Å distance between tyrosine deuteron and the iron becomes larger than 4.95 Å. This is in agreement with earlier studies, which showed that binding of pterin is associated with the movement of a large surface loop and the residues in this loop pack against the amino acid binding pocket (*34*). This observation is also consistent with previous studies that demonstrated formation of a dead-end complex when tyrosine binds to the free enzyme and with the substrate inhibition observed at high concentrations of tyrosine (*36*). Overall it is clear that binding of $6MPH_4$ creates the binding site for tyrosine by initiating protein conformational changes that position tyrosine for productive turnover.

The distance of tyrosine from the iron in the presence of $6MPH_4$ is not close enough for a reaction between the Fe(IV)O intermediate and tyrosine (based on the approximate distance from N of Fe-NO to the ring position to be hydroxylated, estimated according to the positions in Figure 38). However, Fe(IV)O forms by the heterolytic cleavage of an iron-peroxy-pterin bridge, which also leads to the formation of 4a-hydroxypterin. It is reasonable to assume that a different conformation of 4a-hydroxypterin compared to $6MPH_4$ can pull tyrosine close to the iron. This observation indicates that only after the Fe(IV)O forms, does tyrosine become close enough for a productive reaction. This should prevent any direct reaction between the iron-peroxy-pterin bridged intermediate and tyrosine. Such a mechanism ensures the strict coupling of tyrosine hydroxylation to $6MPH_4$ oxidation in TyrH.

Earlier structural studies and kinetic studies presented in Chapter III are in agreement with the ESEEM data of the $6MPH_4$ bound complexes in the absence and presence of tyrosine, which show that the pterin deuteron is at a distance 5.9 Å from the iron in the absence of tyrosine and that this distance decreases to 4.23 Å when tyrosine is bound. A distance of 6 Å between the iron and the pterin C(4a) in the crystal structure of pterin bound PheH decreases to 4.5 Å in the ternary complex (both pterin and substrate analogue bound) (*21*). In addition, kinetic studies in Chapter III showed that the rate of the reaction between oxygen, iron and pterin in the absence of tyrosine is orders of magnitude slower than the rates in the presence of tyrosine.

NO complexes of F184A TyrH were also investigated by EPR spectroscopy. The spectra obtained for all complexes were very similar to the WT enzyme in terms of E/D values. However, there is a decrease in the relative intensity of the major component of the EPR signals in both of the tyrosine complexes (Figure 32C and 32D), which exhibit a mixture of two different populations with slightly different iron environments. This suggests that the movement of the loop with the mutated residue shifts the equilibrium between the two forms of the enzyme, rather than directly affecting the active site. If the component that increases is an inactive form of the enzyme, the uncoupling observed in this mutant might be explained. However, such an assignment will require more detailed analysis of the EPR signals.

Overall, this study brought has brought further insight into the electronic and geometric structure of the active site in TyrH. Investigation of the effects of substrate and/or cofactor binding on the O_2-mimic bound TyrH provided information on the events that occur prior to the chemical steps in the TyrH reaction.

CHAPTER VI

SUMMARY

Studies presented in this dissertation have focused on the catalytic mechanism of tyrosine hydroxylase. One important question in the mechanism of this mononuclear non-heme enzyme and other members of the AAH family has been the identity of the hydroxylating intermediate. An Fe(IV)O species has for long been proposed to be the hydroxylating species. Chapter II describes the kinetic and spectroscopic characterization of an Fe(IV) intermediate in the TyrH reaction pathway by Mössbauer spectroscopy. Further kinetic studies using rapid chemical quench and stopped-flow absorption spectroscopy established this intermediate to be kinetically competent enough to be the Fe(IV)O hydroxylating intermediate. This was the first example for the involvement of an Fe(IV) species in a mononuclear enzyme catalyzing aromatic hydroxylation.

Chapter III described the spectroscopic and kinetic investigation of various tyrosine hydroxylase complexes. Spectroscopic studies showed that resting form and only tyrosine or only $6MPH_4$ bound forms of TyrH have a 6-coordinate iron. In the presence of both tyrosine and $6MPH_4$, the active site iron changes its coordination state to 5-coordinate form. Kinetic studies on the reactivity of oxygen with 5 and 6-coordinate complexes of TyrH indicated that there is a 2-3 orders of magnitude rate enhancement of the reaction of oxygen with the catalytic 5-coordinate complex over 6-coordinate complexes and non-catalytic 5-coordinate complexes. This strategy protects the enzyme from non-catalytic oxidation reactions in the absence of the required substrate and cofactor.

Chapter IV is a combination of rapid reaction and viscosity studies. Rapid chemical quench experiments demonstrated a DOPA burst, indicating a slower step after DOPA formation. Steady-state viscosity studies established this step as being a significantly diffusion-limited step. Stopped-flow studies indicate that a combination of chemical and physical steps, including conformational change, determines k_{cat} of TyrH reaction.

Chapter V focused on the investigation of the NO complexes of TyrH. A combination of UV-Vis, EPR and ESEEM spectroscopies revealed the active site changes upon substrate and cofactor binding in an O_2-mimic bound form of the enzyme. $6MPH_4$ binding creates the binding site for tyrosine and binding of tyrosine initiates fine tuning of the active site such that iron, oxygen and $6MPH_4$ becomes close enough to react to form the putative iron-peroxy-pterin bridged intermediate. Tyrosine is not close enough to interact with this intermediate, suggesting that tyrosine moves towards iron only after the hydroxylating intermediate, Fe(IV)O, forms, which seems to be the strategy used by this enzyme to prevent unproductive turnover.

REFERENCES

1. Kovaleva, E. G., and Lipscomb, J. D. (2008) Versatility of biological non-heme Fe(II) centers in oxygen activation reactions, *Nat Chem Biol 4*, 186-193.

2. Solomon, E. I., Brunold, T. C., Davis, M. I., Kemsley, J. N., Lee, S. K., Lehnert, N., Neese, F., Skulan, A. J., Yang, Y. S., and Zhou, J. (2000) Geometric and electronic structure/function correlations in non-heme iron enzymes, *Chem Rev 100*, 235-350.

3. Klinman, J. P. (2007) How do enzymes activate oxygen without inactivating themselves?, *Acc Chem Res 40*, 325-333.

4. Abu-Omar, M. M., Loaiza, A., and Hontzeas, N. (2005) Reaction mechanisms of mononuclear non-heme iron oxygenases, *Chem Rev 105*, 2227-2252.

5. Bruijnincx, P. C., van Koten, G., and Klein Gebbink, R. J. (2008) Mononuclear non-heme iron enzymes with the 2-His-1-carboxylate facial triad: recent developments in enzymology and modeling studies, *Chem Soc Rev 37*, 2716-2744.

6. Costas, M., Mehn, M. P., Jensen, M. P., and Que, L., Jr. (2004) Dioxygen activation at mononuclear nonheme iron active sites: enzymes, models, and intermediates, *Chem Rev 104*, 939-986.

7. Ryle, M. J., and Hausinger, R. P. (2002) Non-heme iron oxygenases, *Curr Opin Chem Biol 6*, 193-201.

8. Sono, M., Roach, M. P., Coulter, E. D., and Dawson, J. H. (1996) Heme-containing oxygenases, *Chem Rev 96*, 2841-2888.

9. Denisov, I. G., Makris, T. M., Sligar, S. G., and Schlichting, I. (2005) Structure and chemistry of cytochrome P450, *Chem Rev 105*, 2253-2277.

10. Bollinger, J. M., Jr., and Krebs, C. (2006) Stalking intermediates in oxygen activation by iron enzymes: motivation and method, *J Inorg Biochem 100*, 586-605.

11. Koehntop, K. D., Emerson, J. P., and Que, L., Jr. (2005) The 2-His-1-carboxylate facial triad: a versatile platform for dioxygen activation by mononuclear non-heme iron(II) enzymes, *J Biol Inorg Chem 10*, 87-93.

12. Que, L., Jr. (2000) One motif-many different reactions, *Nat Struct Biol 7*, 182-184.

13. Straganz, G. D., and Nidetzky, B. (2006) Variations of the 2-His-1-carboxylate theme in mononuclear non-heme Fe(II) oxygenases, *Chembiochem 7*, 1536-1548.

14. Hausinger, R. P. (2004) Fe(II)/alpha-ketoglutarate-dependent hydroxylases and related enzymes, *Crit Rev Biochem Mol Biol 39*, 21-68.

15. Fitzpatrick, P. F. (2000) The aromatic amino acid hydroxylases, *Adv Enzymol Relat Areas Mol Biol 74*, 235-294.

16. Fitzpatrick, P. F. (1999) Tetrahydropterin-dependent amino acid hydroxylases, *Annu Rev Biochem 68*, 355-381.

17. Royo, M., Daubner, S. C., and Fitzpatrick, P. F. (2005) Effects of mutations in tyrosine hydroxylase associated with progressive dystonia on the activity and stability of the protein, *Proteins 58*, 14-21.

18. Zafeiriou, D. I., Willemsen, M. A., Verbeek, M. M., Vargiami, E., Ververi, A., and Wevers, R. (2009) Tyrosine hydroxylase deficiency with severe clinical course, *Mol Genet Metab 97*, 18-20.

19. Windahl, M. S., Petersen, C. R., Christensen, H. E., and Harris, P. (2008) Crystal structure of tryptophan hydroxylase with bound amino acid substrate, *Biochemistry 47*, 12087-12094.

20. Walther, D. J., and Bader, M. (2003) A unique central tryptophan hydroxylase isoform, *Biochem Pharmacol 66*, 1673-1680.

21. Fitzpatrick, P. F. (2003) Mechanism of aromatic amino acid hydroxylation, *Biochemistry 42*, 14083-14091.

22. Kobe, B., Jennings, I. G., House, C. M., Feil, S. C., Michell, B. J., Tiganis, T., Parker, M. W., Cotton, R. G., and Kemp, B. E. (1997) Regulation and crystallization of phosphorylated and dephosphorylated forms of truncated dimeric phenylalanine hydroxylase, *Protein Sci 6*, 1352-1357.

23. Goodwill, K. E., Sabatier, C., Marks, C., Raag, R., Fitzpatrick, P. F., and Stevens, R. C. (1997) Crystal structure of tyrosine hydroxylase at 2.3 A and its implications for inherited neurodegenerative diseases, *Nat Struct Biol 4*, 578-585.

24. Erlandsen, H., Fusetti, F., Martinez, A., Hough, E., Flatmark, T., and Stevens, R. C. (1997) Crystal structure of the catalytic domain of human phenylalanine hydroxylase reveals the structural basis for phenylketonuria, *Nat Struct Biol 4*, 995-1000.

25. Andersen, O. A., Flatmark, T., and Hough, E. (2002) Crystal structure of the ternary complex of the catalytic domain of human phenylalanine hydroxylase with tetrahydrobiopterin and 3-(2-thienyl)-L-alanine, and its implications for the mechanism of catalysis and substrate activation, *J Mol Biol 320*, 1095-1108.

26. Wang, L., Erlandsen, H., Haavik, J., Knappskog, P. M., and Stevens, R. C. (2002) Three-dimensional structure of human tryptophan hydroxylase and its implications for the biosynthesis of the neurotransmitters serotonin and melatonin, *Biochemistry 41*, 12569-12574.

27. Goodwill, K. E., Sabatier, C., and Stevens, R. C. (1998) Crystal structure of tyrosine hydroxylase with bound cofactor analogue and iron at 2.3 A resolution: self-hydroxylation of Phe300 and the pterin-binding site, *Biochemistry 37*, 13437-13445.

28. Andersen, O. A., Flatmark, T., and Hough, E. (2001) High resolution crystal structures of the catalytic domain of human phenylalanine hydroxylase in its catalytically active Fe(II) form and binary complex with tetrahydrobiopterin, *J Mol Biol 314*, 279-291.

29. Daubner, S. C., and Fitzpatrick, P. F. (1999) Site-directed mutants of charged residues in the active site of tyrosine hydroxylase, *Biochemistry 38*, 4448-4454.

30. Andersen, O. A., Stokka, A. J., Flatmark, T., and Hough, E. (2003) 2.0 A resolution crystal structures of the ternary complexes of human phenylalanine hydroxylase catalytic domain with tetrahydrobiopterin and 3-(2-thienyl)-L-alanine

or L-norleucine: substrate specificity and molecular motions related to substrate binding, *J Mol Biol 333*, 747-757.

31. Wasinger, E. C., Mitic, N., Hedman, B., Caradonna, J., Solomon, E. I., and Hodgson, K. O. (2002) X-ray absorption spectroscopic investigation of the resting ferrous and cosubstrate-bound active sites of phenylalanine hydroxylase, *Biochemistry 41*, 6211-6217.

32. Kemsley, J. N., Wasinger, E. C., Datta, S., Mitic, N., Acharya, T., Hedman, B., Caradonna, J. P., Hodgson, K. O., and Solomon, E. I. (2003) Spectroscopic and kinetic studies of PKU-inducing mutants of phenylalanine hydroxylase: Arg158Gln and Glu280Lys, *J Am Chem Soc 125*, 5677-5686.

33. Daubner, S. C., McGinnis, J. T., Gardner, M., Kroboth, S. L., Morris, A. R., and Fitzpatrick, P. F. (2006) A flexible loop in tyrosine hydroxylase controls coupling of amino acid hydroxylation to tetrahydropterin oxidation, *J Mol Biol 359*, 299-307.

34. Sura, G. R., Lasagna, M., Gawandi, V., Reinhart, G. D., and Fitzpatrick, P. F. (2006) Effects of ligands on the mobility of an active-site loop in tyrosine hydroxylase as monitored by fluorescence anisotropy, *Biochemistry 45*, 9632-9638.

35. Daubner, S. C., Melendez, J., and Fitzpatrick, P. F. (2000) Reversing the substrate specificities of phenylalanine and tyrosine hydroxylase: aspartate 425 of tyrosine hydroxylase is essential for L-DOPA formation, *Biochemistry 39*, 9652-9661.

36. Fitzpatrick, P. F. (1991) Steady-state kinetic mechanism of rat tyrosine hydroxylase, *Biochemistry 30*, 3658-3662.

37. Ellis, H. R., Daubner, S. C., and Fitzpatrick, P. F. (2000) Mutation of serine 395 of tyrosine hydroxylase decouples oxygen-oxygen bond cleavage and tyrosine hydroxylation, *Biochemistry 39*, 4174-4181.

38. Frantom, P. A., and Fitzpatrick, P. F. (2003) Uncoupled forms of tyrosine hydroxylase unmask kinetic isotope effects on chemical steps, *J Am Chem Soc 125*, 16190-16191.

39. Pavon, J. A., and Fitzpatrick, P. F. (2005) Intrinsic isotope effects on benzylic hydroxylation by the aromatic amino acid hydroxylases: evidence for hydrogen

tunneling, coupled motion, and similar reactivities, *J Am Chem Soc 127*, 16414-16415.

40. Pavon, J. A., and Fitzpatrick, P. F. (2006) Insights into the catalytic mechanisms of phenylalanine and tryptophan hydroxylase from kinetic isotope effects on aromatic hydroxylation, *Biochemistry 45*, 11030-11037.

41. Panay, A. J., and Fitzpatrick, P. F. (2008) Kinetic isotope effects on aromatic and benzylic hydroxylation by *Chromobacterium violaceum* phenylalanine hydroxylase as probes of chemical mechanism and reactivity, *Biochemistry 47*, 11118-11124.

42. Bailey, S. W., Rebrin, I., Boerth, S. R., and Ayling, J. E. (1995) Synthesis of 4a-hydroxytetrahydropterins and the mechanism of their nonenzymatic dehydration to quinoid dihydropterins, *J Am Chem Soc 117*, 10203-10211.

43. Bailey, S. W., and Ayling, J. E. (1983) 6,6-dimethylpterins - stable quinoid dihydropterin substrate for dihydropteridine reductase and tetrahydropterin cofactor for phenylalanine-hydroxylase, *Biochemistry 22*, 1790-1798.

44. Hillas, P. J., and Fitzpatrick, P. F. (1996) A mechanism for hydroxylation by tyrosine hydroxylase based on partitioning of substituted phenylalanines, *Biochemistry 35*, 6969-6975.

45. Krebs, C., Fujimori, D. G., Walsh, C. T., and Bollinger, J. M. (2007) Non-heme Fe(IV)-oxo intermediates, *Acc Chem Res 40*, 484-492.

46. Frantom, P. A., Pongdee, R., Sulikowski, G. A., and Fitzpatrick, P. F. (2002) Intrinsic deuterium isotope effects on benzylic hydroxylation by tyrosine hydroxylase, *J Am Chem Soc 124*, 4202-4203.

47. Bassan, A., Blomberg, M. R., and Siegbahn, P. E. (2003) Mechanism of dioxygen cleavage in tetrahydrobiopterin-dependent amino acid hydroxylases, *Chemistry 9*, 106-115.

48. Bassan, A., Blomberg, M. R., and Siegbahn, P. E. (2003) Mechanism of aromatic hydroxylation by an activated FeIV=O core in tetrahydrobiopterin-dependent hydroxylases, *Chemistry 9*, 4055-4067.

49. Fitzpatrick, P. F. (1991) Studies of the rate-limiting step in the tyrosine hydroxylase reaction: alternate substrates, solvent isotope effects, and transition-state analogues, *Biochemistry 30*, 6386-6391.

50. Francisco, W. A., Tian, G. C., Fitzpatrick, P. F., and Klinman, J. P. (1998) Oxygen-18 kinetic isotope effect studies of the tyrosine hydroxylase reaction: evidence of rate limiting oxygen activation, *J Am Chem Soc 120*, 4057-4062.

51. Ramsey, A. J., Daubner, S. C., Ehrlich, J. I., and Fitzpatrick, P. F. (1995) Identification of iron ligands in tyrosine hydroxylase by mutagenesis of conserved histidinyl residues, *Protein Sci 4*, 2082-2086.

52. Que, L., Jr. (2007) The road to non-heme oxoferryls and beyond, *Acc Chem Res 40*, 493-500.

53. Krebs, C., Price, J. C., Baldwin, J., Saleh, L., Green, M. T., and Bollinger, J. M. (2005) Rapid freeze-quench Fe-57 Mössbauer spectroscopy: monitoring changes of an iron-containing active site during a biochemical reaction, *Inorganic Chemistry 44*, 742-757.

54. Hiner, A. N. P., Raven, E. L., Thorneley, R. N. F., Garcia-Canovas, F., and Rodriguez-Lopez, J. N. (2002) Mechanisms of compound I formation in heme peroxidases, *J Inorg Biochem 91*, 27-34.

55. Makris, T. M., von Koenig, K., Schlichting, I., and Sligar, S. G. (2006) The status of high-valent metal oxo complexes in the P450 cytochromes, *J Inorg Biochem 100*, 507-518.

56. Merkx, M., Kopp, D. A., Sazinsky, M. H., Blazyk, J. L., Muller, J., and Lippard, S. J. (2001) Dioxygen activation and methane hydroxylation by soluble methane monooxygenase: a tale of two irons and three proteins, *Angewandte Chemie-International Edition 40*, 2782-2807.

57. Price, J. C., Barr, E. W., Tirupati, B., Bollinger, J. M., and Krebs, C. (2003) The first direct characterization of a high-valent iron intermediate in the reaction of an alpha-ketoglutarate-dependent dioxygenase: a high-spin Fe(IV) complex in taurine/alpha-ketoglutarate dioxygenase (TauD) from *Escherichia coli*, *Biochemistry 42*, 7497-7508.

58. Proshlyakov, D. A., Henshaw, T. F., Monterosso, G. R., Ryle, M. J., and Hausinger, R. P. (2004) Direct detection of oxygen intermediates in the non-heme Fe enzyme taurine/alpha-ketoglutarate dioxygenase, *J Am Chem Soc 126*, 1022-1023.

59. Riggs-Gelasco, P. J., Price, J. C., Guyer, R. B., Brehm, J. H., Barr, E. W., Bollinger, J. M., Jr., and Krebs, C. (2004) EXAFS spectroscopic evidence for an Fe=O unit in the Fe(IV) intermediate observed during oxygen activation by taurine:alpha-ketoglutarate dioxygenase, *J Am Chem Soc 126*, 8108-8109.

60. Price, J. C., Barr, E. W., Glass, T. E., Krebs, C., and Bollinger, J. M., Jr. (2003) Evidence for hydrogen abstraction from C1 of taurine by the high-spin Fe(IV) intermediate detected during oxygen activation by taurine:alpha-ketoglutarate dioxygenase (TauD), *J Am Chem Soc 125*, 13008-13009.

61. Frantom, P. A., Seravalli, J., Ragsdale, S. W., and Fitzpatrick, P. F. (2006) Reduction and oxidation of the active site iron in tyrosine hydroxylase: kinetics and specificity, *Biochemistry 45*, 2372-2379.

62. Daubner, S. C., Lauriano, C., Haycock, J. W., and Fitzpatrick, P. F. (1992) Site-directed mutagenesis of serine 40 of rat tyrosine hydroxylase. Effects of dopamine and cAMP-dependent phosphorylation on enzyme activity, *J Biol Chem 267*, 12639-12646.

63. Ravi, N., Bollinger, J. M., Huynh, B. H., Edmondson, D. E., and Stubbe, J. (1994) Mechanism of assembly of the tyrosyl radical-diiron(III) cofactor of *Escherichia coli* ribonucleotide reductase: 1. Mössbauer characterization of the diferric radical precursor, *J Am Chem Soc 116*, 8007-8014.

64. Baldwin, J., Krebs, C., Ley, B. A., Edmondson, D. E., Huynh, B. H., and Bollinger, J. H. (2000) Mechanism of rapid electron transfer during oxygen activation in the R2 subunit of *Escherichia coli* ribonucleotide reductase. 1. Evidence for a transient tryptophan radical, *J Am Chem Soc 122*, 12195-12206.

65. Kuzmic, P. (1996) Program DYNAFIT for the analysis of enzyme kinetic data: application to HIV proteinase, *Analytical Biochemistry 237*, 260-273.

66. Sinnecker, S., Svensen, N., Barr, E. W., Ye, S., Bollinger, J. M., Neese, F., and Krebs, C. (2007) Spectroscopic and computational evaluation of the structure of the high-spin Fe(IV)-oxo intermediates in taurine: alpha-ketoglutarate

dioxygenase from *Escherichia coli* and its His99Ala ligand variant, *J Am Chem Soc 129*, 6168-6179.

67. Neese, F. (2006) Theoretical spectroscopy of model-nonheme [Fe(IV)OL5](2+) complexes in their lowest triplet and quintet states using multireference ab initio and density functional theory methods, *J Inorg Biochem 100*, 716-726.

68. Pestovsky, O., Stoian, S., Bominaar, E. L., Shan, X. P., Munck, E., Que, L., and Bakac, A. (2005) Aqueous Fe-IV=O: spectroscopic identification and oxo-group exchange, *Angewandte Chemie-International Edition 44*, 6871-6874.

69. Moran, G. R., Derecskei-Kovacs, A., Hillas, P. J., and Fitzpatrick, P. F. (2000) On the catalytic mechanism of tryptophan hydroxylase, *J Am Chem Soc 122*, 4535-4541.

70. Hoffart, L. M., Barr, E. W., Guyer, R. B., Bollinger, J. M., Jr., and Krebs, C. (2006) Direct spectroscopic detection of a C-H-cleaving high-spin Fe(IV) complex in a prolyl-4-hydroxylase, *Proc Natl Acad Sci U S A 103*, 14738-14743.

71. Galonic, D. P., Barr, E. W., Walsh, C. T., Bollinger, J. M., Jr., and Krebs, C. (2007) Two interconverting Fe(IV) intermediates in aliphatic chlorination by the halogenase CytC3, *Nat Chem Biol 3*, 113-116.

72. Moran, G. R., Daubner, S. C., and Fitzpatrick, P. F. (1998) Expression and characterization of the catalytic core of tryptophan hydroxylase, *J Biol Chem 273*, 12259-12266.

73. Haavik, J., and Flatmark, T. (1987) Isolation and characterization of tetrahydropterin oxidation products generated in the tyrosine 3-monooxygenase (tyrosine hydroxylase) reaction, *Eur J Biochem 168*, 21-26.

74. Kemsley, J. N., Mitic, N., Loeb Zaleski, K., Caradonna, J. P., and Solomon, E. I. (1999) Circular dichroism and magnetic circular dichroism spectroscopy of the catalytically competent ferrous active site of phenylalanine hydroxylase and its interaction with pterin cofactor, *J Am Chem Soc 121*, 1528-1536.

75. Meyer-Klaucke, W., Winkler, H., Schünemann, V., Trautwein, A. X., Nolting, H.-F., and Haavik, J. (1996) Mössbauer, electron-paramagnetic-resonance and X-ray-absorption fine-structure studies of the iron environment in recombinant human tyrosine hydroxylase, *Eur J Biochem 241*, 432-439.

76. Moad, G., Luthy, C. L., Benkovic, P. A., and Benkovic, S. J. (1979) Studies on 6-methyl-5-deazatetrahydropterin and its 4a adducts, *J Am Chem Soc 101*, 6068-6076.

77. Loeb, K. E., Westre, T. E., Kappock, T. J., Mitic, N., Glasfeld, E., Caradonna, J. P., Hedman, B., Hodgson, K. O., and Solomon, E. I. (1997) Spectroscopic characterization of the catalytically competent ferrous site of the resting, activated, and substrate-bound forms of phenylalanine hydroxylase, *J Am Chem Soc 119*, 1901-1915.

78. Pavlosky, M. A., Zhang, Y., Westre, T. E., Gan, Q.-F., Pavel, E. G., Campochiaro, C., Hedman, B., Hodgson, K. O., and Solomon, E. I. (1995) Near infrared circular dichroism, magnetic circular dichroism, and X-ray absorption spectral comparison of the non-heme ferrous active sites of plant and mammalian 15-lipoxygenases, *J Am Chem Soc 117*, 4316-4327.

79. Westre, T. E., Kennepohl, P., DeWitt, J. G., Hedman, B., Hodgson, K. O., and Solomon, E. I. (1997) A multiplet analysis of Fe K-edge 1s->3d pre-edge features of iron complexes, *J Am Chem Soc 119*, 6297-6314.

80. Solomon, E. I., Brunold, T. C., Davis, M. I., Kemsley, J. N., Lee, S.-K., Lehnert, N., Neese, F., Skulan, A. J., Yang, Y.-S., and Zhou, J. (2000) Geometric and electronic structure/function correlations in non-heme iron enzymes, *Chem Rev 100*, 235-349.

81. Pavel, E. G., Kitajima, N., and Solomon, E. I. (1998) Magnetic circular dichroism spectroscopic studies of mononuclear non-heme ferrous model complexes: correlation of excited state and ground state electronic structure with geometry, *J Am Chem Soc 120*, 3949-3962.

82. Solomon, E. I., Pavel, E. G., Loeb, K. E., and Campochiaro, C. (1995) Magnetic circular dichroism spectrosopy as a probe of the geometric and electronic structure of non-heme ferrous enzymes, *Coord Chem Rev 144*, 369-460.

83. Andersen, O. A., Stokka, A. J., Flatmark, T., and Hough, E. (2003) 2.0 angstrom resolution crystal structures of the ternary complexes of human phenylalanine hydroxylase catalytic domain with tetrahydrobiopterin and 3-(2-thienyl)-L-alanine or L-norleucine: substrate specificity and molecular motions related to substrate binding, *J Mol Biol 333*, 747-757.

84. Hagedoorn, P.-L., Schmidt, P. P., Anderson, K. K., Hagen, W. R., Flatmark, T., and Martinez, A. (2001) The effect of substrate, dihydropterin, and dopamine on the EPR spectroscopic properties and the midpoint potential of the catalytic iron in recombinant human phenylalanine hydroxylase, *J Biol Chem 276*, 22850-22856.

85. Sawyer, D. T. (1991) *Oxygen Chemistry*, Oxford University Press, New York.

86. Gorren, A. C. F., Kungl, A. J., Schmidt, K., Werner, E. R., and Mayer, B. (2001) Electrochemistry of pterin cofactors and inhibitors of nitric oxide synthase, *Nitric Oxide 5*, 176-186.

87. Ballou, D. P., Entsch, B., and Cole, L. J. (2005) Dynamics involved in catalysis by single-component and two-component flavin-dependent aromatic Hydroxylases, *Biochem Biophys Res Comm 338*, 590-598.

88. Neidig, M. L., and Solomon, E. I. (2005) Structure-function correlations in oxygen activating non-heme iron enzymes, *Chem Commun 2005*, 5843-5463.

89. Solomon, E. I. (2001) Geometric and electronic structure contributions to function in bioinorganic chemistry: active sites in non-heme iron enzymes, *Inorganic Chemistry 40*, 3656-3669.

90. Solomon, E. I., Decker, A., and Lehnert, N. (2003) Non-heme iron enzymes: contrasts to heme catalysis, *Proc Natl Acad Sci USA 100*, 3589-3594.

91. Cheng, N. S. (2008) Formula for the viscosity of a glycerol-water mixture, *Industrial & Engineering Chemistry Research 47*, 3285-3288.

92. Mathlouthi, M., Genotelle, J. (1994) Rheological properties of sucrose solutions and suspensions in *Sucrose* (Mathlouthi, M., and Reiser, P., Ed.), pp 126-154, Blackie Academic & Professional, New York.

93. Rampp, M., Buttersack, C., and Ludemann, H. D. (2000) c,T-dependence of the viscosity and the self-diffusion coefficients in some aqueous carbohydrate solutions, *Carbohydrate Research 328*, 561-572.

94. Sadler, G. D., Roberts, J., and Cornell, J. (1988) Determination of oxygen solubility in liquid foods using a dissolved-oxygen electrode, *Journal of Food Science 53*, 1493-1496.

95. Johnson, K. A. (1995) Rapid quench kinetic analysis of polymerases, adenosinetriphosphatases, and enzyme intermediates, *Methods Enzymol 249*, 38-61.

96. Brouwer, A. C., and Kirsch, J. F. (1982) Investigation of diffusion-limited rates of chymotrypsin reactions by viscosity variation, *Biochemistry 21*, 1302-1307.

97. Johnson, W. W., Liu, S. X., Ji, X. H., Gilliland, G. L., and Armstrong, R. N. (1993) Tyrosine-115 participates both in chemical and physical steps of the catalytic mechanism of a glutathione-S-transferase, *J Biol Chem 268*, 11508-11511.

98. Fitzpatrick, P. F., Kurtz, K. A., Denu, J. M., and Emanuele, J. F. (1997) Contrasting values of commitment factors measured from viscosity, pH, and kinetic isotope effects: evidence for slow conformational changes in the D-amino acid oxidase reaction, *Bioorganic Chemistry 25*, 100-109.

99. Adams, J. A., and Taylor, S. S. (1992) Energetic limits of phosphotransfer in the catalytic subunit of cAMP-dependent protein-kinase as measured by viscosity experiments, *Biochemistry 31*, 8516-8522.

100. Cole, P. A., Burn, P., Takacs, B., and Walsh, C. T. (1994) Evaluation of the catalytic mechanism of recombinant human Csk (C-terminal Src kinase) using nucleotide analogs and viscosity effects, *J Biol Chem 269*, 30880-30887.

101. Caccuri, A. M., Antonini, G., Nicotra, M., Battistoni, A., Lo Bello, M., Board, P. G., Parker, M. W., and Ricci, G. (1997) Catalytic mechanism and role of hydroxyl residues in the active site of theta class glutathione S-transferases. Investigation of Ser-9 and Tyr-113 in a glutathione S-transferase from the Australian sheep blowfly, *Lucilia cuprina*, *J Biol Chem 272*, 29681-29686.

102. Kale, S., Ulas, G., Song, J., Brudvig, G. W., Furey, W., and Jordan, F. (2008) Efficient coupling of catalysis and dynamics in the E1 component of *Escherichia coli* pyruvate dehydrogenase multienzyme complex, *Proc Natl Acad Sci U S A 105*, 1158-1163.

103. McKay, G. A., and Wright, G. D. (1996) Catalytic mechanism of enterococcal kanamycin kinase (APH(3')-IIIa): viscosity, thio, and solvent isotope effects support a Theorell-Chance mechanism, *Biochemistry 35*, 8680-8685.

104. Wallick, D. E., Bloom, L. M., Gaffney, B. J., and Benkovic, S. J. (1984) Reductive activation of phenylalanine-hydroxylase and its effect on the redox state of the non-heme iron, *Biochemistry 23*, 1295-1302.

105. Sampson, N. S., and Knowles, J. R. (1992) Segmental motion in catalysis: investigation of a hydrogen bond critical for loop closure in the reaction of triosephosphate isomerase, *Biochemistry 31*, 8488-8494.

106. Simopoulos, T. T., and Jencks, W. P. (1994) Alkaline phosphatase is an almost perfect enzyme, *Biochemistry 33*, 10375-10380.

107. Ricci, G., Caccuri, A. M., Lo Bello, M., Rosato, N., Mei, G., Nicotra, M., Chiessi, E., Mazzetti, A. P., and Federici, G. (1996) Structural flexibility modulates the activity of human glutathione transferase P1-1. Role of helix 2 flexibility in the catalytic mechanism, *J Biol Chem 271*, 16187-16192.

108. Ansari, A., Jones, C. M., Henry, E. R., Hofrichter, J., and Eaton, W. A. (1992) The role of solvent viscosity in the dynamics of protein conformational changes, *Science 256*, 1796-1798.

109. Sampedro, J. G., and Uribe, S. (2004) Trehalose-enzyme interactions result in structure stabilization and activity inhibition. The role of viscosity, *Mol Cell Biochem 256-257*, 319-327.

110. Wang, S., Sura, G. R., Dangott, L. J., and Fitzpatrick, P. F. (2009) Identification by hydrogen/deuterium exchange of structural changes in tyrosine hydroxylase associated with regulation, *Biochemistry 48*, 4972-4979.

111. Magazu, S., Maisano, G., Migliardo, P., Middendorf, H. D., and Villari, V. (1998) Hydration and transport properties of aqueous solutions of alpha-alpha-trehalose, *Journal of Chemical Physics 109*, 1170-1174.

112. Cottone, G., Giuffrida, S., Ciccotti, G., and Cordone, L. (2005) Molecular dynamics simulation of sucrose- and trehalose-coated carboxy-myoglobin, *Proteins 59*, 291-302.

113. Luzardo, M. C., Amalfa, F., Nunez, A. M., Diaz, S., Biondi De Lopez, A. C., and Disalvo, E. A. (2000) Effect of trehalose and sucrose on the hydration and dipole potential of lipid bilayers, *Biophysical Journal 78*, 2452-2458.

114. Kawai, H., Sakurai, M., Inoue, Y., Chujo, R., and Kobayashi, S. (1992) Hydration of oligosaccharides: anomalous hydration ability of trehalose, *Cryobiology 29*, 599-606.

115. Brown, C. A., Pavlosky, M. A., Westre, T. E., Zhang, Y., Hedman, B., Hodgson, K. O., and Solomon, E. I. (1995) Spectroscopic and Theoretical Description of the Electronic-Structure of S=3/2 Iron-Nitrosyl Complexes and Their Relation to O-2 Activation by Nonheme Tron Enzyme Active-Sites, *J Am Chem Soc 117*, 715-732.

116. Yan, F., Moon, S. J., Liu, P., Zhao, Z., Lipscomb, J. D., Liu, A., and Liu, H. W. (2007) Determination of the substrate binding mode to the active site iron of (S)-2-Hydroxypropylphosphonic acid epoxidase using O-17-enriched substrates and substrate analogues, *Biochemistry 46*, 12628-12638.

117. Hegg, E. L., Whiting, A. K., Saari, R. E., McCracken, J., Hausinger, R. P., and Que, L., Jr. (1999) Herbicide-degrading alpha-keto acid-dependent enzyme TfdA: metal coordination environment and mechanistic insights, *Biochemistry 38*, 16714-16726.

118. Wasinger, E. C., Davis, M. I., Pau, M. Y. M., Orville, A. M., Zaleski, J. M., Hedman, B., Lipscomb, J. D., Hodgson, K. O., and Solomon, E. I. (2003) Spectroscopic studies of the effect of ligand donor strength on the Fe-NO bond in intradiol dioxygenases, *Inorganic Chemistry 42*, 365-376.

119. Nelson, M. J. (1987) The nitric oxide complex of ferrous soybean lipoxygenase-1. Substrate, pH, and ethanol effects on the active-site iron, *J Biol Chem 262*, 12137-12142.

120. Arciero, D. M., Orville, A. M., and Lipscomb, J. D. (1985) [O-17]water and nitric-oxide binding by protocatechuate 4,5-dioxygenase and catechol 2,3-dioxygenase - evidence for binding of exogenous ligands to the active-site Fe-2+ of extradiol dioxygenases, *J Biol Chem 260*, 4035-4044.

121. Chen, V. J., Orville, A. M., Harpel, M. R., Frolik, C. A., Surerus, K. K., Munck, E., and Lipscomb, J. D. (1989) Spectroscopic studies of isopenicillin-N synthase -

a mononuclear nonheme Fe-2+ oxidase with metal coordination sites for small molecules and substrate, *J Biol Chem 264*, 21677-21681.

122. Han, A. Y., Lee, A. Q., and Abu-Omar, M. M. (2006) EPR and UV-vis studies of the nitric oxide adducts of bacterial phenylalanine hydroxylase: effects of cofactor and substrate on the iron environment, *Inorganic Chemistry 45*, 4277-4283.

123. Fitzpatrick, P. F. (1988) The pH dependence of binding of inhibitors to bovine adrenal tyrosine hydroxylase, *J Biol Chem 263*, 16058-16062.

124. Keefer, L. K., Nims, R. W., Davies, K. M., and Wink, D. A. (1996) "NONOates" (1-substituted diazen-1-ium-1,2-diolates) as nitric oxide donors: convenient nitric oxide dosage forms, *Methods Enzymol 268*, 281-293.

125. Mims, W. B., Davis, J. L., and Peisach, J. (1984) The accessibility of type-I Cu(II) centers in laccase, azurin, and stellacyanin to exchangeable hydrogen and ambient water, *Biophysical Journal 45*, 755-766.

126. Muthukumaran, R. B., Grzyska, P. K., Hausinger, R. P., and McCracken, J. (2007) Probing the iron-substrate orientation for taurine/alpha-ketoglutarate dioxygenase using deuterium electron spin echo envelope modulation spectroscopy, *Biochemistry 46*, 5951-5959.

127. Ray, M., Golombek, A. P., Hendrich, M. P., Yap, G. P. A., Liable-Sands, L. M., Rheingold, A. L., and Borovik, A. S. (1999) Structure and magnetic properties of trigonal bipyramidal iron nitrosyl complexes, *Inorganic Chemistry 38*, 3110-3115.

VITA

Bekir Engin Eser

Department of Chemistry
Texas A&M University
PO Box 30012
College Station, TX, 77842-3012
Phone: (979) 739-4339
E-mail: bekireser@yahoo.com

Education

2009, Ph.D. in Chemistry, Texas A&M University

2004, B.S. in Chemistry, Bilkent University, Ankara, Turkey

Publications

- Chow, M. S., **Eser, B. E.** , Wilson, S. A., Hedman, B., Hodgson, K. O., Fitzpatrick, P. F., and Solomon, E. I. (2009) Spectroscopy and kinetics of wild-type and mutant tyrosine hydroxylase: Mechanistic insight into O_2 activation, *J Am Chem Soc 131,* 7685-7698

- **Eser, B. E.**, Barr, E. W., Frantom, P. A., Saleh, L., Bollinger, J. M., Jr., Krebs, C., and Fitzpatrick, P. F. (2007) Direct spectroscopic evidence for a high-spin Fe (IV) intermediate in tyrosine hydroxylase, *J Am Chem Soc 129*, 11334–11335.

- Demirors, A. F., **Eser, B. E.**, Dag, O. (2005) Liquid crystalline mesophases of Pluronics (L64, P65, and P123) and transition metal nitrate salts ($[M(H_2O)_6](NO_3)_2$), *Langmuir 21*, 4156-4162.